

Advanced Design Concepts and Efficient Finite Element Modeling for  
Dielectric Elastomer Devices

Dissertation  
zur Erlangung des Grades  
des Doktors der Ingenieurwissenschaften  
der Naturwissenschaftlich-Technischen Fakultät  
der Universität des Saarlandes

von

Philipp Loew

Saarbrücken

2019

Tag des Kolloquiums:	01.10.2019
Dekan:	Univ.-Prof. Dr. rer. nat. Guido Kickelbick
Berichterstatter:	Prof. Dr.-Ing. Stefan Seelecke Prof. Dr.-Ing. Stefan Diebels
Vorsitz:	Prof. Dr.-Ing. Georg Frey
Akad. Mitarbeiter:	Dr. rer. nat. Tilman Sauerwald

## Kurzfassung

Dielektrische Elastomere (DE) bieten sich durch ihre Vorteile gegenüber herkömmlichen Aktoren und Sensoren für viele Anwendungen an. Sie zeichnen sich aus durch geringes Gewicht, hohe Energieeffizienz, geräuschlosen Betrieb und inhärente Dehnbarkeit. Um die Entwicklung neuer DE Anwendungen voranzutreiben, werden effiziente Auslegungsprozesse benötigt. Zusätzlich sind numerische Methoden zur Optimierung solcher Prozesse von Interesse.

Der erste Teil dieser Dissertation entwickelt fortgeschrittene Entwicklungsmethoden für Aktor- und Sensorsysteme. Für DE Aktoren werden Systeme mit Permanentmagneten als Vorspannmechanismus untersucht und eine Prozedur zur Maximierung des Aktorhubs für eine vorgegebene Last hergeleitet. Für DE Sensoren wird das Feld der Hochdruckmessung erschlossen, indem Konzepte für intrusive und nicht-intrusive Druckmessungen entwickelt werden.

Der zweite Teil dieser Dissertation leitet numerische Modelle für die Simulation von DE Aktoren basierend auf der Finite Elemente Methode her. Der Hauptfokus liegt hierbei auf schnellen Rechenzeiten und numerischer Effizienz. Der erste diskutierte Ansatz basiert auf einer zweidimensionalen Kontinuumsformulierung, während der zweite Ansatz auf einer dreidimensionalen Membranformulierung basiert. Die resultierenden Modelle erlauben die Untersuchung lokaler Feldverteilungen, beispielsweise der mechanischen Spannung, der Dickenänderung und dem elektrischen Feld.



## Abstract

Dielectric elastomers (DEs) offer their use in numerous applications, due to their advantages compared to conventional actuators and sensors. They excel in properties such as lightweight, energy efficiency, low-noise and inherent compliance, just to name a few. In particular, actuator and sensor systems based on membrane DEs show their potential in many fields, from the automotive industry to consumer electronics. Defined procedures which permit an efficient design process are required in order to allow the development of novel DE devices. Additionally, numerical methods for the optimization of such processes are of interest.

The first part of this dissertation provides advanced design methods for actuator and sensor applications. For DE actuators, systems biased with permanent magnets are investigated and design rules are derived in order to maximize the stroke for a given load case. For DE sensors, the field of high pressure measurements is developed, introducing concepts for intrusive and nonintrusive sensor systems.

In the second part of this dissertation, numerical methods for membrane DE actuators based on the Finite Element method are derived. The main focus is fast computation time and numerical efficiency. Two approaches are presented, one based on a two-dimensional continuum formulation and one based on a three-dimensional membrane formulation. The resulting models allow the investigation of local field distributions, such as stresses, thickness and electric field.



## Acknowledgements

First and foremost, I would like to thank Prof. Stefan Seelecke for rendering this thesis possible. His constant encouragement, enthusiasm and guidance in the last five years have been invaluable.

At our lab, I have to give thanks to all my co-workers for not only a productive, but also pleasant work environment. Special thanks go to Daniel Bruch, Gianluca Rizzello and Marc Williams for their helpful and constructive discussions concerning all parts of my work.

I also acknowledge the companies *Bürkert GmbH*, *Continental AG*, *Medtron AG*, *Parker Hannifin Corporation* and *Wacker Chemie AG* for their material and financial support.

Special thanks go to my deep friends Jonas Wahl, Marvin Hahn and Michael Schnepf, for their emotional support and for taking my mind off things when it was necessary. Further, I am grateful to my family for their encouragement, especially to my sister Anna.

Franziska, you are the anchor in my life, thank you for your love and patience.



# Contents

<b>List of Symbols</b>	<b>ix</b>
<b>1 Introduction</b>	<b>1</b>
1.1 Motivation . . . . .	1
1.2 Research Objective and Thesis Remainder . . . . .	2
<b>I Advanced Actuator and Sensor Design</b>	<b>5</b>
<b>2 Fundamentals of Dielectric Elastomers</b>	<b>7</b>
2.1 Operation Principle . . . . .	7
2.2 Membrane Dielectric Elastomer Actuators . . . . .	9
2.3 Membrane Dielectric Elastomer Sensors . . . . .	14
<b>3 Advanced Biasing Methods Based on Permanent Magnets</b>	<b>17</b>
3.1 Concept of Actuator Biasing . . . . .	18
3.1.1 Biasing with Linear Elements . . . . .	18
3.1.2 Systematic Force Analysis . . . . .	23
3.1.3 Stability Analysis . . . . .	25
3.1.4 Biasing with Nonlinear Elements . . . . .	30
3.2 Biasing with Permanent Magnets . . . . .	32
3.2.1 Design of Stable Systems with Biasing Magnets . . . . .	34
3.2.2 Design of Stable Systems with Combined Biasing Elements . . . . .	36
3.2.3 Performance Improvement for Unstable Actuator Systems . . . . .	41
3.2.4 Experimental Validation and Discussion of Results . . . . .	42
3.3 Summary and Future Work: Permanent Magnet Biasing . . . . .	45
<b>4 High Pressure Sensors Based on Dielectric Elastomer Technology</b>	<b>47</b>
4.1 Intrusive Membrane Pressure Sensor . . . . .	48
4.1.1 Increase of Pressure Range Utilizing a Transmission Barrier . . . . .	49
4.1.2 Characterization of the Transmission Barrier . . . . .	50
4.1.3 Sensor Design, Manufacturing and Characterization . . . . .	53
4.1.4 System Design and Housing . . . . .	56
4.1.5 Experimental Validation and Discussion of Results . . . . .	58

4.2	Nonintrusive Membrane Pressure Sensor for Polymer Tubes . . . . .	60
4.2.1	Nonintrusive Concept: Stack Versus Membrane Sensors . . . . .	62
4.2.2	Characterization of the Pressurized Polymer Tube . . . . .	63
4.2.3	Sensor Modeling, Design, Manufacturing and Mounting . . . . .	65
4.2.4	Experimental Validation and Sensor Comparison . . . . .	71
4.2.5	Further System Enhancements . . . . .	74
4.2.6	Discussion of Results . . . . .	76
4.3	Summary and Future Work: High Pressure Sensors . . . . .	77
<b>II</b>	<b>Efficient Finite Element Modeling of Membrane Dielectric Elastomer Actuators</b>	<b>79</b>
<b>5</b>	<b>Fundamentals</b>	<b>81</b>
5.1	Continuum Mechanics . . . . .	82
5.2	Electrostatics for Continuous Bodies . . . . .	86
5.3	Finite Element Modeling with Comsol Multiphysics . . . . .	89
<b>6</b>	<b>Finite Element Modeling of Plane Strain Geometries</b>	<b>93</b>
6.1	Simplifications for Two-Dimensional Continuum Modeling . . . . .	93
6.2	Hyperelasticity and Viscoelasticity . . . . .	95
6.3	Electromechanical Coupling . . . . .	97
6.4	Parameter Identification and Model Validation . . . . .	100
6.5	Effects of Discretized Electrodes . . . . .	107
6.6	Discussion of Results . . . . .	110
<b>7</b>	<b>Finite Element Modeling of Three-Dimensional Membrane Geometries</b>	<b>113</b>
7.1	Discretization of Three-Dimensional Membrane Structures . . . . .	114
7.2	Electromechanical Coupling for a Membrane Formulation . . . . .	115
7.3	Model Validation and Comparison to Two-Dimensional Model . . . . .	117
7.4	Effects of Patterned Electrodes . . . . .	120
7.5	Discussion of Results . . . . .	122
<b>8</b>	<b>Conclusion and Outlook</b>	<b>125</b>
	<b>List of Figures</b>	<b>127</b>
	<b>List of Tables</b>	<b>131</b>
	<b>Bibliography</b>	<b>133</b>

## List of Symbols

$\beta$	.....	Viscoelastic energy factor
$\boldsymbol{\sigma}$	.....	Cauchy stress tensor
$\boldsymbol{\sigma}^{MW}$	.....	Maxwell stress tensor in terms of Cauchy stress
$\epsilon$	.....	Strain
$\lambda_i$	.....	Principal stretches
$\lambda_n$	.....	Transversal stretch
$\mathbf{C}$	.....	Cauchy-Green deformation tensor
$\mathbf{E}^{GL}$	.....	Green-Lagrange strain tensor
$\mathbf{F}$	.....	Deformation gradient
$\mathbf{F}_N$	.....	Normal component of deformation gradient
$\mathbf{F}_T$	.....	Tangential component of deformation gradient
$\mathbf{I}$	.....	Identity tensor
$\mathbf{P}$	.....	First Piola-Kirchhoff stress tensor
$\mathbf{Q}_i$	.....	Non-equilibrium stress tensor
$\mathbf{S}$	.....	Second Piola-Kirchhoff stress tensor
$\mathbf{S}^{MW}$	.....	Maxwell stress tensor in terms of second Piola-Kirchhoff stress
$\mathbf{S}_{iso}^\infty$	.....	Quasi-static isochoric second Piola-Kirchhoff stress tensor
$\Psi$	.....	Mechanic Energy
$\psi_e$	.....	Electric energy density
$\psi_s$	.....	Strain free-energy density
$\tau$	.....	Dashpot relaxation time
$\hat{\mathbf{N}}$	.....	Normal vector in reference configuration
$\hat{\mathbf{n}}$	.....	Normal vector in current configuration

## List of Symbols

---

$\varepsilon_r$	Relative permittivity
$\varphi$	Electric scalar potential
$\varrho_0$	Electric charge density
$\mathbf{D}$	Electric displacement field vector
$\mathbf{E}$	Electric field vector in reference configuration
$\mathbf{e}$	Electric field vector in current configuration
$\mathbf{T}$	Stress vector in reference configuration
$\mathbf{t}$	Stress vector in current configuration
$\mathbf{u}$	Displacement vector
$A$	Surface area
$C$	Electric capacitance
$C_i$	Yeoh material parameters
$d$	Thickness
$F$	Force
$g$	Gravitational constant
$I_1$	First invariant of Cauchy-Green deformation tensor
$J$	Local volume ratio
$k$	Spring stiffness
$m$	Mass
$p$	Pressure
$r$	Radius
$Y$	Young's modulus

# 1 Introduction

Nowadays, many applications demand actuator and sensor systems which offer properties such as compactness, lightweight, energy efficiency, flexibility and low-cost manufacturing. The fast progress in robotics and the biomedical field especially develop a need for such devices. Smart materials, such as piezoelectric ceramics, shape memory alloys, magnetorheological fluids and many more, show their suitability in the aforementioned fields of research. Their applications range from positioning actuators to high frequency noise cancellation [1, 2]. Furthermore, many smart materials show properties which are desirable in the medical field, such as biocompatibility and sterilizability. The materials of interest in this thesis are dielectric elastomers (DEs), which belong to the group of electro-active polymers. Their suitability has been shown in numerous applications as actuators [3], sensors [4, 5], and generators [6, 7]. Although the physical effect has already been described by Röntgen in 1880 [8], the main research originates at Stanford Research Institute International in the early 1990s with the work of Pelrine *et al.* [9].

## 1.1 Motivation

Recently, more and more applications for DEs are proposed in literature, especially in the field of intelligent actuator systems. Advantages of DEs are harnessed, which include large deformations up to 200 % [10], low cost manufacturing, inherent compliance and fast actuation, to name just a few. Standardized design approaches have been established, including different DE actuator (DEA) topologies. For membrane actuators, there is a fast development need for large stroke [11] or high force [12] actuators based on linear and nonlinear biasing mechanisms in order to accomplish such high-performance tasks. Based on the nature of DEs as a smart material, a sensor-less position control is rendered possible and discussed, which is known as the self-sensing effect [13]. Hence, DEs represent a highly attractive technology for future systems, with a focus on robotics, smart wearables and health monitoring applications. However, the design concepts for actuator and sensor systems can be improved in order to enhance the overall performance. For predicting the behavior of DEA systems, different numerical simulation approaches exist, based on lumped elements or distributed models, i.e., the Finite Element (FE) analysis. Based on such models, a more detailed system optimization can be performed without conducting experimental studies. Furthermore, for distributed models,

the effect of different electrode shapes and a locally distributed thickness can be studied in detail.

## 1.2 Research Objective and Thesis Remainder

In this thesis, enhancements of existing design concepts and the development of novel design processes are the main goal. In order to accomplish this task, three fields of DE research are enhanced with advanced concepts. Part I of this thesis covers actuator and sensor systems, which includes performance enhancements of actuator systems biased with attracting permanent magnets and sensor systems for high pressure applications, introducing an intrusive and a nonintrusive concept. In Part II, FE modeling strategies for membrane DE actuators are investigated, focusing on fast computation time and numerical efficiency. The development of a model for large deformations is the main task, which includes hyperelasticity, viscoelasticity and different approaches for the electromechanical coupling due to the application of high voltage. To achieve these aims, this thesis is organized as follows.

**Chapter 2** gives an introduction into the fundamentals of DE technology. Operation principles for actuators and sensors are declared, together with the manufacturing process and electromechanical characterization.

**Chapter 3** discusses actuator systems based on out-of-plane membrane DEAs. The overall concept of biasing this type of actuators with linear and nonlinear mechanisms is presented. A systematic force analysis is examined, together with a stability analysis for distinct biasing elements. These concepts are employed in order to develop an actuator system biased with permanent magnets to enhance system performance. The performance of such systems can be improved further by adding an additional linear element. An advanced design process is introduced to increase robustness of a large stroke actuator system, both for stable and unstable system behavior. The work in this chapter has also been reported in [14, 15].

**Chapter 4** examines DE sensors for high pressure measurements. State-of-the-art pressure sensors based on DE technology are suitable for a low pressure range in the order of 1 bar due to the small mechanical forces a DE is able to endure. Based on the concept where pressurized medium and DE are separated, an intrusive sensor design for pressures up to 10 bar is introduced, followed by a nonintrusive design for measuring pressures up to 62 bar inside a polymer tube. The work in this chapter has also been reported in [16, 17], as well as in the patent [18].

**Chapter 5** gives an introduction to the second part of this thesis, which is based on FE modeling of DEAs. Required fundamentals of continuum mechanics, electrostatics and FE modeling in Comsol Multiphysics are provided.

**Chapter 6** introduces a FE model for membrane DEAs in a pure shear configuration. A reduction to a two-dimensional model discretized with continuum elements is described, including large deformations, hyperelasticity, viscoelasticity and electromechanical coupling. Additionally, the model includes separately discretized electrodes in order to investigate the electrode influence onto local fields. The model is validated for a strip in-plane membrane actuator. The work in this chapter has also been reported in [19, 20].

**Chapter 7** enhances the work of Chapter 6 for arbitrary geometries. A FE membrane formulation is developed which includes large deformations, hyperelasticity, viscoelasticity and electromechanical coupling. Due to the membrane formulation, faster computation times are achieved and thickness distributions can be investigated. The membrane model is validated for a strip in-plane membrane actuator and compared to the results of Chapter 6. The work in this chapter has also been reported in [21].

**Chapter 8** gives a conclusion to the thesis and provides future research topics.



## **Part I**

# **Advanced Actuator and Sensor Design**



## 2 Fundamentals of Dielectric Elastomers

Dielectric Elastomers belong to the material group of electro-active polymers. As a representative of smart materials, their main feature is a change in shape induced by an electric field applied across the material. This behavior can be harnessed in actuator systems, whereas the inverse effect is utilized for generator systems. Additionally, sensor systems can be developed based on DE technology due to their change of electric capacitance while deforming under an external load. A further important feature is the so called self-sensing effect, which correlates deformation to the electric capacitance while using the DE as an actuator. This feature offers sensor-less control of the deformation state [22]. In this chapter, the fundamentals of DE technology are presented. Starting with the overall physical principle, different materials and configurations are briefly discussed and compared. The actuation mechanism for DE membrane actuators is described, followed by the manufacturing process and the electromechanical characterization. Finally, the physical principle of DE sensors (DES) and several applications are presented, stating their advantages over conventional sensor systems. More detailed discussions on those fundamentals can be found in [23, 24].

### 2.1 Operation Principle

A DE consists of a compliant polymer film sandwiched between two compliant electrodes. Its basic structure is shown in Figure 2.1.

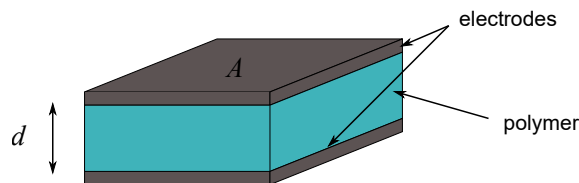


**Figure 2.1:** Basic structure of a DE: a polymer film is sandwiched between two compliant electrodes, building a highly flexible capacitor.

Property	Value		Unit
	Acrylics DE	Silicones DE	
Maximum actuation strain	380	120	%
Maximum actuation stress	8.2	3	MPa
Maximum frequency response	>50	>50	kHz
Maximum energy density	3.4	0.75	MJ/m <sup>3</sup>
Maximum electric field	440	350	MV/m
Relative permittivity (at 1 kHz)	4.5 – 4.8	2.5 – 3	-
Dielectric loss factor (at 1 kHz)	0.005	<0.005	-
Mechanical loss factor	0.18	0.05	-
Young Modulus	0.1 – 3	0.1 – 2	MPa
Maximum electro-mechanical coupling	0.9	0.8	-
Maximum overall efficiency	>80	>80	%
Durability	>10 <sup>7</sup>	>10 <sup>7</sup>	cycles
Operating range	-10 – 90	-100 – 260	°C

**Table 1:** Performance of best acrylics and silicones DEs [28].

From an electrical point of view, the formed structure is a highly flexible parallel plate capacitor, whose capacitance can be computed as

$$C = \varepsilon_0 \varepsilon_r \frac{A}{d}, \quad (2.1)$$

where  $\varepsilon_0$ ,  $\varepsilon_r$ ,  $A$  and  $d$  refer to the vacuum permittivity, relative permittivity of the elastomer, surface area of the DE electrodes, and thickness of the polymer film, respectively. For incompressible polymer films, an increase in area  $A$  simultaneously leads to a decrease in thickness  $d$ , and vice versa. Both effects lead to an increase in capacitance, as equation (2.1) states. This principle can be exploited to design DE actuators [25], sensors [26] and energy harvesters [27]. The requirements to the polymer material are high flexibility, a large electric breakdown strength and small mechanical losses. Therefore, the main materials used for the polymer film can be divided in three main groups, namely acrylics (e.g., 3M VHB 4910), silicones (e.g., Wacker Elastosil 2030) and natural rubber. Research focuses on the first two, acrylics and silicones, as material for sensor and actuator applications. The main features of both material groups are listed in Table 1 [28]. The main differences between acrylics and silicones are the larger actuation strain and relative permittivity for acrylics, while silicones offer much smaller mechanical losses, leading to smaller hysteretic behavior. All actuators and sensors described in this thesis are based on silicone as a polymer film, due to the small mechanical hysteresis, which is crucial for repeatable actuator performance. For the compliant electrodes, a mixture of conducting particles (mostly carbon black) and silicone is used, due to its flexibility and sufficient conductive properties. An overview on different electrodes is given by Rosset and Shea [13]. The electrodes are supposed to provide a small increase in stiffness while maintaining

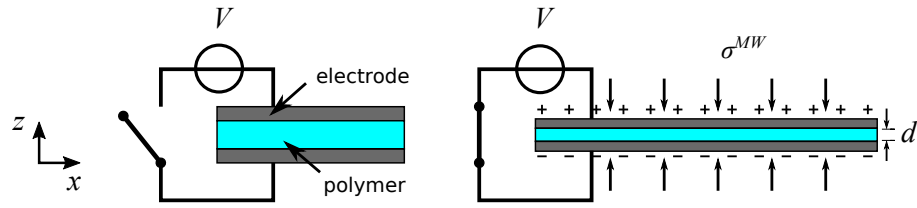


**Figure 2.2:** Due to an electrical voltage  $V$ , the DEA is charged, leading to an increase in surface area  $A$  and a reduction in thickness  $d$ .

adequate electrical conductivity. The influence of different manufacturing parameters when utilizing screen-printing is examined by Fasolt *et al.* [29].

There are two major DE configurations, namely stacks [30, 31, 32] and membranes [33], each of them offering different advantages. On the one hand, a DE stack consists of several DE layers stacked on top of each other. The dominant effect of stack actuators and sensors is the thickness compression of every layer, due to an external force (sensor) or an applied electric field (actuator). A membrane DE, on the other hand, usually consists of a single membrane, which makes use of the area expansion, again due to an external force or an electric field. There are different configurations of membrane actuators, which can be divided in in-plane and out-of-plane actuators, rolls [34] and tubes. For in-plane and out-of-plane, the two main topologies are strips and cones. In this thesis, only membrane DEAs are investigated and advanced design methodologies are derived. For actuator systems, cone DEs are examined in this thesis, while for sensor systems, strip DEs and cone DEs are utilized. The following section discusses main features of membrane DEAs, focusing on out-of-plane deflecting actuators.

## 2.2 Membrane Dielectric Elastomer Actuators

Membrane DEAs usually consist of one DE layer only. The actuation principle bases on its electrical structure, which is a parallel plate capacitor and shown in Figure 2.2. When electrical energy is induced, in terms of an applied high voltage  $V$  onto the electrodes, the capacitor charges. The opposing unlike charges attract each other, as Coulomb's law states, leading to a reduction in thickness. Equally, like charges repel each other, leading in combination with the elastomer's incompressibility to an increase in area. Typical applied voltages depend on the thickness of the polymer film as well as its relative permittivity  $\epsilon_r$ . A common voltage range is between 1 and 10 kV [35]. This process is shown in Figure 2.2. The induced stress, which couples the mechanical with the electrical properties, is known as the Maxwell stress [36]. It can be reduced from its three-dimensional tensor form to one component  $\sigma^{MW}$  normal to the membrane due to the assumption of a homogeneous electric field with only one component in

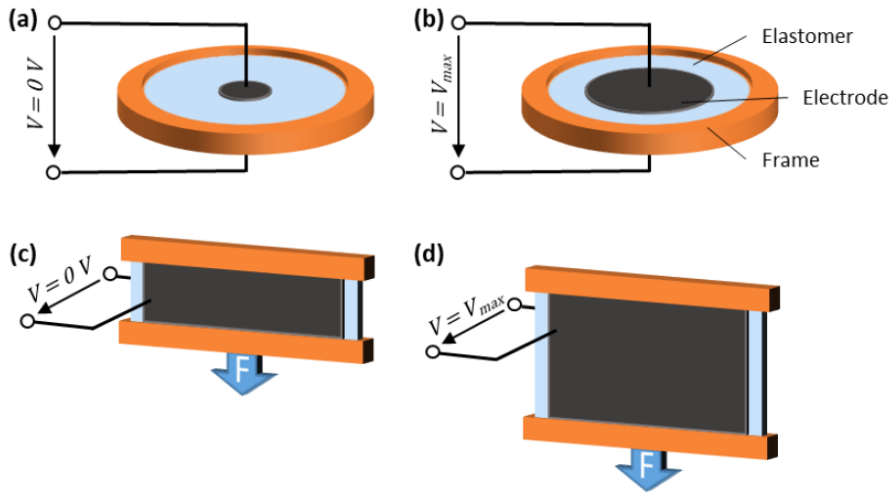


**Figure 2.3:** CIP DEA biased by a pre-stretch of the elastomer film at 0 V (a) and at high voltage (b), and SIP DEA biased by an external force  $F$  at 0 V (c) and at high voltage (d) [23].

$z$ -direction according to the coordinate system in Figure 2.2. In this case, the Maxwell stress calculates to

$$\sigma^{MW} = -\epsilon_0 \epsilon_r E_z^2 = -\epsilon_0 \epsilon_r \left( \frac{V}{d} \right)^2, \quad (2.2)$$

with  $E_z$  being the aforementioned electric field normal to the electrodes. This approximation is feasible for parallel plate capacitor like structures. A detailed derivation of this correlation has been developed by Pelrine *et al.* for flexible, incompressible capacitors [37].

In Part I of this thesis, the approximated form of the Maxwell stress in equation (2.2) is sufficient for all actuator considerations. In context with FE modeling in Part II of this thesis, the general form of the Maxwell stress tensor is discussed in detail. This effect is known as electromechanical coupling due to the interaction of electrostatics and mechanics. It is bounded by the material's electrical breakdown strength. Typical values for the breakdown strength of silicone are in the range of  $80 \text{ V}/\mu\text{m}$  to  $130 \text{ V}/\mu\text{m}$  [38]. Membrane DEAs mainly use the increase in area for actuation, therefore produce large deformations, but small reaction forces. In order to increase the reaction force, several membranes can be stacked, which connects all of them mechanically in parallel. Thus, the force scales with the number of DEA layers [12]. Based on this physical principle, several applications for DEAs are proposed in literature, reaching from loudspeakers [39] to optical switches [3], pumps [40, 41, 42], valves [43], high-force actuators [44], robots [34, 45, 46], micro positioners [47] and grippers [48, 49].

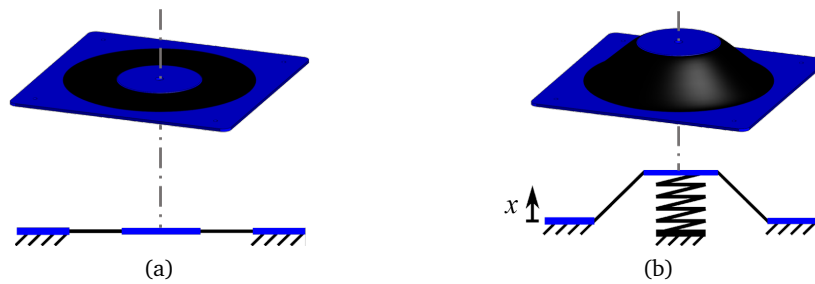


**Figure 2.4:** A COP DEA, without biasing (a) and biased out-of-plane with a linear spring (b).

Two different types of deformation are distinguished, namely in-plane deformation and out-of-plane deformation. In-plane actuators generate a deformation in the membrane plane. In order to accomplish this deformation, the DEA needs some kind of pre-stress. Otherwise, the membrane surface area increase would lead to a wrinkling of the membrane [50], but no induced preferred direction of deformation exists. Additionally, biasing the membrane influences the actuator performance and breakdown strength [51]. This biasing can be induced by a pre-stress of the membrane during manufacturing, or by a biasing element, e.g., a hanging mass or a spring [52] (further details in Section 3.1). Often used geometries are strip in-plane (SIP) DEAs [53] and circular in-plane (CIP) DEAs [10]. Figure 2.3 shows schematics for CIP and SIP actuators.

Out-of-plane actuators generate a deformation normal to the undeflected membrane. Similar to in-plane actuators, a biasing element is mandatory in order to direct the increase in area to a defined deformation in the desired direction. Typical biasing elements are similar to in-plane actuators and described in detail in Chapter 3. Common form factors are circular out-of-plane (COP) [47] and strip out-of-plane (SOP) DEAs [54, 55]. Figure 2.4 shows schematics for a biased COP DEA.

In order to build actuator systems, the DEAs must be manufactured and characterized. Especially the electromechanical characterization is a crucial step towards a working system for every type of DEA, because the system design is entirely based on those measurement. Since silicone films are commercially available (for example Elastosil 2030 by *Wacker AG*), the main task is the application of compliant electrodes. Typical methods are pad printing [56], inkjet printing [57], spray coating [31] or laser ablation [58]. For mass manufacturing, screen-printing offers its advantages, such as low-cost production, scalability and a high repeatability [59]. At the beginning of the screen-printing process, the silicone film is pre-stretched in order to enhance actuator performance and increase the breakdown voltage [60], as mentioned before. Additionally, pre-stretching avoids any wrinkling during printing, since the thin silicone films offers only small mechanical stiffness. The desired electrode pattern is applied onto a screen in a lithographic process. The screen is then used to apply the electrode ink onto the silicone film. A heat curing process is afterwards used, in order to link silicone and electrode.

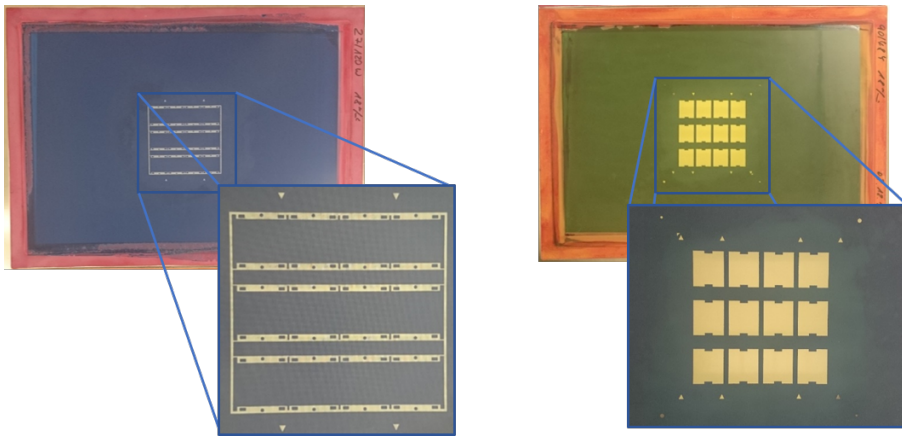
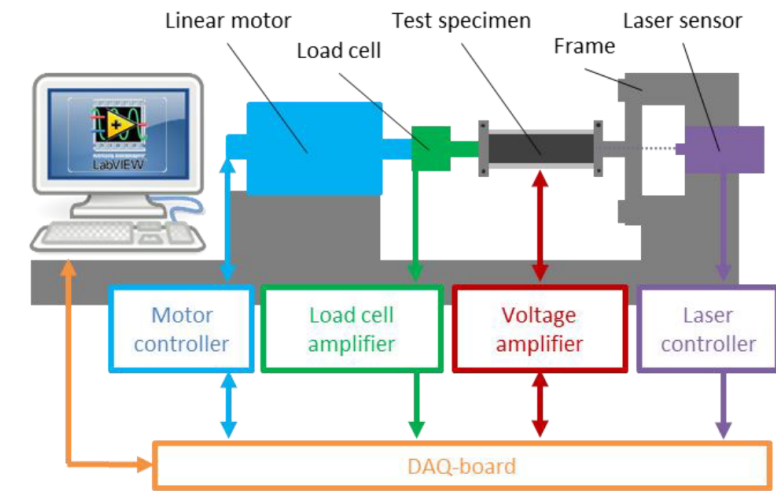


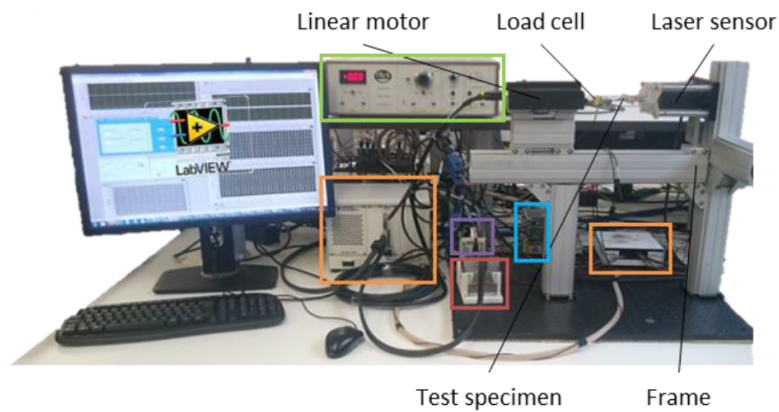
**Figure 2.5:** Two screens for printing SIP DEAs, the epoxy frame (left) and the electrodes (right) [23].

For mechanical stabilization, an epoxy frame is printed around the electrode to improve the handling after manufacturing. Two screens, one for electrode and one for frame printing of a SIP DEA are shown in Figure 2.5. Due to the freedom in designing the screen, arbitrary electrode geometries can be manufactured. Furthermore, in an actuator design process, different geometry parameters have a large influence on the actuator performance [61]. Such parameters can be varied in order to investigate sensitivities and find the optimal DEA for given system specifications. More details on the manufacturing of DEAs via screen-printing can be found in [62].

For the design of actuator systems based on DEAs, an electromechanical characterization is of utmost importance. The force-displacement characteristic needs to be determined in order to systematically design a system consisting of DEA and biasing mechanism. The test rig shown in Figure 2.6 is designed to accomplish these characterization tasks. The setup consists of a linear actuator, which is connected to a load cell. The test specimen shown in Figure 2.6 is a SIP DEA, which is attached to the motor at one side while the other side is fixed. When the linear actuator pulls on the DEA, a laser sensor measures the displacement and the force is recorded by a load cell. During the experiments, the DEA is deflected from zero to a maximum strain value, which is dependent on the actuator size. The measurement is taken for several cycles and with different actuation frequencies, in order to characterize the force-displacement as well as the viscoelastic behavior. These experiments are performed at different voltages applied. To control the setup and perform data acquisition, a NI LabVIEW interface is implemented based on a FPGA for real-time measurements. The resulting force-displacement curves are shown in Figure 2.7, exemplary for a COP DEA. The blue dashed curve represents a measurement without applied voltage, whereas for the red dashed curve a high voltage is applied. As one can see, the stiffness of the actuator is decreasing due to the high voltage application. This behavior is expected, as the applied high voltage induces the Maxwell stress, as equation (2.2) states, which increases the surface area of the DEA. While the voltage increases, the character-



(a)



(b)

**Figure 2.6:** Experimental setup to characterize DEA, schematics (a) and real setup (b) [23].

istic curve shifts from the blue zero volt curve until it reaches the red curve with the maximal voltage applied. In this process, it passes over the green marked work area. The work area, which has been described in detail by Hodgins [24], is the area in which the actuator is able to maintain a force equilibrium with a biasing element and/or an external load. Outside this area, no force equilibrium is possible. The larger the work area, the more versatile is the DEA to adapt to different load profiles. Note that any voltage level is prohibited, which exceeds the electric breakdown strength of the material. The reduction of thickness while deforming a DE membrane must be considered as well, because the electric field rises inversely proportional to the film thickness. Additionally, the breakdown voltage is strain dependent [63], making the choice of a maximal applicable voltage more complex.

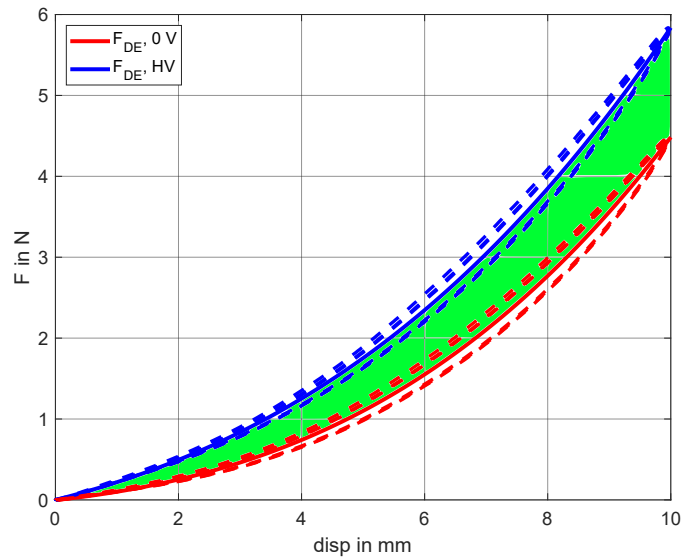


**Figure 2.7:** Characteristic force-displacement curves of a DEA, without voltage (blue) and with applied high voltage (red). The green area displays the actuator's work area.

Another important observation is the hysteretic behavior of the DEA. The hysteresis consists of the silicone viscoelasticity and the electrode viscoelasticity. Within the manufacturing process, it is desired to keep the hysteresis of the electrode material as small as possible, in order to increase the work area. Also, the hysteresis enlarges with actuation frequency. For high frequency applications, such as loudspeakers or positioning stages [39, 47], the hysteresis contributes remarkably to the system performance. A detailed discussion on the effect of different electrodes onto the hysteretic behavior can be found in [59]. In this thesis, the design process for actuator systems is approximated for low frequencies only and thus the hysteresis is neglected. Figure 2.7 shows averaged zero volt and high volt curves (solid blue and red lines) inside the dashed measurement curves. This approximation is repeated for all actuator designs, as well as the qualitative description of biasing elements and stability analysis in this thesis.

### 2.3 Membrane Dielectric Elastomer Sensors

Apart from actuation, DEs also offer their potential as sensors. Basically, a DE is a compliant capacitor. Any deformation results in a change in capacitance. Figure 2.8 shows a DE sensor (DES), which is deformed by an external load  $F_{ext}$ . The deformation leads to a decrease in thickness from  $d_0$  to  $d_1$ . Incompressibility yields a simultaneous increase in area from  $A_0$  to  $A_1$ . As stated in equation (2.1), the DE structure resembles a parallel plate capacitor, therefore the capacitances of both configurations calculate to

$$C_0 = \varepsilon_0 \varepsilon_r \frac{A_0}{d_0} \quad \text{and} \quad C_1 = \varepsilon_0 \varepsilon_r \frac{A_1}{d_1}, \quad (2.3)$$

with the capacitance change  $\Delta C$  resulting in

$$\Delta C = C_1 - C_0 = \varepsilon_0 \varepsilon_r \left( \frac{A_1}{d_1} - \frac{A_0}{d_0} \right). \quad (2.4)$$

The remarkable change in capacitance due to large strains up to 200 % results in a sensitive and flexible sensor structure [64]. Advantages of DES are their high sensitivity and low-cost manufacturing. There is no comparable sensor technology, which combines the level of accuracy with high flexibility, making DES suitable for numerous applications, e.g., the European *SENSKIN* [65] introduces DES for measuring the deformation of motorway bridges. Here, the overall stretch changes over the year, due to the thermal expansion of the bridge. The DES is able to adapt the operating point over the year, while still measuring small changes around the operating point.

Similar to actuators, two different DES configurations exist, stack sensors and membrane sensors. Whereas stack sensors are focusing on measuring a decrease in thickness (e.g., compression), membrane sensors are focusing on an increase in area (e.g., stretches). In addition to the capacitance measurement, also the resistance of the sensor changes with deformation, which is exploited in [66]. The manufacturing process for DES is equivalent to actuators. For the characterization of DES, the same test rig shown in Figure 2.6 is used. However, instead of an electrical actuation, a capacitance measurement is performed, in order to obtain the sensor characteristics, which is deformation versus capacitance change. Hereby, the capacitance is an intermediate quantity. The to be measured quantity is correlated to the capacitance change through a calibration. Figure 2.9 shows a diagram with different application fields for DES, reaching from established sensor applications to new fields such as soft robotics and structural health monitoring. Recent literature proposes DE sensors for traditional sensor applications,

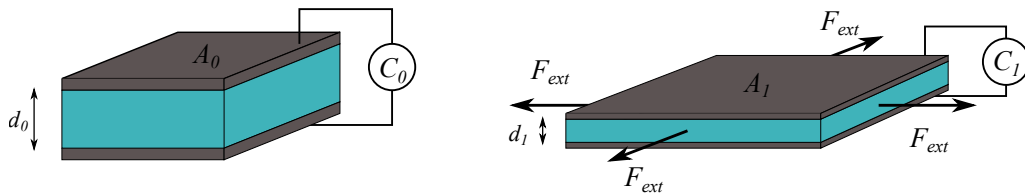


**Figure 2.8:** An external force leads to an increase in area and a decrease in thickness, both increasing the capacitance.

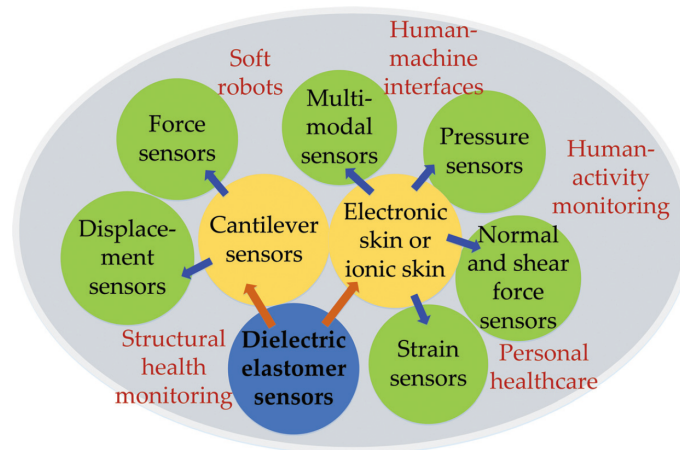


**Figure 2.9:** Application field for DES, reaching from health monitoring to soft robotics, also covering typical sensor applications such as force, displacement and pressure sensors [26].

such as force sensors [67, 68], and large strain sensors [65]. Latter are commercially available, for example, by *StretchSense* [69], *ElastiSense* [70] and *Parker Hannifin* [71]. Pressure sensors based on DES are proposed in literature, reaching from polyurethane films with gold metallization [72] over fluidic sensors [4] and capacitive compression sensors [73]. All these pressure sensor concepts have in common, that the pressure range is restricted, a maximum pressure of 1 bar is reached in [72]. This is due to the soft characteristic of a DES, which is damaged under high loads. A first attempt to overcome this restriction is proposed in the second half of [4], where a transmission barrier is introduced in order to translate higher pressures to a deformation, which then is measured by the DES.

Overall, DES cover a large field of applications. In this thesis, the field of pressure sensing is extended by high pressure sensors. The limit of the low pressure regime is overcome in Chapter 4 by introducing concepts for designing pressure sensors based on DE technology, an intrusive concept for pressures up to 10 bar and a nonintrusive concept for pressures up to 62 bar.

### 3 Advanced Biasing Methods Based on Permanent Magnets

As discussed in Chapter 2, there are many different types of membrane DEAs, ranging from rolls over strips to cone-shaped actuators. This thesis focuses on cone-shaped out-of-plane (COP) DEAs, which are thoroughly examined in literature [38, 44, 74]. Exemplary for out-of-plane biasing, a linear biasing spring (LBS) is shown in Figure 2.4. In order to develop advanced design concepts for such actuator systems, the overall design process must be discussed thoroughly, including a detailed description of the for out-of-plane actuators required biasing elements. To optimize the actuator system performance, an appropriate combination of DEA and biasing mechanism must be chosen. Each element must be characterized to execute this optimization successfully. For actuator applications, not only the free stroke without an applied load matters, but also the performance against arbitrary loads is of interest. Especially the actuator design for a given load is an important aspect for industrial applications. Therefore, advanced design procedures which include external forces and adaption to given load profiles are highly demanded. Hau proposes such concepts for systems demanding high forces [23].

The development of advanced design concepts is the main goal of this chapter, which is divided in two parts. The first part covers biasing concepts for linear elements, such as a LBS or a hanging mass, and nonlinear elements, such as buckled beams [75] and joint mechanisms [76]. A systematic force analysis for the actuator design is presented, which outperforms design approaches based on basic force equilibria between DEA and biasing element. Additionally, stability of the resulting DE systems is discussed in detail. The second part utilizes those methods in order to develop an advanced design process for DEA systems biased with permanent magnets (PM). After designing a PM biased system, the combination of PM and a LBS is discussed, and the potential of using the instability of PM for performance increase. All optimized designs based on PM biased systems are experimentally characterized and compared to each other.

### 3.1 Concept of Actuator Biasing

The immense influence of biasing elements has been discussed by Hodgins *et al.* [52], especially the effect of negative-rate biasing springs (NBS) compared to LBSs. A significant stroke increase of an order of magnitude compared to LBSs can also be performed by using NBS [77]. These results emphasize the importance of studying the design process in detail. This section describes the design process, which is based on the force equilibrium between DEA and biasing element. An advanced description of force equilibria between DEA and biasing element, which has been discussed in [24], offers a comparison of the overall actuator system against an arbitrary load. After the discussion of linear biasing elements with positive rate, stability is discussed by introducing a fictive linear element with negative rate. Subsequently, nonlinear biasing elements and their advantages are introduced.

#### 3.1.1 Biasing with Linear Elements

The static design process of DE actuator systems is based on the force equilibrium between DEA and biasing element. The procedure is explicated based on linear elements. Linear elements, such as a hanging mass or a LBS, are depicted in Figure 3.1, with (a) showing the schematic structure of a system biased with a hanging mass  $m$ , including the force equilibrium and the representation of all forces in the coordinate system of the DEA. Note that the force equilibrium and the schematic structure are different representations of the same system. The biasing element forces for a hanging mass and LBS calculate to

$$F_m = mg \tag{3.1}$$

and

$$F_{LBS} = -k_L (x - x_0^L), \tag{3.2}$$

respectively, with  $g$  being the gravity constant,  $k_L$  the positive stiffness of the LBS and  $x_0^s$  the initial pre-compression of the spring. Note that the negative sign is due to the nature of this force as a restoring force of the spring working against the DEA in the DEA's coordinate system. The force equilibrium for the mass biased system calculates to

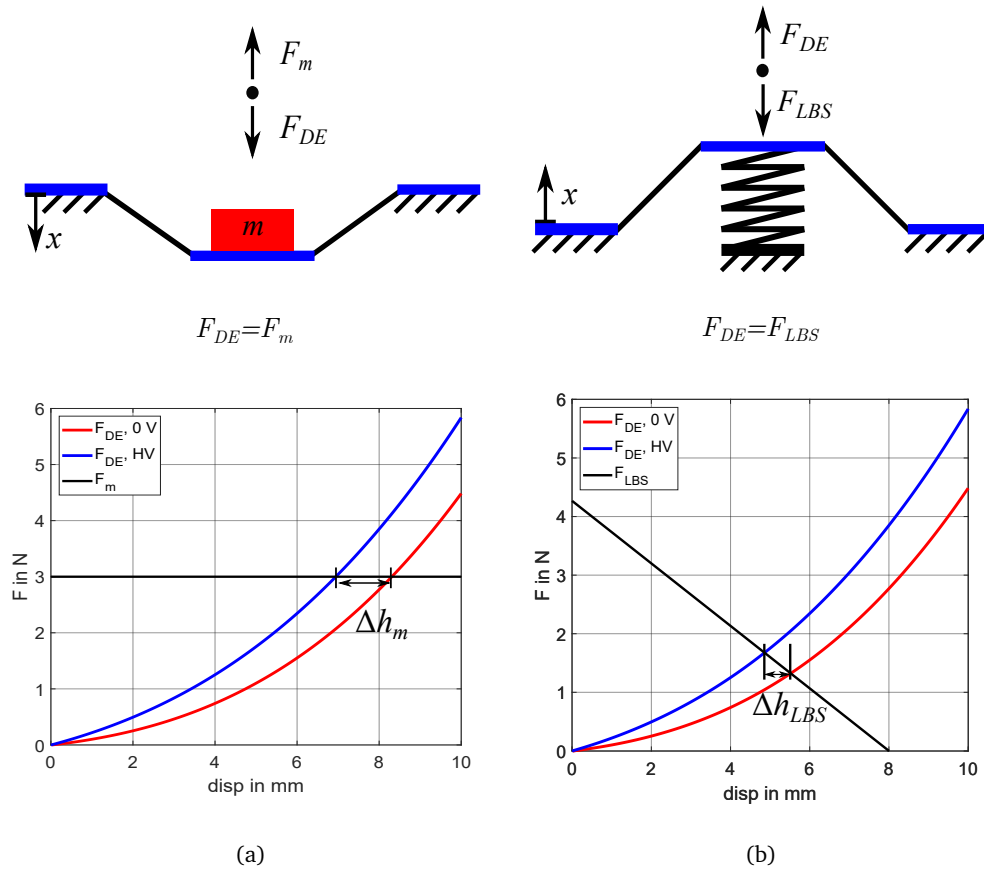


**Figure 3.1:** Example for linear biasing mechanisms and their force equilibrium with a DEA, for a hanging mass (a) and for a LBS (b). The hanging mass system produces a larger stroke than the LBS.

$$F_{DE} = F_m = mg . \quad (3.3)$$

The constant force of the hanging mass intersects with the force-displacement of the DEA, for 0V (blue curve) and for HV (red curve). The stroke produced by the actuator system is the difference from the 0V intersection to the HV intersection. It is shown for the hanging mass as  $\Delta h_m$  in the bottom left graph of Figure 3.1. The only design parameter for a system biased with a hanging mass is the mass  $m$ . Figure 3.1 (b) shows the same results for a system biased with a LBS, with the force equilibrium

$$F_{DE} = F_{LBS} = -k_L (x - x_0^L) . \quad (3.4)$$

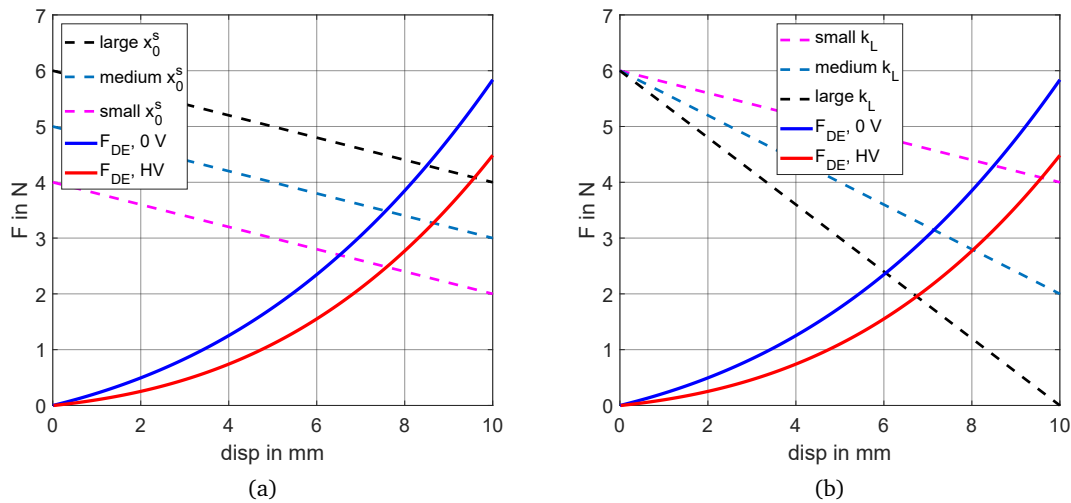


**Figure 3.2:** Parameter variations for LBS, change of spring pre-compression (a) and stiffness (b).

For this system, the stroke  $\Delta h_{LBS}$  is also sketched into the force-displacement graph. Compared to a hanging mass, the LBS offers two design parameters, namely the stiffness  $k_L$  and the pre-compression  $x_0^s$ . Comparing both biasing elements, there are advantages and disadvantages for each. The hanging mass always produces a larger stroke as any LBS biased system for the same DEA. This is due to the monotonically increasing slope of the DEA, while the LBS slope monotonically decreases in the reference frame of the DEA. As long as the LBS has a positive rate, the hanging mass with its constant force reaches a larger distance between both force equilibria, yielding the larger stroke. However, a hanging mass shows disadvantages such as oscillatory behavior due to inertia. Furthermore, the biasing force results from gravity, which prohibits a mass biased system to work when tilted or turned upside down. Due to the disadvantages of hanging masses as biasing mechanism, they are not discussed further in this thesis. As a comparison to nonlinear elements, a LBS biased system is used later on.

In order to make a statement on the robustness of the biasing mechanisms, parameter variations must be discussed. A variation of both parameters, namely spring stiffness  $k_L$  and pre-compression  $x_0^s$ , is shown in Figure 3.2. The spring pre-compression acts like a constant biasing force and shifts the LBS curve up with increasing value (Figure 3.2 (a)), while the stiffness changes the curve slope, which decreases with increasing stiffness (Figure 3.2 (b)). The robustness of LBS biasing becomes evident with these plots. A small deviation in stiffness or pre-compression changes the stroke output of the actuator only marginally. This is an upside of LBS biasing, because the system itself is hard to detune, and behaves intrinsically stable. Due to the linearity and a positive spring rate, the derivation of optimal design rules is fairly easy. In [15], the optimal design is described in detail. The stiffness of the LBS must be chosen small, while the pre-stress must be large. This combination yields a behavior such

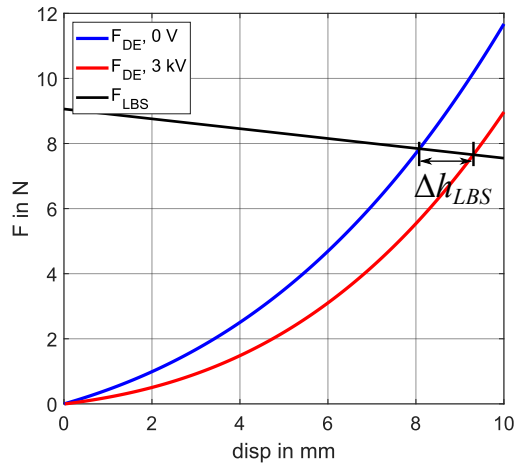


**Figure 3.3:** Optimal design for a LBS working against an 8 layered DEA, yielding a stroke of 1.2 mm.

as the hanging mass system, without its stated disadvantages. The limitation is the maximal mechanical stress the DEA is able to preserve.

In order to compare systems based on advanced design methods, which are developed in this chapter, to linear systems, the optimal design for a LBS system is performed. To achieve quantitative results, the utilized DEA must be specified. For all actuator systems in this chapter, cone shaped DEAs from *Parker Hannifin* are used [78]. These membranes exhibit an inner diameter of 20 mm and an outer diameter of 45 mm. Every actuator cartridge consists of 4 stacked DE layers, each one having a thickness of 45  $\mu\text{m}$ . The dielectric material is the commercially available silicone film SNES-18602-19RT5 from *Parker Hannifin*, coated with electrodes consisting of a silicone and carbon black mixture. All following designs are performed on actuator modules consisting of a stack of two cartridges, resulting in 8 DE layers. The design constraints are expressed in terms of a maximum out-of-plane displacement of 10 mm and a maximum voltage of 3 kV to avoid mechanical/electrical breakdown. In order to design a concrete LBS biased system, the spring stiffness and the initial spring compression need to be determined. Following the design rules discussed in this section, a spring stiffness  $k_L$  of 0.15 N/mm and a pre-compression  $x_0^s$  of 60 mm are chosen. The chosen spring is significantly softer than the DEA. Note that the optimal design would intuitively cross the HV curve at the largest deformation at 10 mm. However, the actuator stroke between the chosen design and the 10 mm design does only differ marginally, and driving the actuator in a larger deformation range results in a larger electric field, which could potentially damage the DEA faster. The result of this optimization is shown in Figure 3.3. The resulting stroke  $\Delta h_{LBS}$  equals 1.2 mm. From Figure 3.3, it can also be observed that the combination of DEA and LBS shows a clear disadvantage. In fact, only approximately 10 % of the large possible actuator stroke of 10 mm is exploited. This is mainly due to the fact that the force-displacement characteristics of LBS and DEA have opposite slopes in this reference frame. As a consequence, the resulting intersections

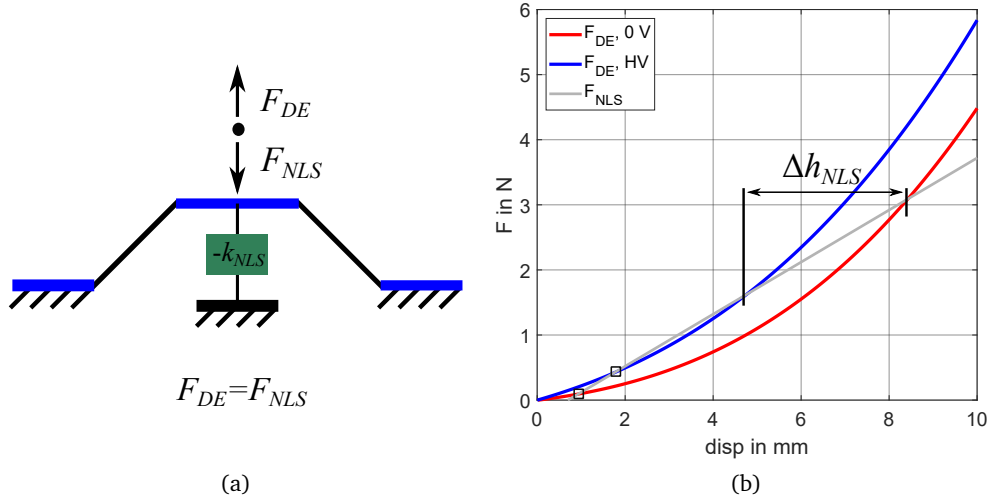


**Figure 3.4:** System design for a fictive biasing element with negative linear stiffness, including force equilibrium (a) and the corresponding force-displacement graph with resulting stroke.

are very close together, implying that the stroke is relatively small. To increase the actuator stroke, a biasing mechanism is required, whose characteristic curve resembles the shape of the DEA. There are different biasing elements offering a nonlinear characteristic, which also have a range of negative rate, which fits the DEA characteristic far better, such as beforementioned NBSs or joint mechanisms [76]. In this work, permanent magnets are presented as a nonlinear biasing mechanism. All these biasing elements with a negative rate have in common, that instabilities of the actuator system might occur. In order to prevent this usually undesired behavior, the nature of stability of negative rate biasing elements in combination with DEAs must be discussed.

In order to perform such investigations, a fictive biasing element is introduced, which is not represented by a direct physical correspondent. This biasing element has the properties of a linear spring with negative rate  $-k_{NLS}$ , and is called negative linear spring (NLS). The constitutive equation of this element is as follows

$$F_{NLS} = k_{NLS}(x - x_0^{NLS}). \quad (3.5)$$

The schematics of the system is shown in Figure 3.4 (a), with the non-physical element depicted as a green box. The force equilibrium of the system calculates to

$$F_{DE} = F_{NLS} = k_{NLS} (x - x_0^{NLS}). \quad (3.6)$$

The element stiffness equals  $-k_{NLS}$ , which means that  $k_{NLS}$  represents the absolute value. This representation is important for the following stability analysis in Section 3.1.3. The corresponding force-displacement plot in Figure 3.4 (b) shows the behavior of the biasing element. Due to its negative stiffness, the curve shape resembles the shape of DEA characteristics much better than a LBS, therefore the achievable stroke  $\Delta h_{NLS}$  is much larger, here approximately 3.7 mm. Note that this design is not optimized, therefore the achieved stroke is not optimal, but already three times as large as the optimized LBS system stroke. As mentioned before, the stability analysis of systems with negative stiffness is a crucial step. A first indication in Figure 3.4 (b) is the existence of further force equilibria, marked with black squares. The meaning of those equilibria is interpreted in Section 3.1.3.

### 3.1.2 Systematic Force Analysis

While the described design process for a LBS biased system offers a structured approach in designing an actuator system, there is a downside. A comparison of the actuator system against an external load based on the representation in Figure 3.1 (b) is not intuitive. To achieve a deeper understanding of the overall system behavior, an alternative representation for the system force analysis is introduced. To introduce this framework, we consider the actuator free-body diagram shown in Figure 3.5 (a). Note that only quasi-static forces are considered. In this case, also an external force  $F_{ext}$  is considered (solid magenta line), representing the external load acting on the actuator. The force equilibrium results into

$$F_{ext} = F_B - F_{DE}, \quad (3.7)$$

with  $F_B$  representing an arbitrary biasing force, in this case a linear spring. It is possible to define the overall actuator force  $F_A$  as

$$F_A = F_B - F_{DE}. \quad (3.8)$$

Therefore, by combining equation (3.7) and (3.8), we obtain the relationship

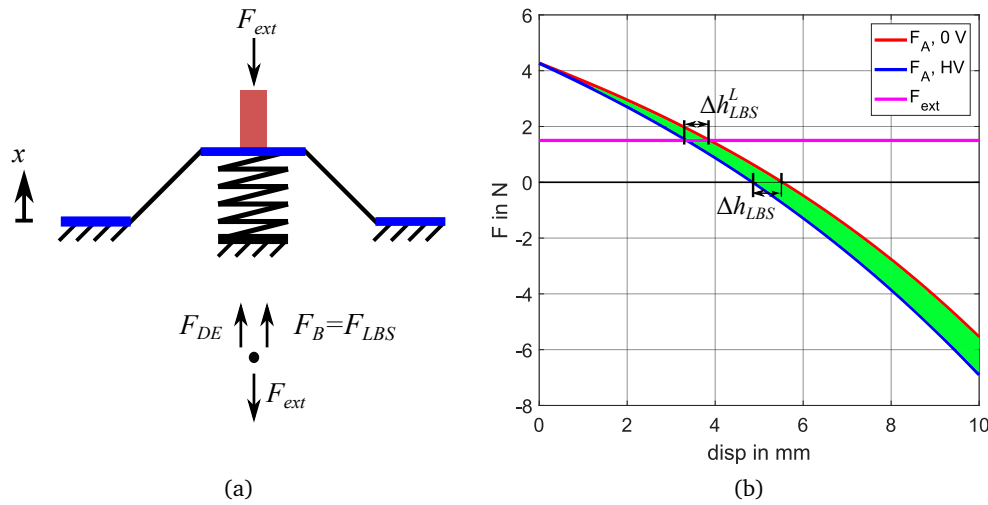


**Figure 3.5:** Actuator schematics with force equilibrium working against an external load (a), and the corresponding force vs. displacement diagram (b).

$$F_{ext} = F_A, \quad (3.9)$$

which implies that the external force is completely balanced by the actuator, i.e., these forces are equal at equilibrium. This condition is also illustrated in the force-displacement diagram shown in Figure 3.5 (b), in which  $F_{ext}$  and  $F_A$  intersect each other in correspondence of the resulting equilibrium points. The actuator force is calculated by considering the same LBS and DEA forces shown in Figure 3.1 (b). The main advantage of this representation is the possibility of directly estimating the overall actuator system performance when working against different types of external loads. Furthermore, the intersection points with the zero force axis describe the actuator system performance in case no external load is applied, i.e.,  $F_{ext} = F_A = 0$ . The resulting zero load stroke output  $\Delta h_{LBS}$  is highlighted in Figure 3.5 (b), and coincides with the stroke prediction according to the inner forces, as in Figure 3.1 (b). Additionally, the intersections between the actuator curves and an external force, here an exemplary constant load (Figure 3.5 (b), magenta line) provide an estimation of the stroke  $\Delta h_{LBS}^L$  when working against this load. As it can be observed from Figure 3.5 (b), the resulting stroke decreases, if the external load increases.

For comparing the optimal design of the LBS actuator to designs produced in this chapter, the actuator force diagram which belongs to Figure 3.3 is shown in Figure 3.6. The same stroke of  $\Delta h_{LBS} = 1.2$  mm is predicted, when no external load is applied. Furthermore, the maximal force  $F_{max}$  the actuator is able to work against equals approximately 9 N. At 9 N, no stroke is

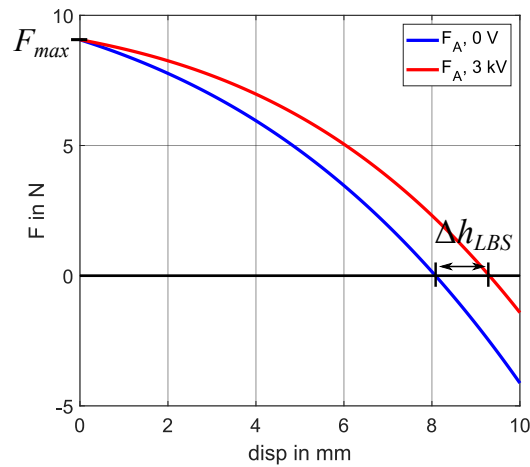


**Figure 3.6:** The actuator diagram of the optimal LBS design also yields 1.2 mm stroke.

produced, above that load, the actuator system produces a stroke in negative  $x$ -direction. For the fictive NLS biasing, the actuator force representation is depicted in Figure 3.7, (a) showing the schematics while (b) shows the force-displacement diagram. The achievable stroke  $\Delta h_{NLS}$  corresponds to the stroke in Figure 3.4 (b). One can see a clear difference between the two actuator diagrams in Figure 3.5 (b) and Figure 3.7 (b). While the diagram is monotonically decreasing for the LBS, for the NLS the slope changes from rising to falling. This fact is discussed in detail in the following section in relation to system stability. Furthermore, the ability to work against external loads is much smaller for the NLS system. While the optimal LBS system is able to produce a stroke against up to 9 N, the NLS system covers only around 0.1 N (maximum force value in Figure 3.7 (b)). For the displayed load case of 0.1 N, the produced stroke  $\Delta h_{NLS}^L$  decreases marginally. As shown by the previous examples, this systematic force analysis leads to a more intuitive understanding of the actuator performance when working against an external load. In this case, the analysis of inner forces does not allow a straightforward stroke computation. The work area inside the envelope between the actuator curves can be interpreted as an evaluation of the system actuation capability (highlighted in green in Figure 3.5 (b)). In fact, the larger this work area, the more the system is capable of handling various types of loads, in complete accordance to the work area for inner forces in Figure 2.7. As mentioned before, the use of a negative spring rate element demands a stability analysis, which is performed next.

### 3.1.3 Stability Analysis

In order to discuss the stability of an actuator system, an investigation of the system energy is adequate. In Newtonian mechanics, the relation between force  $F$  and energy  $\Psi$  of a system is defined as

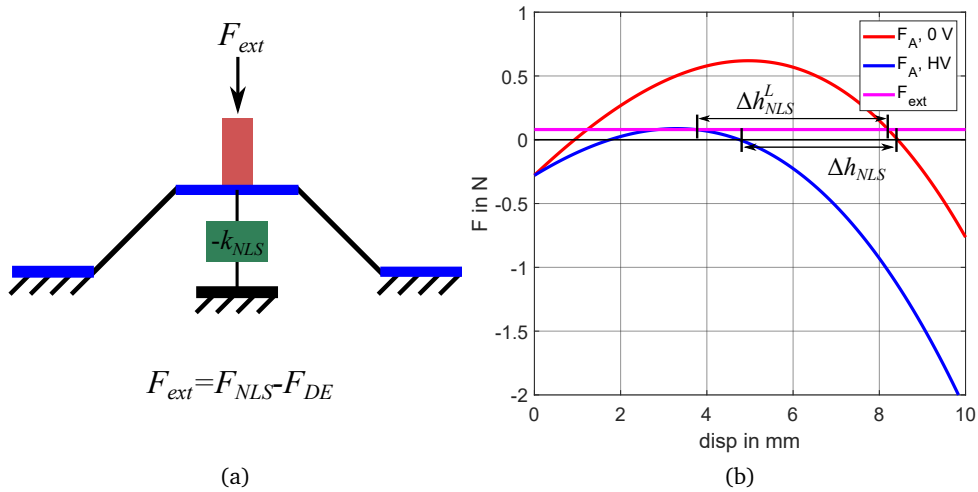


**Figure 3.7:** Actuator schematics with external load for NLS biasing (a) and corresponding force vs. displacement (b).

$$F = -\frac{d\Psi}{dx}. \quad (3.10)$$

A system is in an equilibrium, when the sum of all forces  $F$  equals zero,

$$\frac{d\Psi}{dx} = 0. \quad (3.11)$$

Additionally, the system must be able to maintain that equilibrium by itself. When for a small deflection  $\delta x$ , the resulting force increment  $\delta F$  onto the system counteracts this deflection, the system restores back to its original equilibrium state. Following this description, for the force increment  $\delta F$  applies

$$\delta F = \frac{dF}{dx} \delta x + \mathcal{O}(x^2) \approx \frac{dF}{dx} \delta x, \quad (3.12)$$

yielding the stability condition

$$\frac{dF}{dx} < 0. \quad (3.13)$$

Combining equation (3.10) and (3.13) leads to

$$-\frac{d^2\Psi}{dx^2} < 0, \quad (3.14)$$

respectively

$$\frac{d^2\Psi}{dx^2} > 0. \quad (3.15)$$

Concluding from equation (3.11) and (3.15), it is evident that the energy  $\Psi$  must obtain a minimum in order to achieve a stable state. For a LBS, the energy calculates to

$$\Psi_{LBS} = - \int F_{LBS} dx = \int k_L x dx = \frac{1}{2} k_L x^2, \quad (3.16)$$

whereas for a NLS, it calculates to

$$\Psi_{NLS} = - \int F_{NLS} dx = - \int k_{NLS} x dx = -\frac{1}{2} k_{NLS} x^2. \quad (3.17)$$

A comparison of the element forces and energies is shown in Figure 3.8. Whereas the energy of the LBS (Figure 3.8 (b), green line) is convex and therefore always stable with one minimum, the energy of the NLS system (Figure 3.8 (b), gray line) is intrinsically unstable. The interpretation of the unstable behavior of the NLS system is explained with following thought experiment. Due to the negative linear stiffness defined in equation (3.5) as a restoring force, a deflection does not lead to a counteract back to the stable state. In the absence of a counteracting force, the deflection increases further, thus, the system behaves unstable. Combining the energies of DEA and LBS, as shown in Figure 3.9 ((a) shows the individual energies, whereas (b) shows the superposition) yields an important conclusion. Due to its convex shape, there is

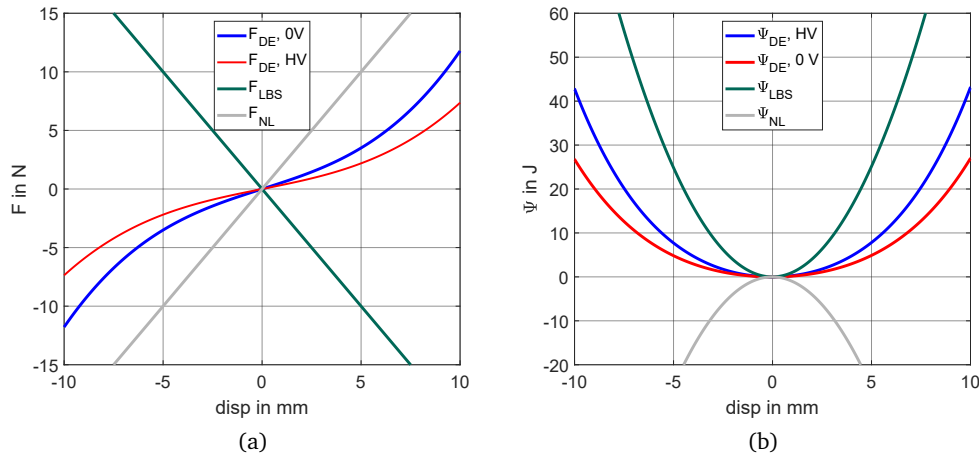


**Figure 3.8:** Force equilibrium for DEA, LBS and NLS in the DEA coordinate system (a) and corresponding energies (b).

always on stable equilibrium for 0 V and for HV. These stable equilibria are marked with a black circle. This is in accordance with the physical understanding of this system's stability. Note, that the shift of the LBS energy is due to its pre-compression when used inside the actuator system.

For the NLS system, the behavior is different. Examining the combined energy in Figure 3.10 ((a) shows the individual energies, whereas (b) shows the superposition), there is a concave and a convex area. This change in curvature leads to stable and unstable equilibria, as already stated in Figure 3.4 (b). The black squares mark the unstable maxima of the energy, which only fulfill condition (3.11), while the black circles mark the stable energy minima, which fulfill condition (3.11) and (3.15). In conclusion, stable equilibria need to be in the convex area of the energy. These energy considerations give an understanding of the system behavior, marking the important difference for elements with negative stiffness. The DEA without any biasing behaves mechanically stable, with the ambition to maintain in the equilibrium position without any deflection (see DEA energy in Figure 3.8 (b)). Only a combination with an element with negative stiffness influences the system stability. Note that just like for the LBS, the NLS energy shifts due to the pre-compression  $x_0^{NLS}$ .

In order to proceed stability analysis for nonlinear systems, considering the energy is not the only way to go. Based on equation (3.13), the force combination of the actuator diagram also yields the stability of all force equilibria. Equilibria with negative slope are stable,

$$\frac{dF_A(x, V)}{dx} < 0, \quad (3.18)$$

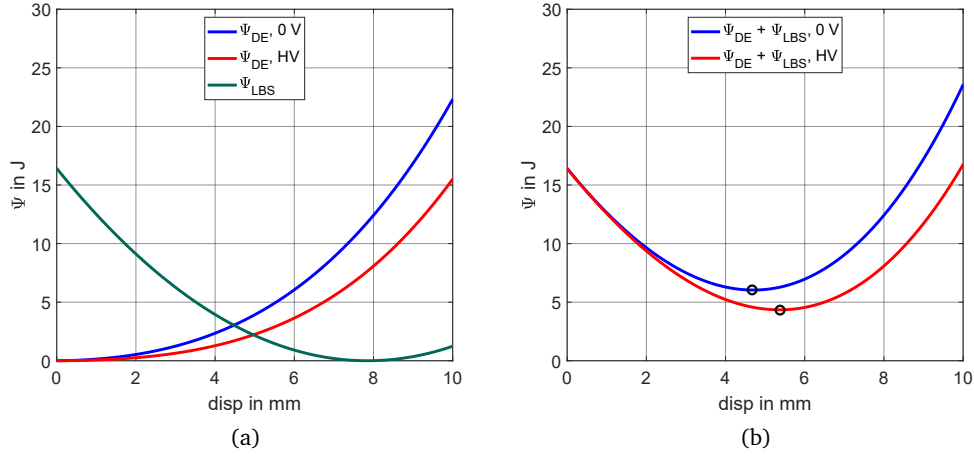


**Figure 3.9:** The energies of DEA and LBS (a), their combination generates two stable energy minima (black circles) for 0V and HV (b).

whereas equilibria with positive slope are unstable,

$$\frac{dF_A(x, V)}{dx} > 0. \quad (3.19)$$

This observation is determined by a comparison of Figure 3.7 (b) and Figure 3.10 (b). Both figures represent the same actuator system. The equilibria with positive slope in Figure 3.7 (b) correspond to the energy maxima in Figure 3.10 (b) and vice versa for stable equilibria and energy minima. This result can be translated further to the inner force diagram, as shown in Figure 3.4 (b). Combining equation (3.8) and (3.13), the stability criterion transforms to

$$\frac{dF_{DE}(x, V)}{dx} > \frac{dF_B(x)}{dx}. \quad (3.20)$$

This representation also offers a physical interpretation. The slope of the inner forces equals their stiffness. When the system is deflected by  $\delta x$  out of an equilibrium point and the stiffness of the DEA exceeds the biasing element stiffness, the DEA is pulling the system back into an equilibrium, and thus it is stable. If the biasing element's stiffness is larger than the DEA stiffness, the biasing element pulls the system out of the equilibrium, thus is unstable. A critical point is defined, where the stability of an equilibrium changes as

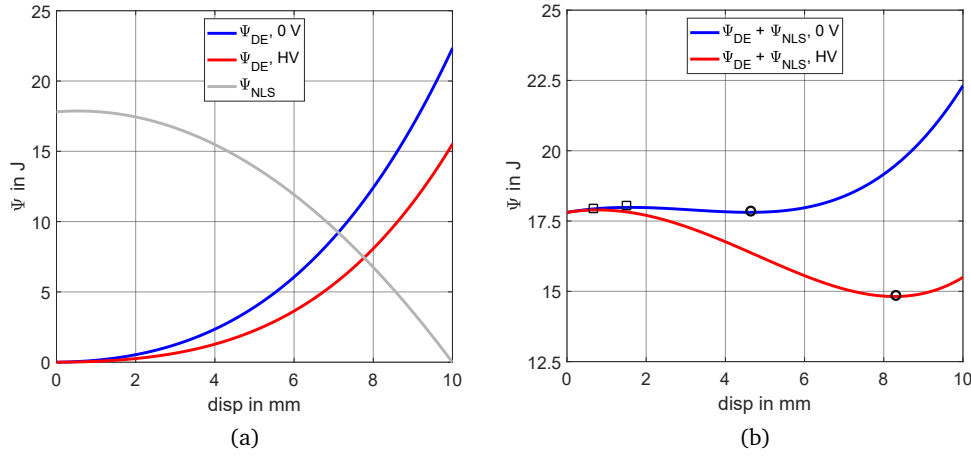


**Figure 3.10:** The energies of DEA and NLS (a), their combination generates unstable energy maxima (rectangles) and stable energy minima (circles) (b).

$$x_{cr} = x_{cr}(V) = \left\{ x \left| \frac{dF_{DE}(x, V)}{dx} = \frac{dF_B(x)}{dx} \right. \right\} = \left\{ x \left| \frac{dF_A(x, V)}{dx} = 0 \right. \right\}. \quad (3.21)$$

Note that this point is not fixed for an actuator system, since the stiffness of the DEA decreases with voltage application. This result is harnessed in Section 3.2 in order to design stable and unstable areas of the actuator diagram, as well as in Section 3.2.3 in order to improve the actuator performance.

### 3.1.4 Biasing with Nonlinear Elements

The in the prior sections discussed fictive biasing element with negative stiffness does not offer a physical correspondent. However, there are different nonlinear elements which exhibit negative stiffness in a particular range. Such elements are discussed in literature, e.g., NBSs [11, 53, 79], joint mechanisms [76, 80] or attracting permanent magnets [15, 81, 82]. For example, the inner forces and actuator force for a NBS biased system is shown in Figure 3.11. In the area of negative stiffness, the qualitative behavior of the NLS element is clearly visible. However, at the ends, where the NBS characteristic has positive stiffness, the behavior differs from the NLS biasing element. The derived rules for stability analysis in the actuator diagram can be applied to the NBS actuator diagram in Figure 3.11 (b). Based on equation (3.18) and (3.19), the actuator diagram yields stable equilibria without an applied load, whereas a load application of 0.2 N (Figure 3.11 (b), magenta line) produces additional unstable equilibria (black rectangle in Figure 3.11 (b)). In this case, the stable equilibria are shifted to the smaller

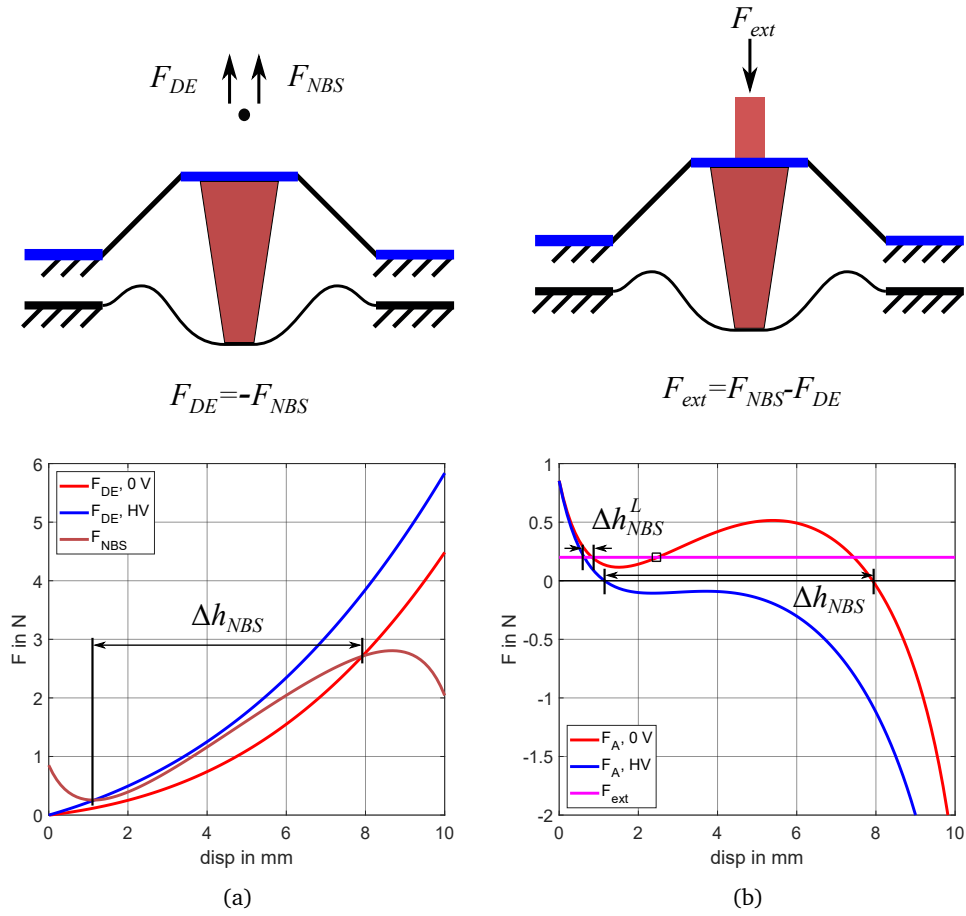


**Figure 3.11:** A NBS as nonlinear biasing element, inner force equilibrium (a) and actuator force representation (b).

deformation area and produce a significantly smaller stroke  $\Delta h_{NBS}^L$ , as shown in Figure 3.11 (b). Note that the presented qualitative curves in Figure 3.11 are for an inclined NBS. If the NBS is not inclined, a combination of NBS and LBS is necessary in order to produce the depicted actuator diagram. See [83] for further details concerning inclined NBS. For every nonlinear element which offers a negative stiffness area, stability must be examined. For NBS systems, system stability and suitable control algorithms have been discussed by Rizzello *et al.* [84].

In Summary, a systematic analysis for linear and nonlinear biasing elements has been discussed in this section, including a stability analysis. The nonlinear biasing mechanism used for the advanced design methods in the subsequent section is based on PM, followed by a combination of PM and LBS for system improvement.

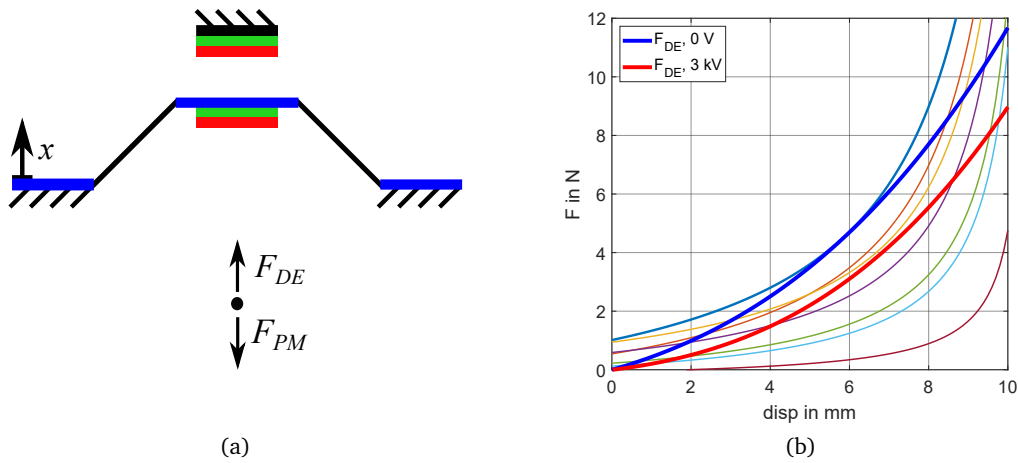


**Figure 3.12:** A sketch of a PM biased DEA system with free-body diagram (a), and different commercially available permanent magnet characteristics in comparison to DEA curves (b).

## 3.2 Biasing with Permanent Magnets

Attracting PM are a comparably new biasing mechanism for DEA systems. First systems have been described in [14, 15], as well as in [81, 82]. For a system based on COP DEAs, schematics are shown in Figure 3.12 (a). The magnets attract each other and work against the DEA force. The advantage of PM is the shape of their force-displacement characteristic, which can be approximated with the function  $x^{-n}$  ( $n$  varying for different magnet types, e.g., [85] states  $n = 6$  for cylindrical permanent magnets), which is shown for different commercially available magnet types in Figure 3.12 (b) and resembles the shape of the DEA curves. Different magnets from *K&J Magnetics* [86] have been examined in order to find a suitable magnet type for the here used COP DEAs (see Figure 3.12 (b)). To obtain a large stroke, the biasing system needs to be properly designed in order to achieve optimal intersections between DEA and PM curves. Applying the stability considerations performed in Section 3.1.2, the actuator diagram of a PM biased system can be divided in three parts. For the actuator diagram, stable and unstable regions have been defined in equation (3.18) and (3.19).

Figure 3.13 (a) shows the inner force diagram of PM and DEA, while Figure 3.13 (b) shows the equivalent actuator force diagram. Both depict different areas where the system behaves stable (green), where the system behaves unstable (red) and a further region, here called the critical region (yellow). Due to the change in stiffness of the DEA during actuation, the critical point shifts according to the applied voltage  $V$ . This change in stiffness is reflected in the critical region, where the stability is dependent on the applied voltage. To obtain an overall stable system, condition (3.20) must hold for the smallest stiffness of the DEA, which is obtained for the maximum applicable voltage  $V_{max}$ , yielding

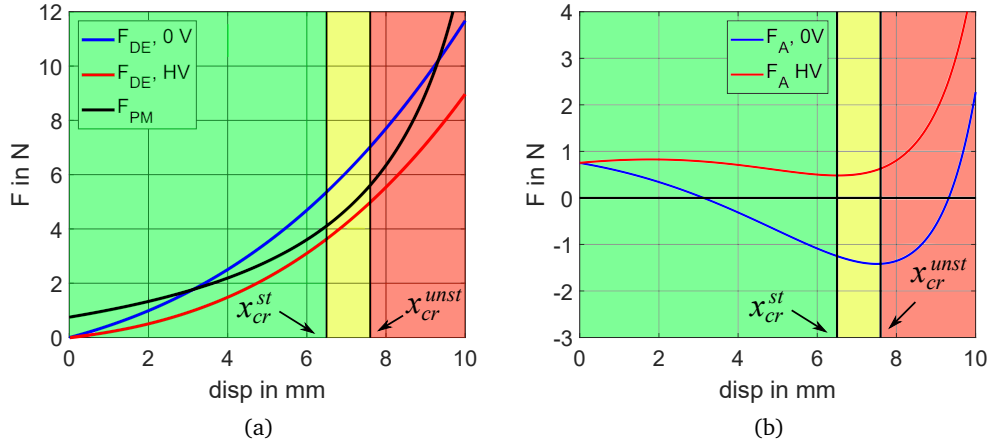


**Figure 3.13:** Different stability areas for arbitrary magnet curve: stable (green), critical (yellow) and unstable (red). Inner forces (a) and actuator force (b).

$$x_{cr}^{st} = \left\{ x \left| \frac{dF_{DE}(x, V_{max})}{dx} = \frac{dF_{PM}(x)}{dx} \right. \right\} = \left\{ x \left| \frac{dF_A(x, V_{max})}{dx} = 0 \right. \right\}. \quad (3.22)$$

The condition

$$x_{cr}^{unst} = \left\{ x \left| \frac{dF_{DE}(x, 0V)}{dx} = \frac{dF_{PM}(x)}{dx} \right. \right\} = \left\{ x \left| \frac{dF_A(x, 0V)}{dx} = 0 \right. \right\} \quad (3.23)$$

yields the point  $x_{cr}^{unst}$  from where on the system shows unstable behavior. In between, the system shows unstable behavior, but regains its stability at 0V. The physical interpretation of the unstable area of a PM biased system is as follows. When the critical point  $x_{cr}^{st}$  is exceeded, the PM stiffness exceeds the DEA stiffness, and therefore dominates the system. In this moment, the system tends to collapse, which means that the magnets attract each other to the point of contact. The actuator is then caught in this state and can only be pulled back into its original state by an additional external force. However, when a hard stop, positioned at  $x_{cr}^{unst}$ , prevents the system from moving further into the unstable area, the system is able to return to its original state when the voltage is removed, due to the DEA stiffness exceeding the PM stiffness in any case. For PM biased actuators in this section, a hard stop is always used in order to limit the area of operation. For stable actuators, the hard stop is placed at  $x_{cr}^{st}$ , so that instabilities are prohibited. When the actuator is allowed to reach the critical area, the hard stop is placed at  $x_{cr}^{unst}$ . When the actuator transfers to the critical area, the magnets snap to

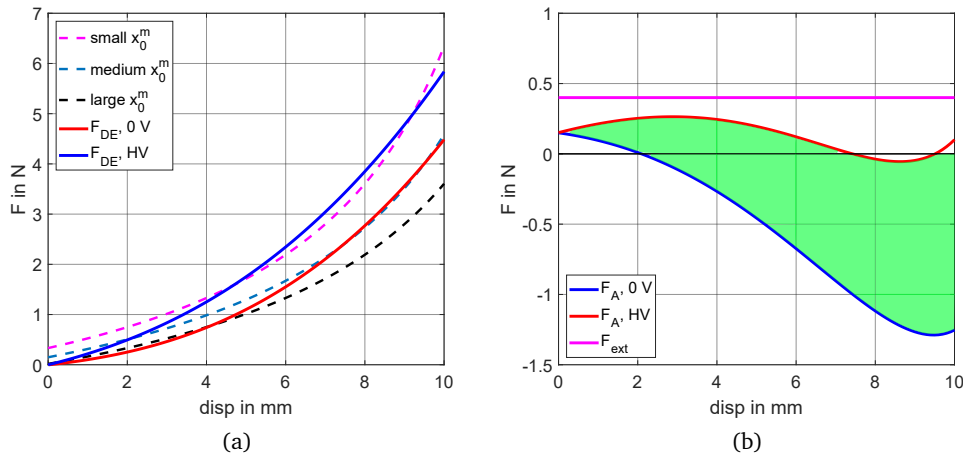


**Figure 3.14:** Varying the initial magnet displacement changes the actuator performance (a), and actuator curves corresponding to medium initial displacement (b).

the hardstop. When the voltage is decreased, the DEA is eventually stiffer than the PM and pulls the system back in its original state.

In this section, first a stable system is designed, which bases on PM as biasing mechanism only. Subsequently, a stable combination of LBS and PM is proposed, in order to eliminate disadvantages of a PM system and improve the overall system performance. A system based on PM only, which acts in the stable as well as the critical range, is finally proposed in order to further increase the actuator performance.

### 3.2.1 Design of Stable Systems with Biasing Magnets

For a PM biased system, there are two main design parameters, namely the type of PM and the initial magnet displacement  $x_0^m$ . Although all investigated magnet types show qualitatively similar behavior (see Figure 3.12 (b)), each curve exhibits different slope and force levels. The choice of the PM type must be performed in order to match the characteristics of the DEA as close as possible. The initial magnet displacement  $x_0^m$  corresponds to the distance between the DEA and the PM system. By increasing this value, the PM characteristic curve shifts to the right with respect to the DEA coordinate system, as shown in Figure 3.14 (a). A larger initial displacement leads to smaller stroke (see Figure 3.14 (a), black dashed line). For a smaller initial displacement, the stroke increases due to the larger force and slope exhibited by the PM curve. In case the shift to the left of the PM curve is excessively large, no intersection with the HV DEA curve exists. At this point, beforementioned stability issues arise. This fact makes the PM biased system sensitive for parameter changes, e.g., a small change of the initial magnet displacement might influence the stroke drastically. In summary, the initial magnet

displacement must be chosen in order to ensure an intersection with the HV curve, such that the actuator stroke is maximized (see Figure 3.12 (a), cyan dashed line). The systematic force analysis of the PM biased system, namely the design with medium  $x_0^m$  (Figure 3.12 (a), cyan line), is shown in Figure 3.14 (b). First, note that the force scale is smaller in comparison to the diagram in Figure 3.5 (b) for the LBS system. Therefore, despite the PM biased system yielding a much larger stroke in comparison to a LBS, the external forces that can be handled are significantly lower. As an example, note that the 0.4 N external load shown in Figure 3.14 (b) (magenta line) cannot be applied to the system. This is due to the lack of intersections in the actuator force diagram. In conclusion, there is no possibility for the PM biased actuator of increasing the force level as in the LBS case, where the spring pre-compression is able to compensate known external loads. The advantages of the PM biased system are then rapidly lost in case of an external force applied.

For the practical design of the system biased with PM, two magnets of type R 624 from *K&J Magnetics* are chosen. This choice is motivated by the compatibility of the R 624 magnets with the characteristics of the 8-layer DEA. As previously discussed, the actuator stroke increases with a smaller initial magnet displacement  $x_0^m$ . If this value is not chosen properly, however, stability issues may arise. In order to correctly operate in open loop, the initial magnet displacement is decreased until the PM curve just touches the 3 kV DEA curve. To improve robustness with respect to the neglected material hysteresis, an additional shift of 0.1 mm is also included. The resulting design is shown in Figure 3.15, for inner forces (a) and the overall actuator force (b). The optimal value for the initial magnet displacement  $x_0^m$  results to 8.8 mm and leads to a theoretical stroke  $\Delta h_{PM}^{st}$  of 3.9 mm. Compared to the LBS DEA system in Figure 3.3, which states a stroke of 1.2 mm, the PM permits to achieve an increase in stroke of a factor higher than 3. Additionally, the DEA equilibrium for zero volt is lower for the PM system, leading to smaller stretch of the DEA and therefore to a possibly longer lifetime. In order to keep the actuator from reaching the critical area, an additional hard stop is placed at the in equation (3.22) stated  $x_{cr}^{st} = 6.7$  mm. Note that, for both actuator diagrams in Figure 3.5 (a) (LBS) and Figure 3.15 (b) (PM), the slope of the 0 V curve is always larger in magnitude than the 3 kV one. As a result, the achieved actuator stroke decreases with increasing external load. It can then be concluded that the maximal stroke is always achieved for the zero load case. As discussed in Section 3.1.2, the LBS system is able to generate actuation against external loads up to 9 N. The PM biased system is not able to perform a stroke for external loads larger than 0.6 N, i.e., 15 times smaller than the LBS one. This shows a clear downside of the PM biasing. In order to resolve especially this issue, a combination of LBS and PM biasing is introduced in the next section. This combination offers the possibility of a PM biased system to be adapted to arbitrary load scenarios.

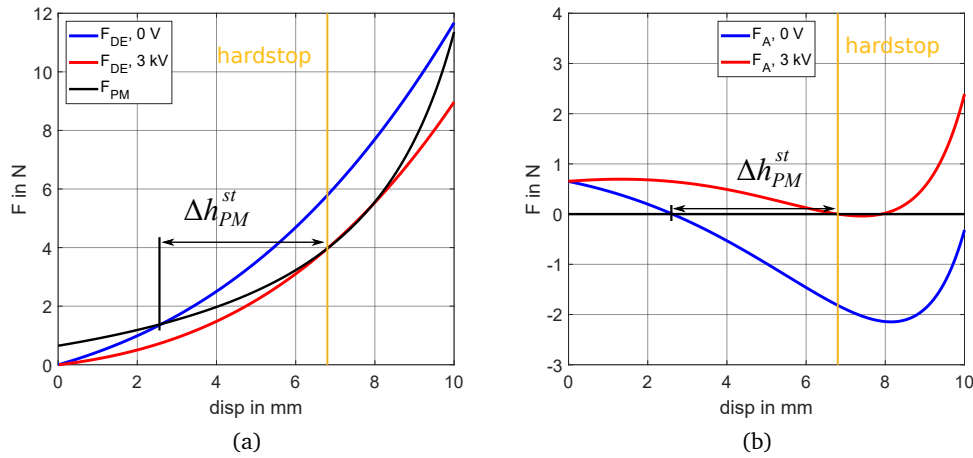


Figure 3.15: Optimal design for PM biased system, inner forces (a) and actuator force (b).

### 3.2.2 Design of Stable Systems with Combined Biasing Elements

The biasing solution based on PM shows a remarkable improvement in stroke with respect to LBS DEA systems, as the previous section states. However, the PM biased DEA exhibits a drawback concerning the maximum applicable external load. In fact, while a LBS biased system can be adapted to a desired load through an increase or decrease in spring compression, the same does not hold for PM biased systems. The only design parameter for a chosen magnet type is the initial magnet displacement  $x_0^m$ , which on the one hand yields a straight forward optimal design process, but on the other hand does not allow any adaption to external loads. In addition, if the external load force changes, the stroke of the PM biased actuator decreases drastically. In order to overcome these issues, a combination of both LBS and PM as a biasing mechanism is introduced in this section as an advanced biasing concept. This combined system has three design parameters, namely  $x_0^m$ ,  $x_0^s$  and  $k_L$ . The force equilibrium for this actuator system yields the new equation

$$F_{ext} = F_A = F_{LBS} + F_{PM} - F_{DE}. \quad (3.24)$$

A schematic of the combined biasing system consisting of LBS, PM and DEA is depicted in Figure 3.16. The combination of both elements is mechanically realizable by putting the magnet underneath the DEA in contact with the LBS. An increase from one design parameter for the PM system to three design parameters for the LBS system offers the possibility to adapt the system to different load scenarios. However, the straight forward nature of the design process changes due to interference of all three parameters. Changing one parameter also influences

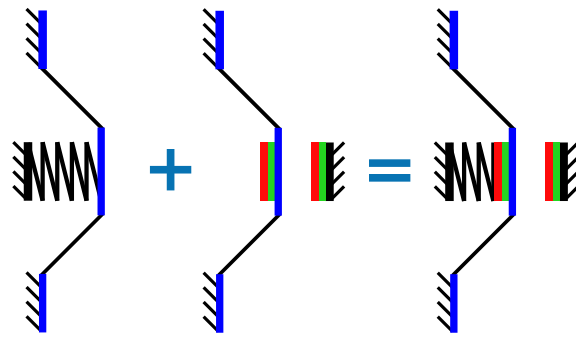


**Figure 3.16:** A combined biasing mechanism consisting of LBS and PM for performance improvement.

the effect of the other parameters. To understand the combined effect of all design parameters on the resulting actuator performance, a sensitivity analysis is performed first. To this end, one parameter is varied while the other two are fixed. This procedure permits to identify trends for each parameter in order to develop an optimal design procedure for a given external load. Since the effects of the load have to be explicitly taken into account, a force analysis based on the actuator representation is preferred. The goal of the design is the maximization of the envelope between the actuator curves, i.e., the work area of the system (see Figure 3.14 (b), green area). Every external load that fits into this work area can be coped with the resulting actuator. As an additional requirement, the system must be able to work properly even without an external load. This condition implies that the system must exhibit two intersections with the zero load axis in the actuator diagram, one for 0V and one for 3 kV. Without these equilibria the actuator system does not work in the allowed area, as described before, and it may eventually get stuck in a state in which actuation is no longer possible due to instability.

Before showing results of the sensitivity analysis, the influence of the design parameters onto the qualitative behavior of the actuator diagram is discussed. Two effects can be observed in the actuator diagram while changing parameters, i.e., a variation in curve slope, which results in a change in horizontal gap between the actuator curves, and a change in the force level. An increase of the horizontal gap between the actuator curves leads to a larger work area and to a larger actuator stroke, e.g., upper right to upper center diagram in Figure 3.17, while a decrease in this quantity leads to a reduction in both work area and stroke. If the force level increases, the range of loads that the actuator is capable to handle increases (see Figure 3.17, upper left to upper center diagram), while a decrease in force also decreases this quantity. An optimal design requires a high force level together with a large horizontal gap between the actuator curves. However, a tradeoff has to be found in practical system design, since an increase in force level always leads to a decrease of the horizontal gap and vice versa. The main objective is the maximization of the envelope between the two curves, by finding the best tradeoff between force level and horizontal gap with respect to the applied load. In other words, the force level must be raised at least up to the desired external load, in

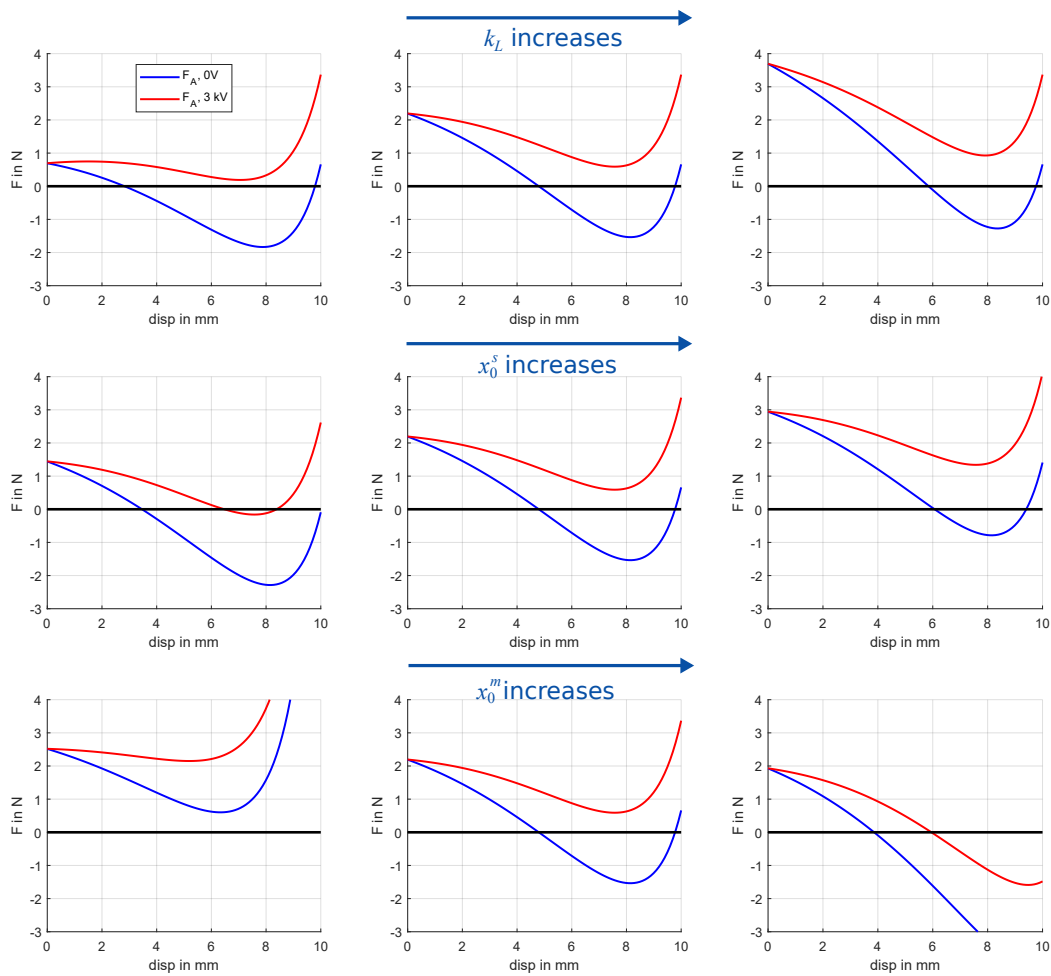


**Figure 3.17:** Variation of design parameters (from left to right): increasing spring stiffness (upper row), increasing spring pre-compression (center row), increasing initial magnet displacement (lower row).

order to produce equilibria between this load and the actuator curves. At the same time, the intersections with the zero force axis must be ensured. Figure 3.17 shows a set of parameter variations. Nominal values are reported in the center column. The parameters are varied by decreasing (left column) and increasing (right column) their nominal values. Through this variation, the sensitivity of the actuator curves based with respect to such parameters can be analyzed. The upper row displays the effect of an increase in spring stiffness  $k_L$ . The actuator curves tilt due to the tilting of the LBS curve. A lower stiffness leads to a larger horizontal gap between the curves, which is suited to obtain a large stroke for small loads. A larger stiffness leads to a smaller horizontal gap but, at the same time, the force level increases. A larger load can therefore be handled with a larger  $k_L$ , but the smaller horizontal gap also leads to a smaller actuation stroke. A variation of the LBS pre-compression  $x_0^s$  is shown in the center row of Figure 3.17. The pre-compression is directly reflected into a force offset, as shown in Figure 3.17 (b). The existence of an equilibrium for the 3 kV DEA curve can be ensured

by shifting the actuator curves, ensuring that both of them intersect the zero load axis. This tuning is essential to ensure that the system works correctly without an external load. The effects of varying the third parameter, i.e.,  $x_0^m$ , are shown in the lower row. A decrease of the initial magnet displacement increases the horizontal gap, leading to a larger actuator stroke. Then again, an increase in  $x_0^m$  rises the force level, but decreases the horizontal gap, which reduces the actuator stroke. The outcome of the parametric study can be summarized into the following design procedure:

1. Start with a  $3 \times 3$  matrix as shown in Figure 3.17, representing the relevant parameter space. Therefore, vary each parameter in such a way that the described trends are clearly visible.
2. Use the values corresponding to the most satisfactory set of parameters as initial design. If needed, modify the initial magnet displacement so that both curves touch the zero force line.
3. Modify the LBS stiffness  $k_L$  so that the required force level is exceeded
4. Adjust the spring compression to shift the curves back to a possible actuation with zero load (both curves touch the zero force line).

Steps 3 and 4 are interdependent: a change in spring compression also shifts the force level. To achieve an optimal design, these steps have to be iterated until both conditions are satisfied. Note also that the complete design turns out to be an iterative process. Due to the simultaneous dependency of performance on all design parameters, it is not expected that the optimal design is achieved in just one iteration.

In order to obtain a large stroke and ability to cope with larger external loads simultaneously, a practical design solution based on the combination of LBS and PM biasing is proposed. The system design is carried out by means of the derived design procedure. Similar to all other actuator designs in this chapter, 8 DEA layers and attracting magnets of type R 624 will be considered for the design. The performance specification is given in terms of a maximal possible stroke for 1.5 N constant load, as well as the ability to perform a stroke even without an external load. All steps described in the design procedure are reported in detail in the following paragraph. For every step, Figure 3.18 shows the corresponding result. For demonstration purposes, only the first iteration of the procedure is shown, while a total number of 3 iterations has been performed to achieve the final design. The last two iterations yield a theoretical stroke improvement of less than 5 % compared to the first one. Therefore, discussion of the first iteration only is sufficient for demonstration purposes.

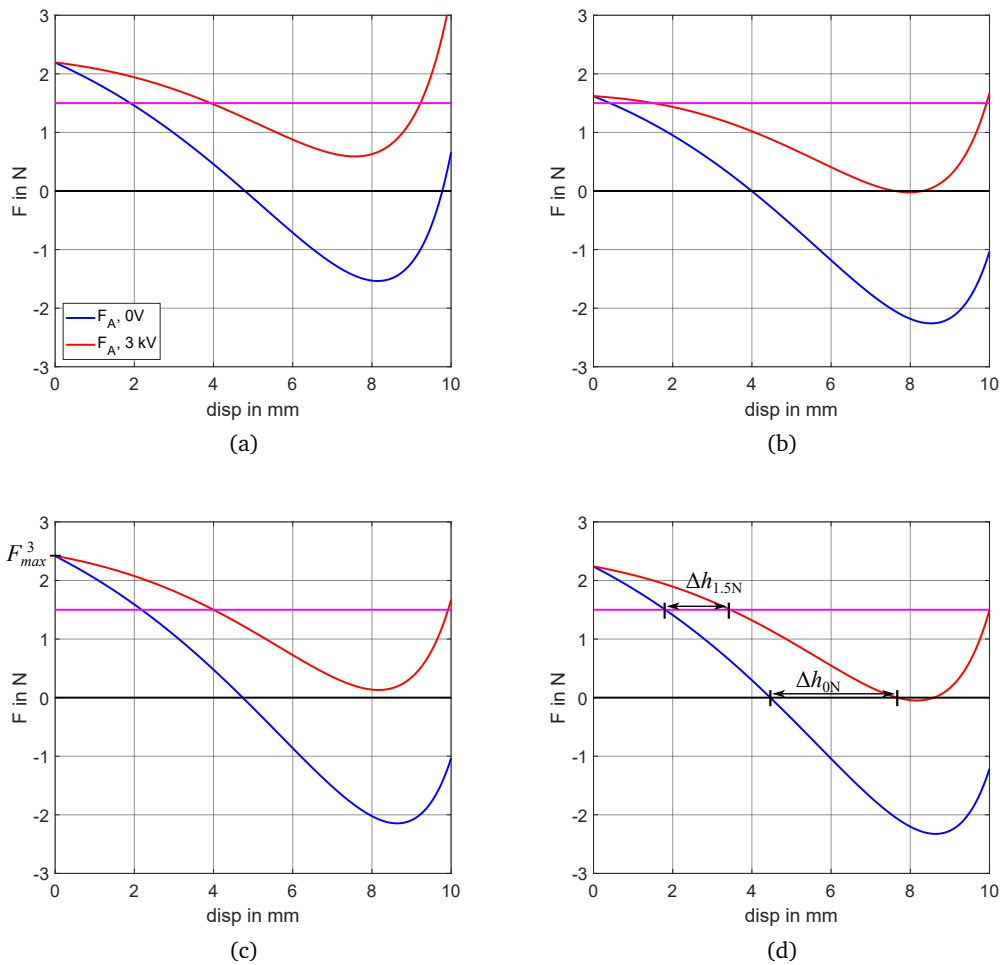


**Figure 3.18:** All 4 design steps to maximize the actuator stroke for the given load case of 1.5 N constant force (a)-(c), and final design (d).

1. For the first step, an initial set of parameter values is chosen. For the given case of study, the corresponding  $3 \times 3$  matrix is shown in Figure 3.17. The middle-left configuration shows the most promising characteristics and is reported in Figure 3.18 (a). The parameters corresponding to this configuration are chosen as initial conditions, and are given as follows:  $k_L = 0.1 \text{ N/mm}$ ,  $x_0^s = 10 \text{ mm}$ ,  $x_0^m = 9 \text{ mm}$ .
2. Following the instructions of step 2, the initial magnet displacement is increased so that both curves touch the zero force line. This is obtained by modifying  $x_0^m$  from 9 mm to 9.4 mm. The resulting actuator diagram is shown in Figure 3.18 (b) and yields a stroke of 1.0 mm for 1.5 N load, and of 3.5 mm at zero load.
3. To maximize the stroke for 1.5 N constant load, the force level needs to be increased. The aforementioned iteration of steps 3 and 4 is skipped by directly increasing the force

level up to  $F_{max}^3 = 2.4 \text{ N}$ , as shown in Figure 3.18 (c). Therefore, the spring stiffness  $k_L$  is increased from  $0.1 \text{ N/mm}$  to  $0.18 \text{ N/mm}$ . The resulting actuator diagram is shown in Figure 3.18 (c), and yields a stroke of  $1.8 \text{ mm}$  for  $1.5 \text{ N}$  load. Note that for zero load no proper actuation is possible. This issue is fixed in the next step.

4. To regain proper actuation stroke at zero load, the spring pre-compression is reduced until the equilibria with the zero force line are recovered. To achieve this goal, the pre-compression  $x_0^s$  is changed from  $10 \text{ mm}$  to  $9 \text{ mm}$ . Note that, similarly to the design in Section 3.2, the spring stiffness is further decreased to compensate the neglected hysteresis. The final optimized actuator diagram is shown in Figure 3.18 (d). It yields a stroke of  $1.7 \text{ mm}$  for  $1.5 \text{ N}$  load, and  $3.2 \text{ mm}$  at zero load. Finally, the optimized parameter set is reported:  $k_L = 0.18 \text{ N/mm}$ ,  $x_0^s = 9 \text{ mm}$ ,  $x_0^m = 9.4 \text{ mm}$ .

Compared to the design based on PM biasing only, a decrease in actuator stroke for zero load can be observed, i.e., from  $3.9 \text{ mm}$  to  $3.2 \text{ mm}$ . For the  $1.5 \text{ N}$  load case, however, the stroke improvement is remarkable. In fact, while the design without LBS cannot be actuated with a load of  $1.5 \text{ N}$ , the optimized design with combined LBS and PM is able to produce a stroke up to a load of  $2.6 \text{ N}$ . The corresponding stroke for a load of  $1.5 \text{ N}$  equals  $\Delta h_{1.5\text{N}} = 1.7 \text{ mm}$ .

### 3.2.3 Performance Improvement for Unstable Actuator Systems

The stroke resulting from the stable design in Section 3.2.1 can be improved by exploiting the unstable behavior of the PM biasing. For comparison, an actuator is designed with PM biasing, without an additional LBS. The design process with PM and LBS is basically the same, the phenomenological change due to harnessing the critical area in Figure 3.13 can be performed equally. For this design, a new operating point for the system is chosen where the high voltage equilibrium point vanishes by reducing the magnet distance  $x_0^m$ . The system reaches its critical point when the deformation is larger than  $x_{cr}^{st}$  defined in equation (3.22), and from here on the system is unstable. To avoid that the system collapses completely into the unstable area (Figure 3.13, red area), the hard stop is repositioned at  $x_{cr}^{unst}$  as defined by equation (3.23). This procedure creates an artificial equilibrium between PM and hard stop. As long as the instability condition (3.19) holds, the system stays in the artificial equilibrium. When the voltage decreases, the DEA stiffness exceeds the PM stiffness eventually. Then, the DEA is able to pull the system back into its original state. This design procedure results in an increase of stroke because not only the stable, but also the critical area is exploited. In exchange, proportionality vanishes. When the critical area is reached, the actuator snaps onto the hard stop, therefore, it is impossible to control positions in the critical area in open loop. To ensure proportionality in this area, a stabilizing position control system has to be designed [87]. For the actual design, the initial magnet displacement is chosen to  $x_0^m = 8.4 \text{ mm}$ , so that system

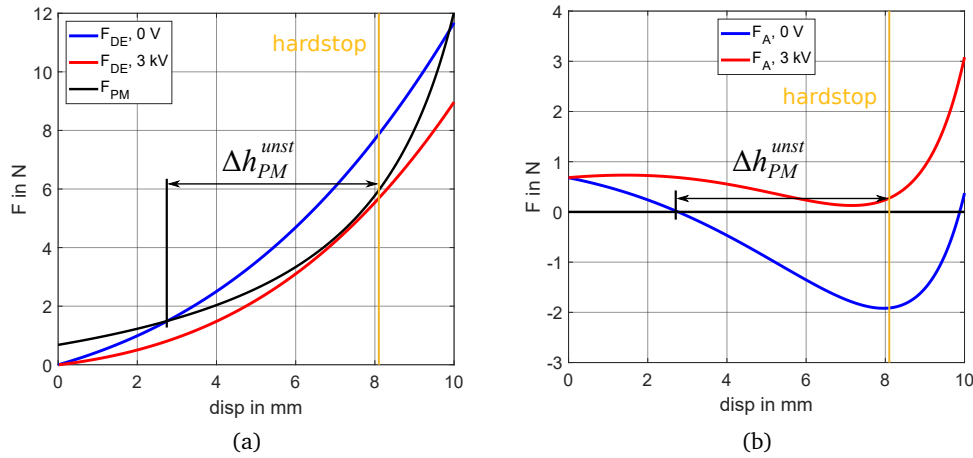


**Figure 3.19:** Design for unstable system in order to increase the actuator stroke, inner forces (a) and actuator force (b).

instability occurs and the critical area is maximized. The hard stop position  $x_{cr}^{unst}$  is chosen to 8.1 mm. Figure 3.19 shows the design curves, for inner forces (a) and for the actuator representation (b). A maximal stroke  $\Delta h_{PM}^{unst} = 5.3$  mm is obtained. With the stable design yielding a stroke of  $\Delta h_{PM}^{st} = 3.9$  mm, we obtain a relative stroke increase of 1.4 mm. The results of all designs are summarized in Table 2 for better comparison. The stroke without an external load, the stroke with an external load of 1.5 N and the maximal external force the actuator is able to work against are compared. In conclusion, the LBS+PM biased actuator shows the most versatility.

biasing mechanism	max. stroke at 0 N	max. stroke at 1.5 N	max. external force
LBS	1.2 mm	1.1 mm	9 N
PM (stable)	3.9 mm	none	0.6 N
PM (unstable)	5.3 mm	none	0.8 N
LBS + PM	3.2 mm	1.7 mm	2.6 N

**Table 2:** Results of the design section for all biasing systems.

### 3.2.4 Experimental Validation and Discussion of Results

In order to perform an experimental validation of all design methodologies, three demonstrators are designed in Solidworks 2016 (see Figure 3.20), based on LBS, PM and combined LBS+PM biasing, respectively. Note that the PM demonstrator is utilized to perform experiments for the stable as well as the unstable PM system, simply by adjusting the initial magnet displacement via a set screw and the use of an adapted hard stop. A HV sinusoidal signal is generated by a TREK Model 610E voltage amplifier and used to actuate the DEAs, while a Keyence LK-G87 laser displacement sensor measures the resulting stroke. The setup is con-

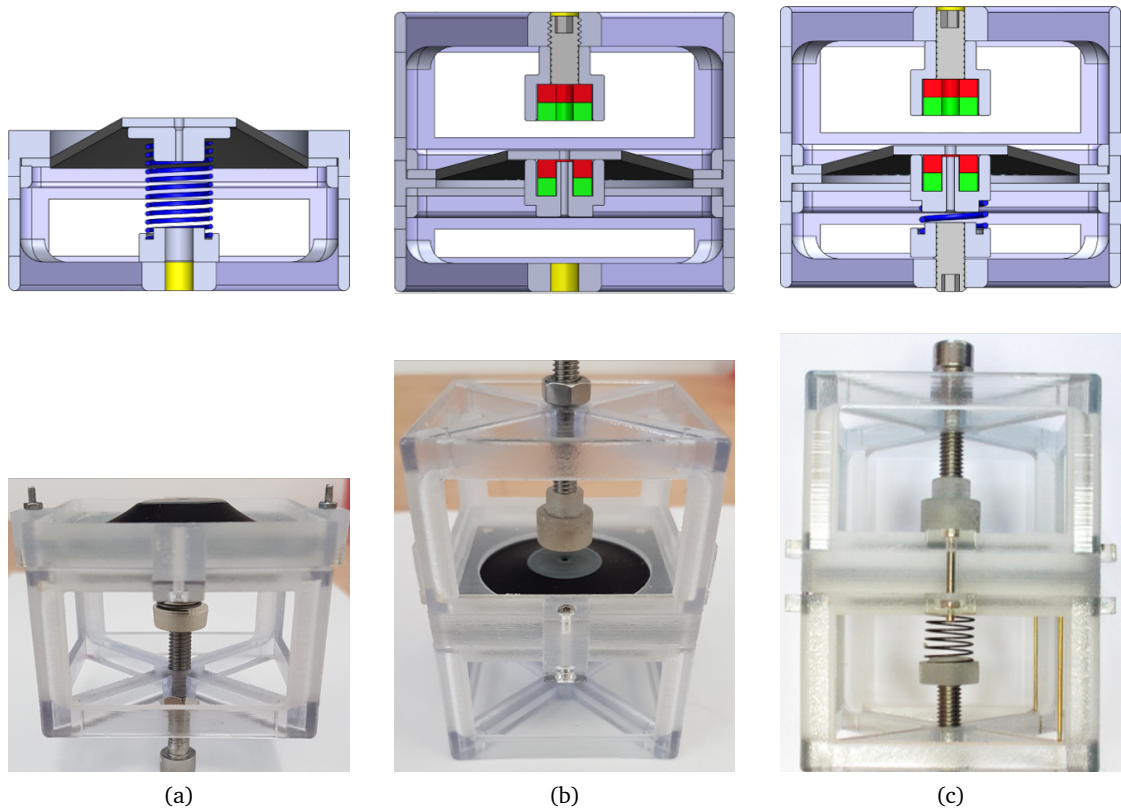


**Figure 3.20:** Assembled demonstrators, CAD model (upper row) and 3D printed prototypes (lower row). LBS biased system (a), PM biased system (b) and LBS+PM biased system (c).

trolled via a NI LabVIEW interface. The resulting stroke over applied voltage curves are shown in Figure 3.21 for all 4 actuator designs. The LBS biased system characterization in Figure 3.21 (a) shows an achieved stroke of  $\Delta h_{LBS} = 1.2$  mm without applied load and an achieved stroke of  $\Delta h_{LBS} = 1.1$  mm for a load of 1.5 N, yielding a perfect match to the theoretical prediction. Also, for the stable PM biased actuator system, the measured stroke fits the prediction of  $\Delta h_{PM}^{st} = 3.9$  mm (see Figure 3.21 (b)) in a remarkable agreement. The design for the combined LBS+PM system is validated without external load and with an external load of 1.5 N. The measurements are shown in Figure 3.21 (c), yielding yet another match to the predictions with an error of 0.1 mm,  $\Delta h_{0N} = 3.1$  mm and  $\Delta h_{1.5N} = 1.6$  mm. Finally, the stroke of the unstable PM biased actuator is shown in Figure 3.21 (d). The predicted stroke agrees with the measurement, except an error of 0.1 mm, providing  $\Delta h_{PM}^{unst} = 5.4$  mm. To allow a better comparison and evaluation of the design methodology effectiveness, all theoretical predictions and experimental results are reported in Table 3.

A more detailed examination needs to be performed for the unstable PM actuator. Its force-displacement curve differs highly from the other systems. While dynamic effects are neglected for the stable actuators during the design process, the snapping behavior of the unstable actu-

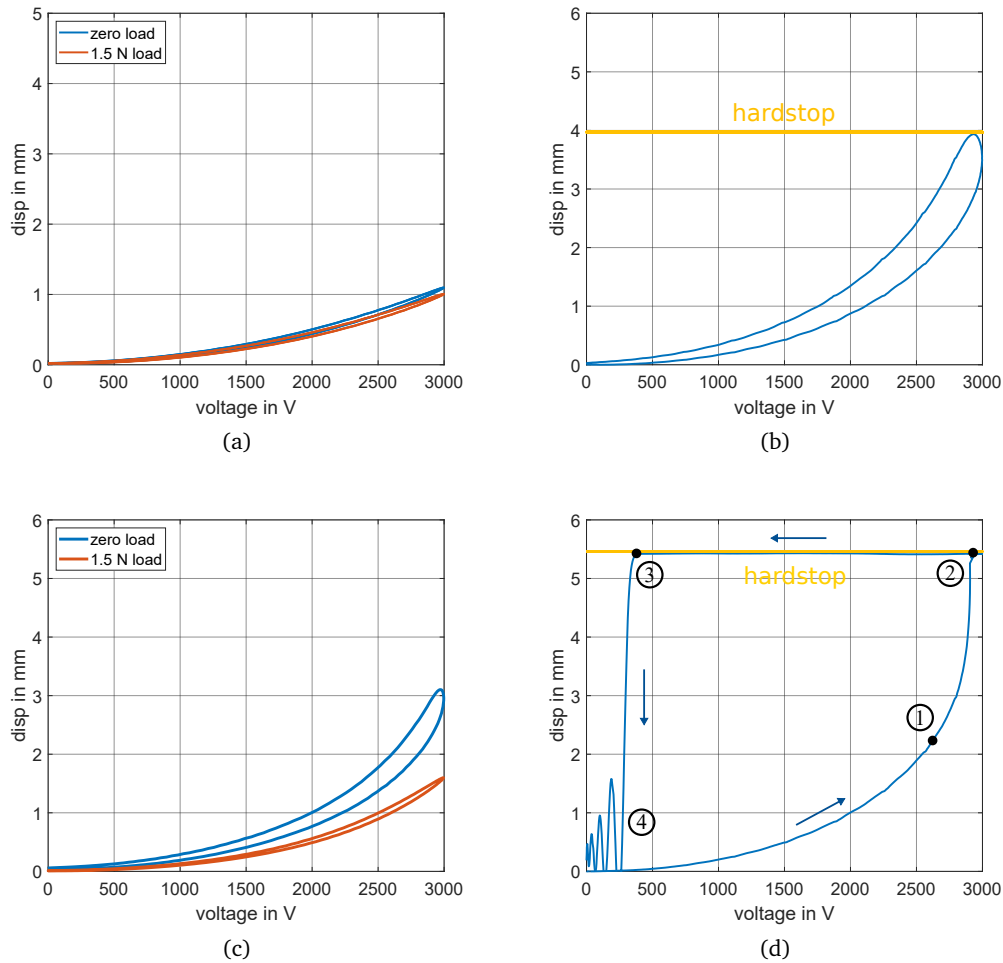


**Figure 3.21:** Stroke over voltage measurements for all designed actuator systems: LBS (a), stable PM (b), LBS+PM (c) and unstable PM (d).

ator is predicted. However, the design does not consider inertial effects by itself, the prediction of dynamics is due to the mentioned interpretation of the optimal design. The measurement of the unstable PM actuator is shown in Figure 3.21 (d). There are 4 points marked in the curve, which are important for the actuator behavior. When the voltage is applied up to approximately 2700 V, the system behaves stable (marker 1). Then, the PM exceeds the DEA's stiffness, leading to a collapse of the system onto the hard stop (marker 2). Since the PM stiffness exceeds the DEA stiffness until the voltage drops below approximately 300 V (marker 3), the actuator is stuck at the hard stop. At this point, the actuator stiffness exceeds the PM stiffness, and the actuator snaps back into its original position. Note that the oscillatory behavior at marker 4 is not a system characteristic, but a dynamic effect from the measurement, which is performed at a frequency of 1 Hz, and the snapping of the DEA in combination with the mass of the PM leads to these oscillations.

In conclusion, the PM biased systems clearly outperform the LBS system concerning the actuator stroke. The mentioned disadvantage of the system biased with PM only working against a load is overcome with the combination of LBS and PM. Comparing the performance to proposed NBS systems, as in [12, 52, 53], similar performance to those of PM are observed. On the one hand, advantages of PM systems over NBS include the possibility of building more compact systems. In addition, by exploiting the inertia of the magnets, the PM biased actuator can be driven in resonance to further magnify the stroke and to produce larger forces. Moreover, the biasing magnets are not physically in contact, allowing to reduce acoustic noise at high frequency activation. This aspect turns out to be of high importance in dynamic applications such as loudspeakers [39]. On the other hand, these inertial effects could represent an issue in some applications, depending on the desired system behavior. Furthermore, in the static case, the weight of the PM exceeds the NBS, which could be critical in low-weight applications. This effect scales with the desired force output, resulting in a considerably larger weight of the biasing PM compared to biasing NBS for high-force applications, such as [40]. Finally, NBS systems can provide a larger stroke than PM systems, due to the possibility of adapting the NBS to the DEA characteristics with fast model-based design methods [11]. The choice among PM and NBS as stroke magnification biasing mechanism depends then on the requirements of the specific application.

	theoretical prediction	exp. measurements
$\Delta h_{LBS}$	1.2 mm	1.2 mm
$\Delta h_{LBS}^L$	1.1 mm	1.1 mm
$\Delta h_{PM}^{st}$	3.9 mm	3.9 mm
$\Delta h_{0N}$	3.2 mm	3.1 mm
$\Delta h_{1.5N}$	1.7 mm	1.6 mm
$\Delta h_{PM}^{unst}$	5.3 mm	5.4 mm

**Table 3:** Theoretical predictions and experimental measurements for all examined actuator systems.

### 3.3 Summary and Future Work: Permanent Magnet Biasing

This chapter proposes an advanced design for DEA systems based on a novel nonlinear biasing element, namely permanent magnets. In order to design and optimize arbitrary DEA systems, the concept of a systematic force analysis of the whole actuator system is proposed and its advantages over a design process based on inner forces is exhibited. The discussion of stability for biasing elements with negative stiffness is crucial in order to design stable actuator systems. A description based on energy considerations and a translation to actuator force diagrams yield an optimal concept to predict the actuator's stability during system design. The utilization of permanent magnets increases the actuator stroke compared to a LBS, reaching the same range

as NBS systems. The design for a system biased with PM only is demonstrated. Besides the large stroke of the system, drawbacks are discussed, such as the inability of working against external loads. A structured design process is developed, which enables the design of a system biased with a combination of PM and LBS working against a given load. This design procedure is validated by designing a system working against an exemplary load of 1.5 N. Additionally, the stability of nonlinear DE systems is discussed, in order to harness unstable behavior to increase the actuator stroke of a PM biased system.

In future works, the dynamic behavior of the system requires a more detailed examination, identifying resonances and the possibility of harnessing the force of the oscillating mass. The application of control strategies for the unstable actuator system is another topic of interest, which would lead to a proportional large stroke actuator, which outperforms the stable solution. Overall, PM as a further nonlinear biasing mechanism contributes to the usability of DE driven actuator systems and offers more design flexibility for given load cases. The design process derived in this chapter for PM biased DEA systems provides a tool for the systematic adaption of a DE actuator to a given external load.

## 4 High Pressure Sensors Based on Dielectric Elastomer Technology

While the DE technology is established in the scientific field of smart actuators, it is as well arranged in the field of sensor applications. The fundamentals of DE sensors (DES), as discussed in Section 2.3, yield their attractiveness as a low-cost, highly compliant and high-sensitive sensor technology. From the in Section 2.3 described two topologies, namely stack and membrane sensors, this chapter discusses membrane sensors. In Section 4.2.1, a comparison is drawn between stacks and membranes for the specific requirements, but besides that, DES refers to membrane DES in this chapter.

While used in different sensor applications, such as force sensors [67, 68], strain sensors [65] or health monitoring applications [88, 89, 90, 91] (see Figure 2.9), this chapter deals with high pressure sensors. Literature proposes different pressure sensors based on DE technology, e.g., a polyurethane film with gold metallization [72] for pressures up to 1 bar, a pressure and shear force sensor with a range up to 0.25 bar [91], or a capacitive compression sensor [73] for up to 1 bar. Further pressure sensors with a restricted pressure range are proposed by Mannsfeld *et al.* [92] and in the first part of [4]. All these sensors have in common, that the measurable pressure range is restricted to the order of 1 bar. This is due to the fact, that a DE consists of a soft elastomer. From a mechanical point of view, DE sensors rupture under large loads, i.e., large pressures. In order to overcome this limitation, York *et al.* [4] proposes a transmission barrier between pressurized medium and DES (see Figure 4.1). However, this publication states a maximal pressure of approximately 0.7 bar.

In this chapter, sensors for high pressure applications based on DE technology are introduced. Despite the restriction of pressure range in recent literature, advanced design concepts for sensors are developed, which allow the measurement of pressures larger than an order in magnitude compared to the state of the art. In order to achieve this aim, the concept of a transmission barrier [4] is revisited and enhanced in order to obtain a sensor for the mentioned pressure range. In Section 4.1, a fluidic pressure sensor for pressures up to 10 bar is developed, which bases on an intrusive measurement concept. In this context, intrusive means that the pressurized system is unsealed in order to position the sensor and execute a pressure measurement directly at the medium. In contrast to the intrusive concept, Section 4.2 proposes a fluidic pressure sensor for polymer tubes, which bases on a nonintrusive concept and is able

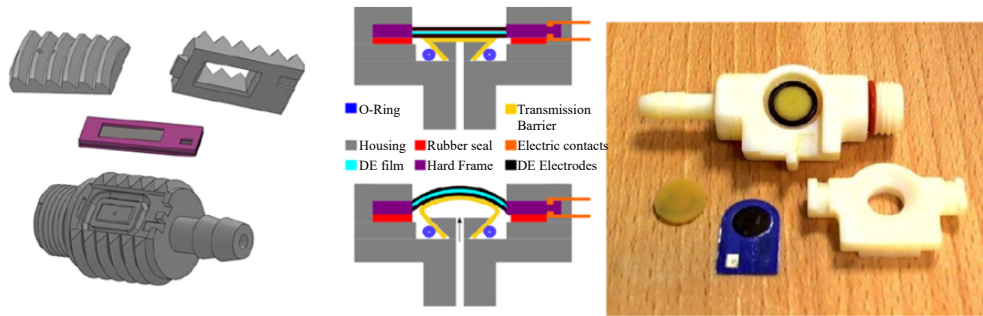


**Figure 4.1:** Concept of a fluidic pressure sensor, without a transmission barrier (left), with a latex transmission barrier (middle) and an assembled prototype (right) [4].

to measure pressures up to 62 bar. For both concepts, a transmission barrier is introduced and investigated, which translates the system pressure to a deformation. The DES then measures the deflection of the transmission barrier, therefore must not endure any large forces.

#### 4.1 Intrusive Membrane Pressure Sensor

One goal for the development of an intrusive high pressure DES system is the comparison to a state-of-the-art industrial pressure sensor, namely the Bosch SMP137 [93]. The SMP137 is a fluidic pressure sensor for a pressure range up to 100 bar, with a diameter of 19 mm and a thickness of 9 mm (see Figure 4.2, left). The exact pressure range depends on the used model. Here, a version with a maximal range of 20 bar is used. The in this section developed DE sensor aims at a maximal pressure of 10 bar, due to its limitation in sealing the system with a housing which is 3D printed. Hence, a higher pressure is limited by the housing itself, not the actual sensor unit. Additionally, the conclusion of this section describes a straightforward way for scaling the sensor range by adjusting the transmission barrier.

The concept of state-of-the-art DE pressure sensors is limited due to their small pressure range. While an attempt discussed by York *et al.* [4] shows the potential of using a transmission barrier in order to improve the sensor performance while simultaneously increasing the pressure



**Figure 4.2:** Commercially available pressure sensor SMP137 with a pressure range of 20 bar [93] (left), and a corrugated metal membrane (right).

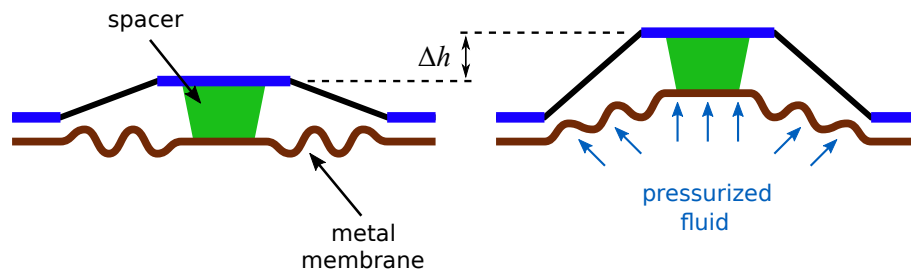


**Figure 4.3:** Concept of DES with metal membrane as transmission barrier, without applied pressure (left) and deformed due to an applied pressure onto the barrier (right).

range, the pressure range is still limited to approximately 0.7 bar due to the small stiffness of the separating latex membrane. The basic idea of a transmission barrier is the translation of a force onto the DES into a force onto the transmission barrier, which deforms under pressure and deflects the DES. In other words, the pressure measurement is translated to a deformation measurement of the transmission barrier. Therefore, the system needs to be unsealed in order to attach the sensor system onto the pressurized area. Resealing must be performed properly in order to avoid any leakage after adding the sensor to the system. The pressure range is then dependent on the transmission barrier itself. The choice of transmission barrier is crucial for this sensor concept.

#### 4.1.1 Increase of Pressure Range Utilizing a Transmission Barrier

An optimal transmission barrier translates the pressure of the system into a possibly large deformation, resulting in a deformation of the DES. The DES, with its structure as a parallel plate capacitor as shown in Figure 2.8, increases its capacitance during deformation. While the transmission barrier needs to perform a large deformation, it is prohibited to deform plastically, due to the loss of a distinct measurement. Any rate-dependent behavior also needs to be minimal, as hysteretic effects degrade the sensor sensitivity and resolution. Here, a tradeoff must be made, choosing a transmission barrier with sufficient elastic range and little hysteretic behavior. The choice in this work are corrugated metal membranes (see Figure 4.2, right), as they are used in commercially available pressure sensors, such as pressure cells or manometers [94]. Common materials are NiBe, CuBe, or different types of steel (1.4435, 1.4571, C75), which are resistant to corrosion up to different degrees (dependent on the pressurized fluid). Those membranes combine two effects. First, these metals all have a perfect linear-elastic range up to 0.2 % [95], with a negligible hysteresis. This local deformation of 0.2 % is enlarged by the corrugated structure of the membrane. The overall structure is able to deform much further without deforming plastically, because locally, each ripple stays under the yield strength. Figure 4.3 shows the concept of a cone-shaped DES in combination with a metal membrane as transmission barrier. A spacer between DES and membrane biases the DES and

sets its operating point. While no pressure is applied, the metal membrane is in its undeflected state and the DES is deformed due to the biasing spacer (see Figure 4.3, left). When a pressure is applied underneath the metal membrane, the membrane deflects and deforms (see Figure 4.3, right). The DES deforms equally, producing a stroke  $\Delta h$  which results in a capacitance change as described by equation (2.4).

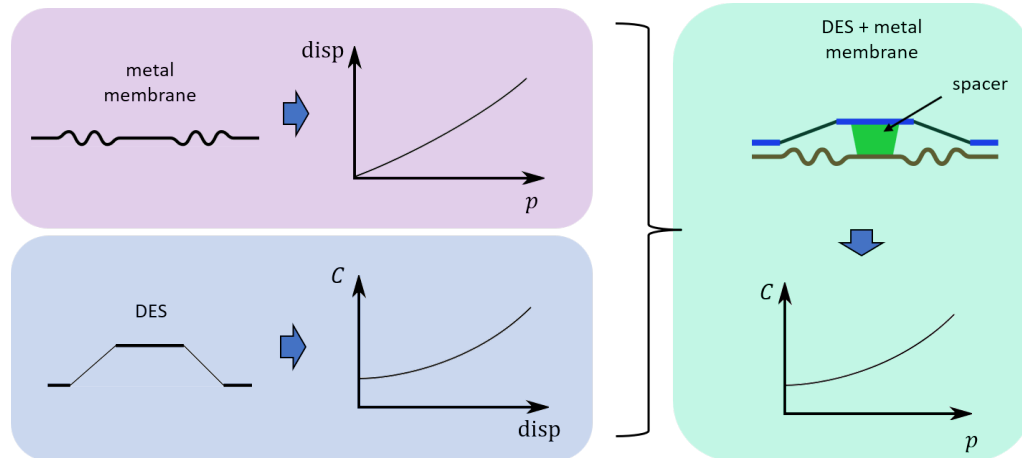


**Figure 4.4:** Measurement paradigm: the characterization of metal membrane (purple box) and the characterization of the DES (blue box) lead to the overall sensor characteristic curve (green box).

The overall measurement paradigm of the sensor system is depicted in Figure 4.4. The two elements interacting with each other must be characterized. The metal membrane stroke must be measured while applying pressure (purple box), and the capacitance change of the DES must be measured over the displacement (blue box). Both characteristics are coupled through the displacement, yielding the sensor's characteristic curve of capacitance change over applied pressure (green box). The spacer sets the operating point between the two systems. In the subsequent sections, these characterizations are preformed, including a comparison of different metal membranes and DES in order to optimize the system performance.

#### 4.1.2 Characterization of the Transmission Barrier

The in this section characterized metal membranes have been purchased at *Membranenbeck GmbH* [96], with the restrictions of a size comparable to the Bosch SMP137 and a thickness which enables sufficient deflection in the pressure range up to 10 bar. Four membranes with different geometries are examined, all of them depicted in Figure 4.5. The membrane label name, inner and outer diameter and thickness are stated in Table 4. Note that for nomenclature, the membrane identifiers of the manufacturer are adopted (Table 4, first column). Besides the outer diameters, also the shape and number of corrugations change for each membrane type. The membrane has to ensure elastic deformation without reaching the plastic

range, therefore, the maximal yield stress is prohibited to exceed. Linear mechanics states, that the thicker a bending structure, the larger the resulting stresses. Applying this theory to the corrugated membranes which are bent locally when pressure is applied, the thinnest membrane must ensure elasticity for the largest range, while simultaneously providing the largest deformation.

metal membrane identifier	thickness in $\mu\text{m}$	inner diameter in mm	outer diameter in mm	meas. force at 0.7 mm disp in N
10502	150	3.6	18.6	34.9
10454	120	2	17.2	31.5
10407	90	3	17.2	27.6
10433	40	2.7	11.6	14.7

**Table 4:** Comparison of metal membranes: geometry, thickness and measured force at 0.7 mm displacement.

Following this observations, Table 4 yields the best result for the membrane type 10433. However, the area the pressure acts onto the membrane is smaller compared to the other membranes, leading to a smaller force acting onto the metal membrane surface. Additionally, the handling of small membranes in order to build a housing and ensure proper sealing is more difficult compared to larger membranes. Comparing the remaining three membrane types, 10407 with a thickness of  $90\mu\text{m}$  promises good results. Still, the membrane has to stay in its elastic range. In order to ensure elasticity, the membranes are experimentally characterized. The force-displacement of each membrane is experimentally examined with the setup depicted in Figure 4.6. They are clamped into a 3D printed frame (Figure 4.6, right), while a linear actuator with an attached load cell (Futek LSB303) deflects the membrane (Figure 4.6, left).

The experiments are performed at 1 Hz, with a displacement of 0.7 mm. The most important observation in Figure 4.7 concerns the elastic range. For the chosen maximal deflection of 0.7 mm, all membranes show a different amount of hysteresis and plasticity. The result of this tensile test is shown in Figure 4.7. The hysteresis of type 10407 (yellow line) is the smallest, while its maximal force is the lowest. This first observation confirms the theory by which

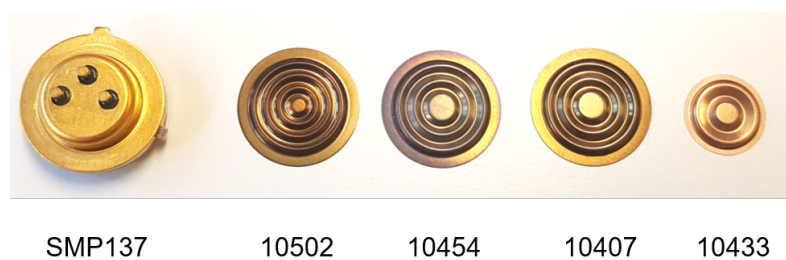


**Figure 4.5:** Different metal membranes in comparison to the Bosch SMP137 pressure sensor.

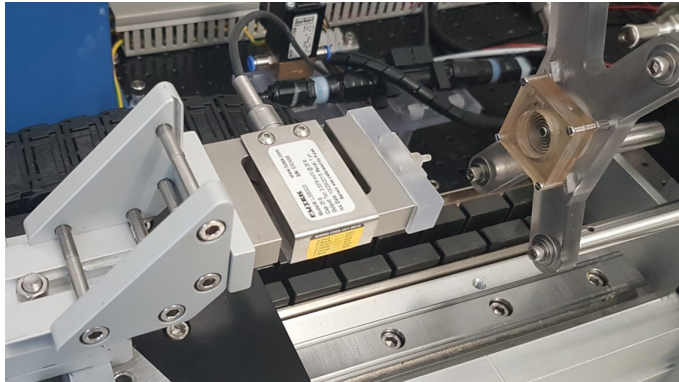


**Figure 4.6:** Test setup for measuring the metal membrane's force-displacement characteristics.

the membrane thickness influences the stiffness significantly. The so far preferred membrane type 10407 is the softest membrane, therefore yielding the largest stroke when a pressure is applied. Note that a specific amount of hysteresis is inevitable, due to the stiffness of the setup which partially consists of 3D printed parts, and further tolerances. Furthermore, type 10407 completely returns to its initial position, while the other membrane types stay deformed (see the offset for the red and blue curve after the first cycle). All these observations predestine type 10407 as the best transmission barrier for the DES system and is from now on referred to as metal membrane.

In order to follow the design paradigm in Figure 4.4, not the force-displacement of the membrane is of importance, but the deformation under fluidic pressure. An experimental setup is built in order to characterize the metal membrane, based on the schematics shown in Figure 4.8. A hydraulic pump (HP) applies pressure to the metal membrane (MM), which is clamped on the edge and the deformation is measured with a Keyence LK-G87 laser sensor (LS) at the

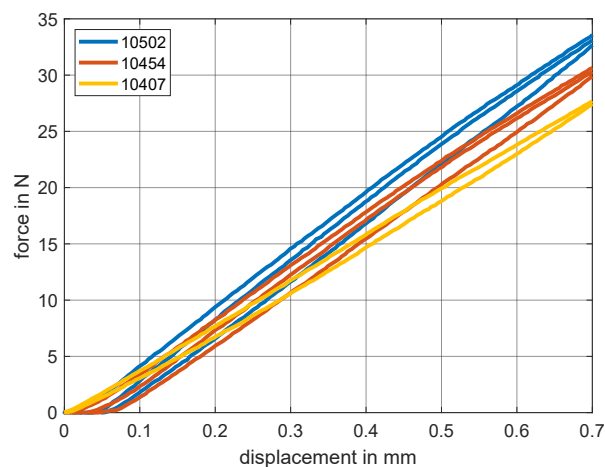


**Figure 4.7:** Force-displacement measurements of all metal membranes show the difference in stiffness.

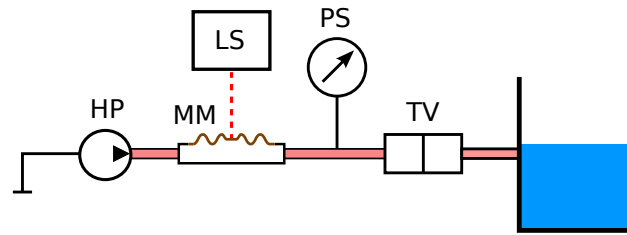


**Figure 4.8:** Schematics of a test setup for characterizing the metal membranes under pressure application, including a high pressure source (HP), a laser sensor (LS), the metal membrane (MM), a pressure sensor (PS) and a throttle valve (TV)

membrane's center point. The reference pressure sensor (PS) is a Hydac HDA 4745. The hydraulic pump used in this experiment is flow rate controlled, therefore a throttle valve (TV) is used in order to set the maximal pressure applied to the system. A pressure ramp is applied to the system, until the desired maximal pressure of 10 bar is reached. The results are shown in Figure 4.9, yielding a displacement of 0.65 mm of the membrane. Based on these measurements and the size of the metal membrane, the DES are designed in the subsequent section.

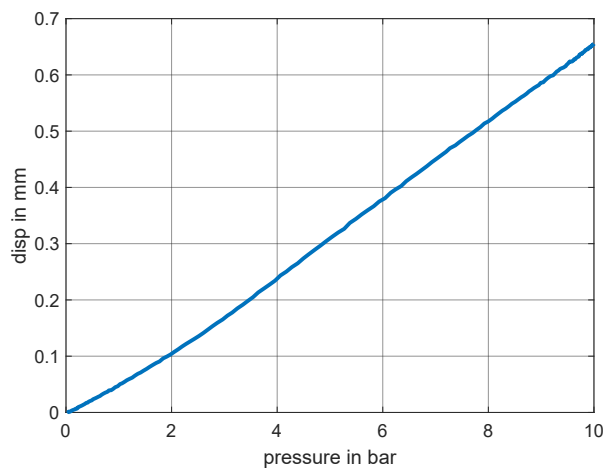


**Figure 4.9:** Displacement-pressure characterization of metal membrane 10407.

### 4.1.3 Sensor Design, Manufacturing and Characterization

In general, the capacitance change depends on the area of the DES and its thickness. The thickness is defined by the used Silicone film from *Wacker AG*, namely *Elastosil 2030* with a thickness of 50  $\mu\text{m}$ . The outer diameter of the sensor is restricted through the target of staying in the size range of the Bosch SMP137 and the size of the metal membrane. Hence, the outer diameter of the DES is desired to be in the range of the metal membrane, which is around 17 mm (see Table 4). Two different sensor sizes are manufactured, both are shown in Figure

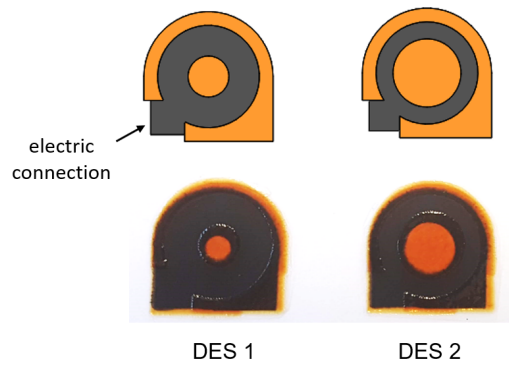


**Figure 4.10:** Two designed DES with different geometries, the CAD drawing and the manufactured sensors.

4.10. The upper row shows the CAD drawing of the sensor electrode and epoxy frame, which is important for mechanical stabilization. The lower row shows the manufactured sensors. Both designs have an edge without printed frame material. Those edges are designed in order to connect the sensors for performing the capacitance measurement. The sensor geometries are listed in Table 5. Note that there are two values for the inner radius  $r_i$  and  $r_{i,e}$ , and the outer radius  $r_o$  and  $r_{o,e}$ . While the radius  $r_i$  corresponds to the radius of the epoxy frame, the inner radius of the electrode  $r_{i,e}$  is smaller. The reason lies in the manufacturing process. Between the screen-printing of electrode and frame material, a small misalignment is inevitable. The offsets of electrode radius and frame radius permits that in the deforming area (the area which is not fixed by the epoxy frame) the electrodes always overlap completely. This overlap is visible in Figure 4.10, lower row. Through the epoxy middle piece of the DES, the electrode overlap is shown. Also, a small misalignment is visible. While the outer radius is equal for both DES and comparable to the metal membrane dimensions, the inner radius is varied. The capacitance of the actuators is calculated based on the parallel plate capacitor equation (2.3), resulting for incompressible silicone to

$$C_0 = \epsilon_0 \epsilon_r \frac{A_0}{d_0} = \epsilon_0 \epsilon_r \frac{\pi (r_{o,e}^2 - r_{i,e}^2)}{d_0}, \quad (4.1)$$

With a relative permittivity  $\epsilon_r$  of 2.8. An important fact is the stretching of the silicone film during manufacturing by 10 % in both directions, leading to an actual initial thickness  $d_0 \approx 41 \mu\text{m}$ . This model yields nominal sensor capacitances of 129 pF for DES 1 and 106 pF for DES 2.

The measured nominal capacitances are also shown in Table 5 and provide a satisfactory agreement to the model capacitances. The small deviations are due to the mentioned misalignment,

DES	$r_i$ in mm	$r_{i,e}$ in mm	$r_o$ in mm	$r_{o,e}$ in mm	$C_0$ in pF	$C_0^{meas}$ in pF
1	3	2	7.5	8.5	129	126
2	5	4	7.5	8.5	106	104

**Table 5:** Comparison of DES: dimensions and capacitance.

which leads to the electrodes not forming a complete capacitor ring, but losing some overlapping area at the edges.

In order to choose between both DES, an experimental characterization of both geometries is performed. The process corresponds to the characterization described in Section 2.3, using the described test setup. The capacitance change over displacement for both DES is shown in Figure 4.11. Note that both measurements show nearly no hysteretic effects. This behavior is well described in [4] and arises from the fact, that the hysteresis in force-displacement curves of DE actuators, such as Figure 2.7, is a viscoelastic effect induced by the reaction force. The capacitance, however, is nearly nonhysteretic, yielding a distinct sensor characteristic. As shown in Figure 4.11, DES 1 is deflected further, because its larger free area permits larger deformations without damaging the sensor. Although DES 1 has a larger capacitance, the capacitance change of DES 2 is higher, even for a smaller displacement. This effect is based on the larger stretch of DES 2. Assuming a deformation of the DES as a truncated cone as depicted in Figure 4.3, we define a strain  $\epsilon$  of the active area as

$$\epsilon = \frac{\sqrt{\Delta h^2 + (r_o - r_i)^2}}{r_o - r_i} - 1, \quad (4.2)$$

with  $\Delta h$  being the maximal out-of-plane displacement of the DES. For DES 1, the resulting

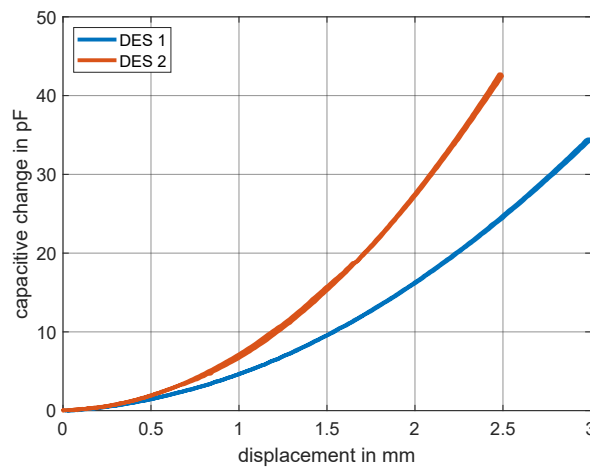


**Figure 4.11:** The capacitance change over displacement for both DES shows different sensitivities.

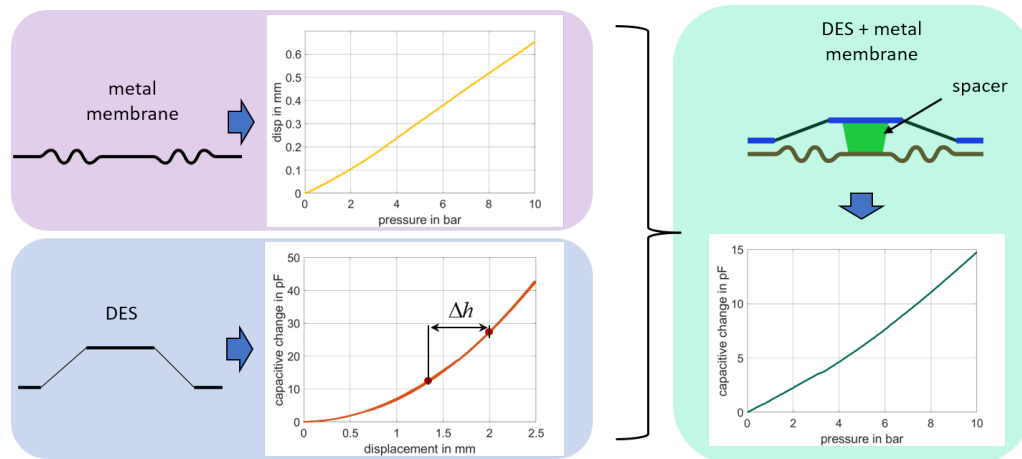


**Figure 4.12:** Measurement paradigm with characterized metal membrane and DES leads to a prediction of the sensor characteristics.

strain equals  $\epsilon_1 \approx 20\%$ , while for DES 2, the strain results to  $\epsilon_2 \approx 41\%$ . This significantly larger strain results in a much smaller thickness, which influences the capacitance change drastically, as equation (2.3) states. Hence, the slope of the characteristic curve of DES 2, which represents the sensor sensitivity, is larger, further predestining DES 2. The only disadvantage of DES 2 is its smaller possible displacement  $\Delta h$  due to the larger stretch. However, the maximal stretch of the DES is provided by the displacement of the metal membrane, which deflects around 0.7 mm for a pressure of 10 bar. In this case, a stretch range of 2.5 mm for DES 2 is sufficient for this application.

#### 4.1.4 System Design and Housing

Now that the transmission barrier is characterized (displacement over fluidic system pressure), and the sensor element is characterized (capacitance change over displacement), the left side of the measurement paradigm shown in Figure 4.4 is completed. In order to extract a prediction for the sensor characteristic, which is the capacitance change over the fluidic system pressure, one last step is missing. The operating point of the DES must be chosen. Figure 4.11 shows an increasing slope of the DES over the displacement, which equals the sensor sensitivity. Ideally, the operating point is chosen so that at 10 bar, the deflection equals 2.5 mm. However, due to tolerances in the sensor assembly, which consist of 3D printed parts, and possible misalignments between metal membrane, DES and spacer, the worst case would provide a larger stretch to the DES, which could induce damage. In order to compensate this unfavorable superposition of tolerances, the operating point is chosen 0.5 mm below the optimum, which means that at 10 bar the DES is deflected by 2 mm. In this case, in the reference state without any applied pressure, the DES must be pre-deflected by the spacer for 2 mm minus the displacement of the metal membrane of approximately 0.7 mm, resulting in a pre-deflection of

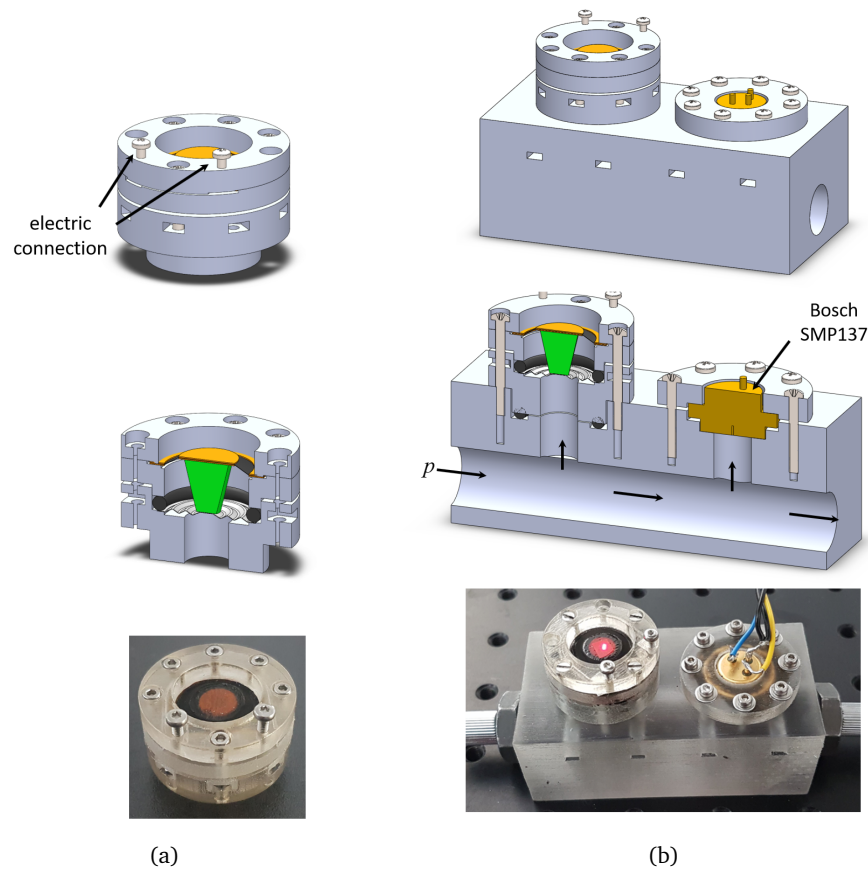


**Figure 4.13:** CAD drawings and prototype of a sensor housing (a) and a test setup for comparison between DES prototype and Bosch SMP137.

the DES of 1.3 mm. The operating point is inserted into the DES curve in Figure 4.12 as a red dot. The red dot moves along the DES curve when the metal membrane deforms due to the applied pressure. Coupling both diagrams yields an estimation of the sensor characteristics, which is shown on the right side of Figure 4.12. A maximal capacitance change of 15 pF is predicted for an applied pressure of 10 bar.

In order to withstand the system pressure up to 10 bar with a 3D printed prototype, a robust housing is designed which is able to ensure sealing between the pressurized fluid and the metal membrane. The design of such a housing is shown in Figure 4.13 (a), CAD drawing (upper part), cross-section (middle part) and assembled prototype (lower part). The green spacer in the middle part shows the pre-deflection of the DES, setting up the operation point. In order to seal the high pressure area from the low pressure side, the metal membrane is glued into the lower part of the housing with superglue and clamped with an O-Ring from above. Also, the spacer is connected to the middle part of the DES with superglue. The DES is connected via two screws, which push onto the free connection parts of the DES (see Figure 4.10). A

conducting polymer foam with a thickness of  $200\ \mu\text{m}$  is attached to the electrode connectors to prevent the screws from damaging the DES when pressed onto the silicone film.

For testing the sensor and compare it to the Bosch SMP137, a connection block is designed, where both sensors are mounted on. The setup consisting of the 3D printed connection block and both sensors is shown in Figure 4.13 (b), with CAD drawing (upper part), cross-section (middle part) and assembled prototype (lower part). Both sensors are as close to each other as possible, in order to ensure the same pressure at both sensors. The fully assembled block is then attached to the test setup shown in Figure 4.8 in order to characterize the prototype.

#### 4.1.5 Experimental Validation and Discussion of Results

Three experiments are performed and compared to each other in order to characterize the DES system and validate the prediction of the characteristic sensor curve in Figure 4.12. The maximal pressure level is 9 bar, respectively 10 bar. For all three experiments, the system pressure is increased as described for the metal membrane characterization in Section 4.1.2. The reference pressure is measured with the Hydac HDA 4745, while the DES deformation, which equals the metal membrane deformation, is measured with a Keyence LK-G87 laser sensor. The resulting capacitance change is measured with a Hameg HM8118 LCR bridge, performed at a frequency of 1 kHz, for an equivalent parallel RC circuit [84]. The results are shown in Figure 4.14, pressure (a), displacement (b) and capacitance change (c) over time. Due to the different maximal pressure levels and the slight changes in the pressure application (see Figure 4.14 (a)), a comparison of all three measurements is hard to perform in this representation over time. Hence, Figure 4.15 shows all measured values plotted against each other. All three combinations, namely displacement over pressure (a), capacitance change over displacement (b) and finally capacitance change over pressure (c), show a perfect match for all three

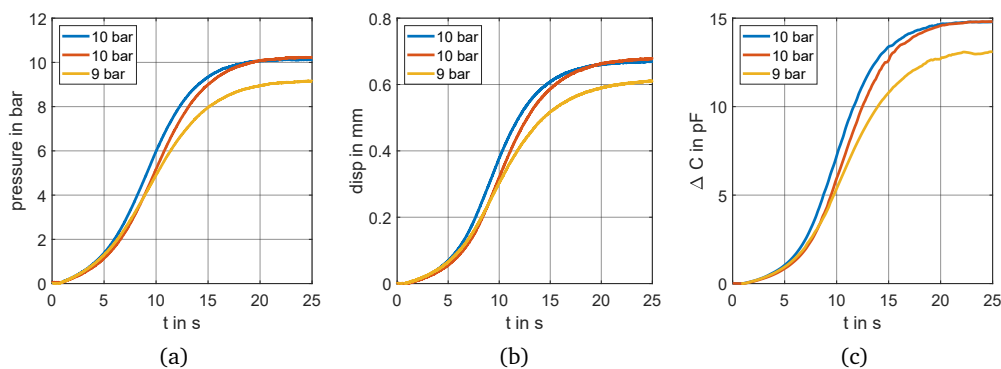


**Figure 4.14:** Characterization of DES sensor, system pressure (a), membrane displacement (b) and capacitance change (c) over time.

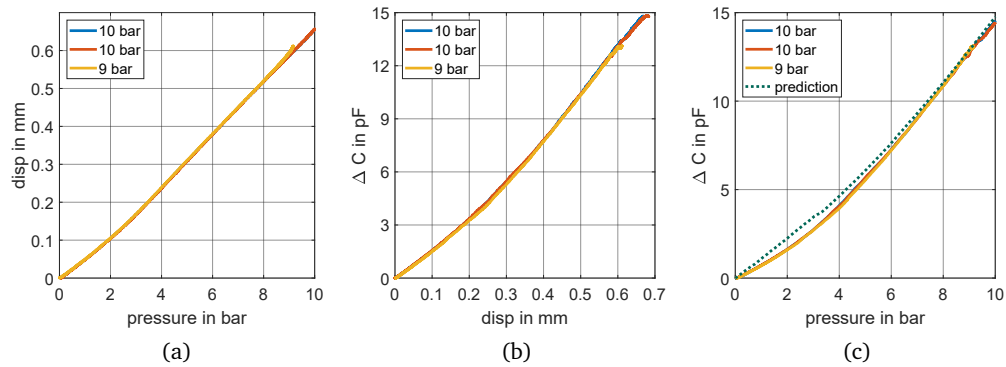


**Figure 4.15:** Characteristic curves of DES sensor, displacement over pressure (a), capacitance change over displacement (b) and capacitance change over pressure (c).

measurements. The plot of capacitance change over pressure equals the sensor characteristic curve, which maps the input (pressure) to the output (capacitance change). Additionally, Figure 4.15 (c) compares the measured sensor characteristic with the prediction shown in Figure 4.12. Especially this agreement is remarkable, because the prediction does not consider any uncertainties concerning sensor mounting, manufacturing tolerances or reaching the exact operation point of the DES with the spacer.

Finally, both sensors, the developed DES system and the Bosch SMP137, are compared. A size comparison can be drawn from Figure 4.13 (b). Although the DES system is larger than the Bosch sensor, most of the size is due to the need of a sealed housing based on 3D printing. A machined housing consisting of a stiffer material, such as aluminum or brass, permits to shrink the housing down to the size of the metal membrane or the DES element itself. In this case, the sizes of both sensors are comparable. For a further experiment, the pressure measurements of the Bosch sensor and the DES system are compared in Figure 4.16 (a) for a maximal pressure of 10 bar. The remarkable match of both curves is emphasized in Figure 4.16 (b), where the error  $p_{Bosch}/p_{DES}$  reaches a maximum of approximately 1 %.

In conclusion, the feasibility of the intrusive sensor concept based on DE technology is shown for high pressure applications. The developed sensor system measures the applied pressure on the same level as the commercially available Bosch SMP137. An important fact is the possibility of scaling the maximal pressure of the DES system by using a thicker, therefore stiffer metal membrane. However, in this case, the elastic range of the membrane needs to be redetermined. A further decrease of sensor size is achievable by using a smaller metal membrane, e.g., membrane 10433 in Figure 4.5, and an adapted DES with smaller outer diameter. Note that the assembly process for a prototype would be more complex, which is why the larger version has been pursued in this work.

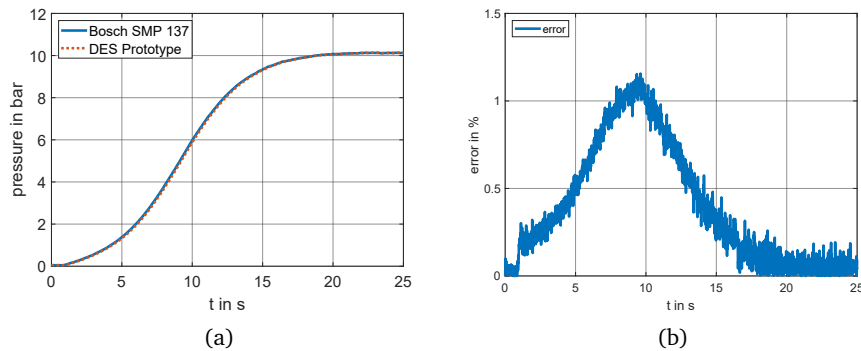


**Figure 4.16:** A comparison between DES and Bosch SMP137 shows a remarkable correlation, pressure over time (a) and error between both sensor signals (b).

## 4.2 Nonintrusive Membrane Pressure Sensor for Polymer Tubes

In the previous section, an intrusive high pressure sensor based on DE technology with remarkable performance compared to a state-of-the-art sensor is presented. However, the concept requires unsealing of the pressurized system in order to mount the sensor. The sensor requires contact with the fluid to measure the pressure. In this section, another advanced approach is described, which permits to measure high pressure up to 62 bar inside sealed systems, more precisely, inside a fabric-reinforced polymer tube.

In the medical field, injector systems are used to inject contrast fluid into the patient while performing a computer tomography (CT) scan, as well as during an angiography or a magnetic resonance imaging (MRI) scan. These injector systems build up pressure in a range up to 83 bar, due to the required flow rates and the small diameter of the injection needle. Figure 4.17 (a) shows an angiography injector, namely the Accutron HP836 [97] of the company Medtronic AG. An important implicit control variable of this injector is the system pressure. However, the injector is controlled via the flow rate. When the fabric-reinforced polymer tube (see Figure 4.17 (b)) with the pressurized medium inside bends, the flow of the injection fluid can be interrupted. On the one hand, the contrast fluid is not injected into the patient, yielding to degraded imaging of the CT or coronary angiogram. On the other hand, the system pressure rises until the tube system gets damaged, leading to a leakage in the system. In order to stay below the maximal allowed pressure limit (for high pressure injection tubes 83 bar), the pressure must be monitored during injection. Conventional pressure sensors deliver several downsides for this application. An intrusive pressure sensor demands an unsealing of the system in order to be in contact with the contrast fluid. In this case, a contamination of the injection fluid is not prohibited, therefore an intrusive concept is not suitable for medical injection applications. Nonintrusive concepts based on conventional pressure sensors cannot be applied onto the tube, but onto the syringe which contains the injection fluid. However,

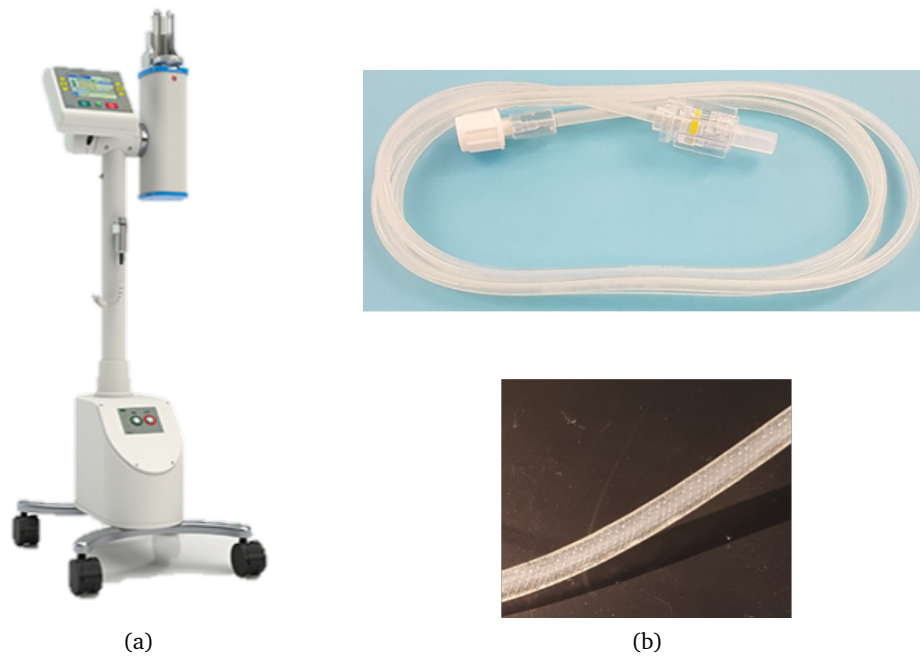


**Figure 4.17:** An injector system for contrast fluids (a) applies pressure inside a fabric-reinforced polymer tube (b).

a measurement as close to the patient as possible is desirable, in order to directly detect any accumulation close to the injection needle. Additionally, a decrease in pressure over the tube is neglected when the pressure is measured at the syringe. A concept based on DE technology offers the possibility of attaching the soft and flexible film directly onto the tube close to the patient. A fabric-reinforced polymer tube which is used for high pressure injections is shown in Figure 4.17 (b), with a zoom in order to point out the fabric reinforcement structure inserted into the tube. The inner radius  $r_0^{in}$  of the tube equals 0.9 mm, while the outer radius  $r_0^{out}$  equals 1.85 mm. A convention for geometry quantities is derived by Figure 2.8, where lower case zeros describe the reference, non-deflected geometry ( $r_0$ ,  $A_0$ ,  $C_0$ ), while lower case ones describe the deformed geometry ( $r_1$ ,  $A_1$ ,  $C_1$ ). With those dimensions, attaching other rigid sensor elements becomes challenging, while a DES is flexible and can be attached onto the tube.

Basically, the concept resembles the paradigm of Section 4.1, with a separating transmission barrier between pressurized medium and DES. While the separating layer is a metal membrane in Section 4.1, here, the polymer tube itself is used as transmission barrier due to its expansion while applying high pressures. Following this concept, the system is not obliged to be unsealed. The required steps also resemble the paradigm in Figure 4.4. A characterization of the separating layer, here the polymer tube, in combination with the characterization of a properly designed sensor, yields the sensor characteristics. Therefore, this section performs these steps, first examining the expansion of the pressurized tube, followed by a design pro-

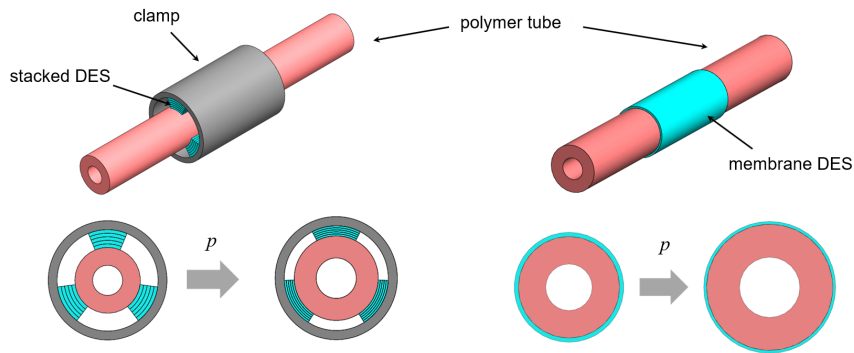


**Figure 4.18:** A comparison of two concepts, DE stack sensors (left) versus a DE membrane sensor (right). The lower part shows the DES deformation under applied pressure  $p$ .

cess of the DES, its manufacturing and characterization. Finally, the DES is assembled onto the tube and the combination of tube and DES is characterized. Additionally, improvement of the mechanical stability and the possibility of detecting air bubbles inside the fluid is investigated.

#### 4.2.1 Nonintrusive Concept: Stack Versus Membrane Sensors

For the nonintrusive concept, sensors are attached to the tube surface, so that the system stays sealed. In order to accomplish this task, two DES topologies are available, namely stack DES [98] and membrane DES [99]. Two possible designs are shown in Figure 4.18, one for stack DES and one for membrane DES. The concept based on stack DES is shown in Figure 4.18 (a), upper part, where three DES stacks are attached around the circumference of the tube. The sensors are held in place by an outer clamp, which also pre-compresses the sensors. When pressure is applied to the tube, it expands, whereby the stack sensors are further compressed, as shown in Figure 4.18 (a), lower part. The resulting change in capacitance can be measured and then correlated to the pressure inside the polymer tube. The second concept based on a membrane DES is shown in Figure 4.18 (b), upper part. Here, the membrane is wrapped around the polymer tube. While applying pressure, the tube expands, stretching the membrane while simultaneously decreasing its thickness, which increases the sensor capacitance (see Figure 4.18 (b), lower part). Again, the change in capacitance can be measured and correlated to the system pressure.

In order to choose between both concepts, a comparison is necessary. There are several advantages of the membrane concept over the stack concept. First, the assembly process for the membrane concept is simpler. To attach the sensor, a membrane can be wrapped around the tube. For the stack concept, the stack sensors have to be attached onto the tube, then a clamp has to be placed in such way that the sensors are evenly pre-compressed. Additionally, the

membrane sensors are much softer compared to the stack sensors. While the tube expands, the sensors are prohibited to antagonize this process. Sensor and tube are mechanically connected in parallel for both concepts. The membrane sensors are much softer than the polymer tube, therefore not interfering with the expansion process. For the stack actuators, this approximation may not be legit. Due to the concept of using several layers and compressing the structure, the stiffness of a stack sensor is at least one order of magnitude larger than the membrane one [32]. Also, the outer clamp restricts the expansion process and has to be dimensioned properly, so that the sensors are not pre-compressed too tight, leading to an extreme rise in stiffness. Finally, the membrane sensor measures the change of the whole circumference, while the stack sensors would only measure discrete spots. To avoid this complex of problems, a membrane sensor is chosen in this work. Additionally, for the design process, arbitrary sensor geometries can be manufactured in the cleanroom, thereby the sensor can be fit to the tube expansion behavior without being dependent on commercially available stack sensors. The tube expansion behavior must be examined before designing and manufacturing the DES, which is performed in the next section.

#### 4.2.2 Characterization of the Pressurized Polymer Tube

To characterize the tube expansion behavior, an experimental rig is designed and assembled, with a design similar to the setup used in Section 4.1 for characterizing the intrusive pressure sensor. In order to measure all required quantities, the rig consists of a high pressure source (HP), a laser sensor (LS, Keyence LK-G87), a reference pressure sensor (HP, Hydac HDA 4745), a throttle valve (TV) and a liquid tank (see Figure 4.19 (a)). As a high pressure source, the beforementioned injector system Accutron HP836 is utilized. The throttle valve is used to set the maximal pressure of the performed measurement, because the here used injector system is flow rate controlled, therefore the system pressure is an implicit quantity and has to be manipulated by the valve. Thus, the flow-rate is prescribed for each measurement and the pressure is adjusted by the throttle valve. Note that the highest examined pressure equals 62 bar, although for angiography and CT scans, pressures up to 83 bar are permitted. This is due to the fact, that the used injector system has already an emergency stop implemented when pressures of around 83 bar are reached. In order to avoid triggering this safety measure in all experiments, the examined maximal pressure is decreased. Water is chosen as pressurized medium for improving system handling. To characterize the sensing properties of the DES, the test rig is additionally equipped with a capacitance measurement (CS, Hameg HM8118 LCR bridge). A CAD drawing of the assembled test rig is shown in Figure 4.19 (b).

During the measurement, the tube expands and moves across the setup due to the large forces induced by the high pressure up to 62 bar. To suppress this movement, the tube is inserted into a convex shaped pod, as shown in Figure 4.20 (a). Due to the pod geometry, the tube presses

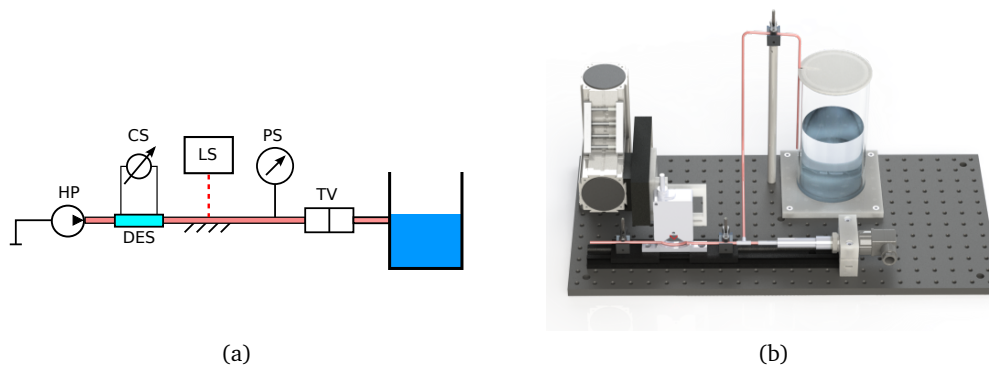


**Figure 4.19:** Test setup to characterize the tube expansion, schematics (a) and CAD drawing (b).

itself into the pod's channel, fixing its position self-contained. The laser sensor then scans the whole tube cross-section. It is attached onto a linear stage driven by a Zaber T-NA08A25 in order to scan the whole tube profile, including the tube pod. The concept is illustrated in Figure 4.20 (b). Experiments are performed, varying the maximal pressure limit through the throttle valve. In this work, three different pressure levels, namely 24 bar, 44 bar and 62 bar, are investigated. First, pressure is applied until an equilibrium is reached, then the whole tube surface is scanned. Results are shown in Figure 4.21 (a), with a zoom to the relevant region in Figure 4.21 (b). The plot can be divided in three parts. The left side of Figure 4.21 (a) shows the scan of the pod, the middle part the tube surface and the right side again the tube pod. Due to the bent tube surface, the laser dot is scattered and therefore the laser sensor is not able to register steep incidence angles. For this reason, not the whole tube surface is depicted in Figure 4.21 (a). The assumption that the tube expands radially symmetric yields that only the point of maximal expansion is of interest. The zoom in Figure 4.21 (b) shows, that the point of maximal expansion does not shift in  $x$ -direction (referring to the coordinate system in Figure 4.20 (b)). This result is verified by several measurements.

To obtain measurements for system pressure and tube expansion over time, the measurement procedure is as follows. First, the tube is set in position inside the pod. Then, the laser sensor

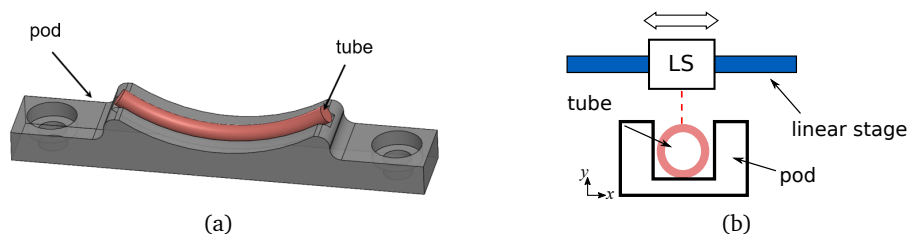


**Figure 4.20:** To ensure a proper fixation of the tube during pressure application, the tube is fixed in a convex pod (a), whereas the laser sensor is mounted on a linear stage in order to scan the whole tube profile.

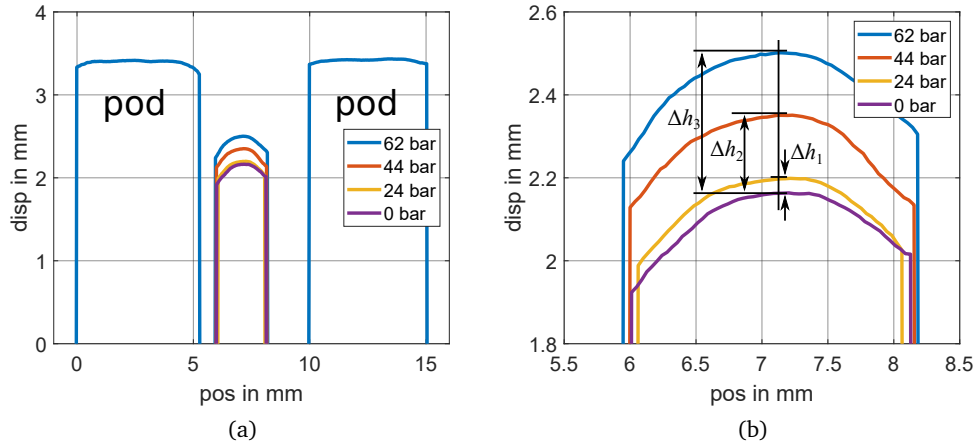


**Figure 4.21:** Tube displacement measurements for different pressure levels, namely 0 bar, 24 bar, 44 bar and 62 bar (a), and a zoom to the relevant area (b).

is positioned so that it scans the point of maximum deflection via a LabVIEW implemented routine which measures the signal of the laser sensor and scans for the highest spot. Subsequently, measurements are performed, by applying a pressure ramp and simultaneously measuring tube expansion and system pressure. The results of these measurements are presented in Figure 4.22, the system pressure  $p$  over time (Figure 4.22 (a)) and the tube expansion  $\Delta h$  over time (Figure 4.22 (b)) for all three pressure levels. Maximal expansions result to  $\Delta h_1 = 58 \mu\text{m}$ ,  $\Delta h_2 = 207 \mu\text{m}$  and  $\Delta h_3 = 314 \mu\text{m}$ , for 24 bar, 44 bar and 62 bar, respectively. The effect that the tube keeps expanding after reaching a constant pressure level is likely caused by viscoelastic effects. Also, it is noted that the effect increases with pressure. Consequences are discussed in detail in Section 4.2.4. Together with specifications concerning a minimal desired capacitance change and some geometry restrictions, the tube expansion measurements allow a design process of the DES based on an analytic model, which is developed next.

### 4.2.3 Sensor Modeling, Design, Manufacturing and Mounting

The approach with a membrane sensor wrapped once around the tube is shown in Figure 4.18 (b). When a membrane sensor of the length  $l$  is unwrapped from the tube, the structure can be approximated as a rectangle, as shown in Figure 4.23. The radial expansion of the tube from  $r_0$  to  $r_1$  due to an applied pressure  $p$  correlates to an increase in circumference, and therefore in surface area. Translated to the rectangular approximation, Figure 4.23 shows surface area  $A$ , thickness  $d$  and capacitance  $C$  for both, the non-deflected (left) and the expanded geometry (right). The length  $l$  is considered constant, because the sensor is fixed onto the tube due to adhesion and cannot expand or reduce in axial direction. A possible change in tube length during pressure application is thereby neglected. Following the description of the capacitance

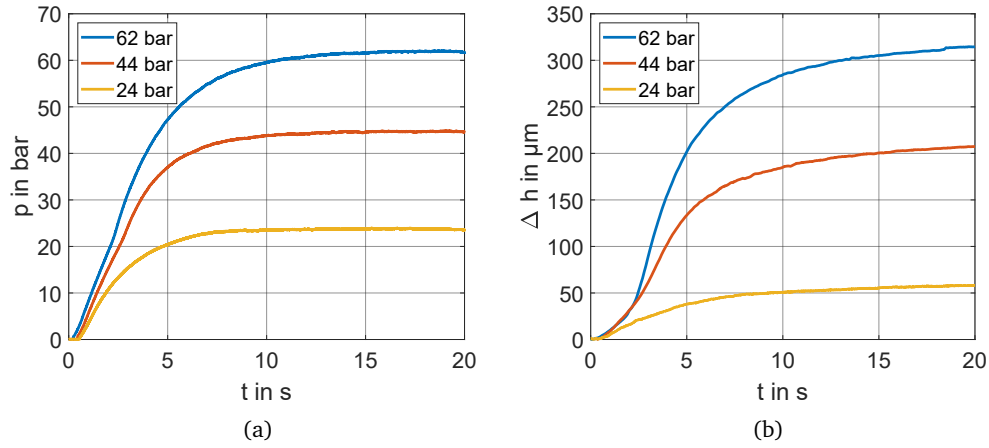


**Figure 4.22:** Experimental results of three tube expansion measurements, system pressure over time (a) and expansion over time (b).

for a parallel plate capacitor given in equation (2.3), the capacitances  $C_0$  for the undeflected DES and  $C_1$  for the deflected DES calculate to

$$C_0 = \epsilon_0 \epsilon_r \frac{A_0}{d_0} = 2\pi l \epsilon_0 \epsilon_r \frac{r_0}{d_0}, \quad (4.3)$$

$$C_1 = \epsilon_0 \epsilon_r \frac{A_1}{d_1} = 2\pi l \epsilon_0 \epsilon_r \frac{r_1}{d_1}, \quad (4.4)$$

which leads to a capacitance change  $\Delta C$  of

$$\Delta C(r_1, d_1) = C_1 - C_0 = 2\pi l \epsilon_0 \epsilon_r \left( \frac{r_1}{d_1} - \frac{r_0}{d_0} \right). \quad (4.5)$$

The membrane material for manufacturing the DES is Wacker Elastosil 2030 with a thickness of  $50 \mu\text{m}$ , which has a relative permittivity of  $\epsilon_r = 2.8$ . Under the assumption of incompressibility, which is legitimate for silicone, equation (4.5) can be simplified to

$$\Delta C(r_1) = 2\pi l \epsilon_0 \epsilon_r \left( \frac{r_1^2 - r_0^2}{d_0 r_0} \right). \quad (4.6)$$

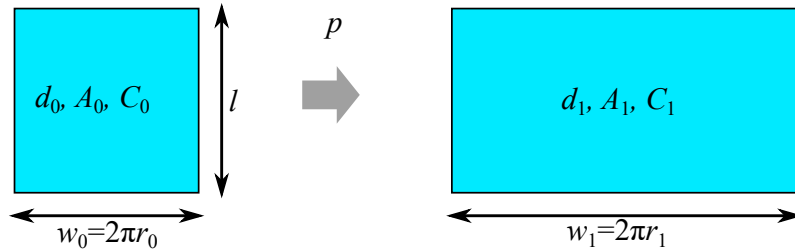


**Figure 4.23:** DES approximated as a rectangle which increases its length while applying pressure.

The experiments performed in Section 4.2.2 measure the expansion  $\Delta h = 2\Delta r = 2(r_1 - r_0)$ . In order to match model and experiments, the capacitance change in equation (4.6) can be expressed in terms of  $\Delta h$ ,

$$\Delta C(\Delta h) = \pi l \varepsilon_0 \varepsilon_r \left( \frac{\Delta h^2 + 4 \Delta h r_0}{2 d_0 r_0} \right). \quad (4.7)$$

Together with the capacitance of the membrane DES, the mechanical properties of the fabric-reinforced polymer tube need to be described as well. To this end, a model based on linear-elastic theory is proposed. Standard linear approaches for the expansion of tube-like structures are not admissible, since they are commonly based on the assumption that the wall thickness of the tube is much smaller than its outer diameter. In this case,  $r_0^{out} \gg r_0^{in}$ , making the thin wall assumption not true. Therefore, a more complex theory has to be applied, as described in [100, Chapter 4]. Here, the displacement  $u$  of a thick-walled circular cylinder with open ends under internal pressure  $p$  is derived to

$$u(r = r_0) = \frac{2r_0}{Y} \frac{p}{\delta^2 - 1}. \quad (4.8)$$

at the outer tube surface. The factor  $\delta = r_0^{out}/r_0^{in}$  is the dimensionless diameter ratio and  $Y$  the Young's modulus of the polymer tube. To this end, linear-elastic theory only holds for small deformations. From equation (4.8), the Young's modulus  $Y$  can be calculated, with the input quantity  $\Delta h = 2u$ , to

$$Y = \frac{4r_0}{\Delta h} \frac{p}{\delta^2 - 1}. \quad (4.9)$$

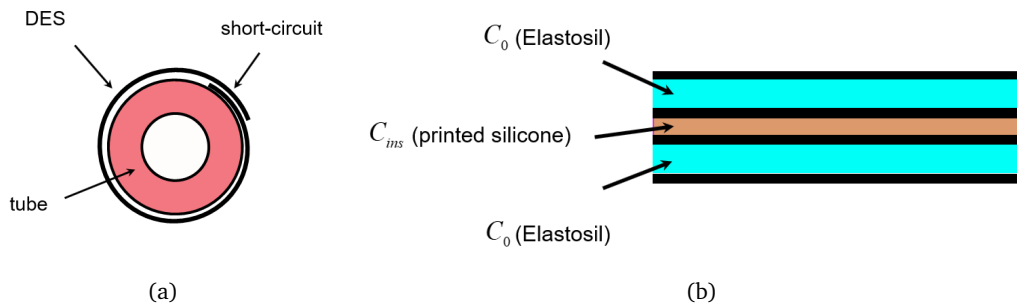


**Figure 4.24:** When the DES is wrapped around the tube, an overlap would short-circuit the sensor (a), therefore a protective layer is printed onto one electrode, which generates a second capacitance (b).

For the three different pressure levels and corresponding tube expansions,  $Y$  is computed to 47 MPa, 24 MPa and 23 MPa, for 24 bar, 44 bar and 62 bar, respectively. The decrease in Young's modulus over pressure is based on the nonlinear behavior of the tube, which yields a decrease in stiffness over deformation for most polymers [101]. The model in equation (4.9) is based on the assumption of small deformations. Based on this observation, only the first value for 24 bar is representative for small deformations of the tube. Nevertheless, another approximated value has not been found in literature and gives at least a first order estimation of the mechanical tube properties of a fabric-reinforced polymer tube.

In order to determine the sensor geometry, some quantities must be chosen, while others can be derived out of chosen restrictions and the developed model for the capacitance change (equation (4.7)). The manufacturing of the sensors is a screen-printing process, as described in Section 2.2 for DE actuators. A commercially available silicone film, namely Elastosil 2030 from Wacker [102] with a thickness of  $50\ \mu\text{m}$ , is used. One of the goals in this section is the comparison of different sensor geometries. A first variation parameter is the width  $w_0$  as defined in Figure 4.23, which possibly leads to multiple layers wrapped around the tube. Hence, there are two types of DES, the ones which are wrapped around the tube once and the ones which are wrapped around the tube multiple times. After printing the electrodes, DES geometries which are wrapped multiple times around the tube receive an additional screen-printed layer of silicone onto one electrode. If this manufacturing step is not performed, both electrodes could overlap as soon as the sensor wraps around the tube once and the DES is short-circuited, as shown in Figure 4.24 (a). This insulating silicone layer is shown in Figure 4.24 (b) in blue. An important fact is, that due to the multiple wrapping, a second capacitance is generated, which is referred to as the capacitance of the insulating layer  $C_{ins}$ . Due to the inhomogeneous and unknown thickness of the insulating layer, this capacitance is hard to estimate. The sensors have two degrees of freedom, namely their length  $l$  and their width  $w_0$  (see Figure 4.23). From here on, the sensor geometry is described as  $l \times w_0\ \text{cm}^2$ . The parameter  $l$  does not change during pressure application, while the parameter  $w_0$  increases

to  $w_1$ . The design is aimed to optimize handling, manufacturing process and capacitance change due to pressure application. In order to receive reliable capacitance measurements, a capacitance change of around 10 pF at 62 bar is chosen. For the handling, the sensor length  $l$  should not be too large, otherwise the mounting procedure becomes more complex. Larger sensor geometries induce larger capacitance changes, so the smallest geometry needs to yield the demanded change. To avoid the effect of overlapping insulating capacitances  $C_{ins}$ , or a short-circuit, the smallest DES should wrap around the tube once. From the geometry, the width is then corresponding to Figure 4.23 (a) the tube circumference  $w_0 = 2\pi r_0 = 11.6$  mm. In order to avoid an overlap of the sensor ends, the width  $w_0^1$  of the first sensor is decreased to 10 mm. Equation (4.7) yields for the maximal tube expansion of 314  $\mu\text{m}$  at 62 bar and a desired capacitance change  $\Delta C$  of 10 pF a length  $l$  of

$$l = \frac{2d_0r_0\Delta C}{\pi l \varepsilon_0 \varepsilon_r (\Delta h^2 + 4\Delta h r_0)} = 10.2 \text{ mm}, \quad (4.10)$$

which is approximated to 10 mm. Considering the notation for the sensor introduced in this section, the now defined sensor geometry is  $1 \times 1 \text{ cm}^2$ . The undeflected capacitance of the first sensor calculates to  $C_0 = 55$  pF based on equation (2.3), and the deformed capacitance to  $C_1 = 65$  pF.

For a comparison, four different sensor geometries are chosen and manufactured, with the sizes  $1 \times 1 \text{ cm}^2$ ,  $3 \times 1 \text{ cm}^2$ ,  $2 \times 3 \text{ cm}^2$  and  $2 \times 5 \text{ cm}^2$ . Due to the tube circumference of approximately 10 mm, the sizes can be interpreted, that the sensors are wrapped around the tube once (first two geometries), and 3, respectively 5 times (third and fourth geometry), while their length  $l$  is varied as well (1 cm, 3 cm, 2 cm and 2 cm). The chosen geometries are manufactured with the in [29] described screen-printing process, where the silicone film is clamped into a metal frame and the electrodes are applied via screen-printing. All four sensor sizes are fabricated (see Figure 4.25 (a)), put onto a stiff support film for better handling and cut out of the metal frame. To ensure adequate electric connection for the capacitance measurement, self-adhesive copper tape is attached onto the printed contacts, as shown in Figure 4.25 (b). The nominal capacitances  $C_0$  are measured and compared to the calculated capacitances from equation (4.3). The results are presented in Table 6, column 1 to 3. The measurements are performed with a Hameg HM8118 LCR bridge and show a remarkable match to the predicted model values. The capacitance measurements are performed at a frequency of 1 kHz, for an equivalent parallel RC circuit [36]. Deviations arise due to a mismatch of the electrodes in the screen-printing process. When the electrodes do not match perfectly, the capacitance drops due to the smaller overlapping electrode area. The occurring error, which is smaller than 3 %,

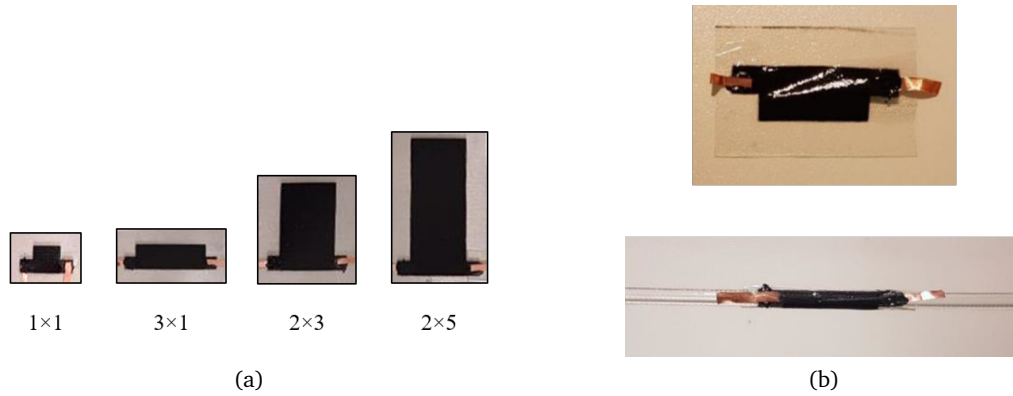


**Figure 4.25:** DES with different geometries (a), cut from the metal frame and mounted onto the polymer tube (b).

is acceptable for the targeted goal of this section, which is measuring the capacitance change during tube expansion and varying the DES geometry.

sensor size	$C_0$ , model	$C_0$ , meas.	$C_0$ , meas. (wrapped)	$\Delta C$ , model (62 bar)	$\Delta C$ , meas. (62 bar)
$1 \times 1 \text{ cm}^2$	55 pF	53 pF	53 pF	8.4 pF	7.8 pF
$3 \times 1 \text{ cm}^2$	162 pF	159 pF	161 pF	25.2 pF	24.7 pF
$2 \times 3 \text{ cm}^2$	324 pF	315 pF	398 pF	50.4 pF	69.3 pF
$2 \times 5 \text{ cm}^2$	540 pF	528 pF	700 pF	84 pF	111.7 pF

**Table 6:** Comparison for all DES sizes: modeled and measured capacitances and capacitance changes during pressure application.

The DES are removed from the support film and wrapped around the tube. Due to the adhesive properties of the silicone film, the sensors stick to the tube, which simplifies this step. Finally, an additional layer of plain silicone film is wrapped around the DES in order to increase the mechanical stability. Due to the comparably low stiffness of the silicone film, the additional silicone layer has no influence on the tube expansion later on. The assembled system is shown in Figure 4.25 (b), exemplary for the second sensor ( $3 \times 1 \text{ cm}^2$ ). This process is repeated for all four sensors, leading to four assembled tube-DES systems. Again, the capacitance after assembly is measured and compared to the measured capacitance before assembly. The results are presented in Table 6, column 4. For sensor 1 and 2, there is a nearly perfect match between unwrapped and wrapped capacitance. However, for sensor 3 and 4, there is a considerable deviation between these values. The reason lies in the additional capacitance  $C_{ins}$  of the insulating layer, as shown in Figure 4.24 (b). This capacitance arises during the wrapping process. For sensor 1 and 2, there is no overlap because the sensor is only wrapped around once, while for sensor 3 and 4, the DES is wrapped around the tube approximately 3, respectively 5 times. The effect also increases when the sensor is wrapped more often around the tube, as Table

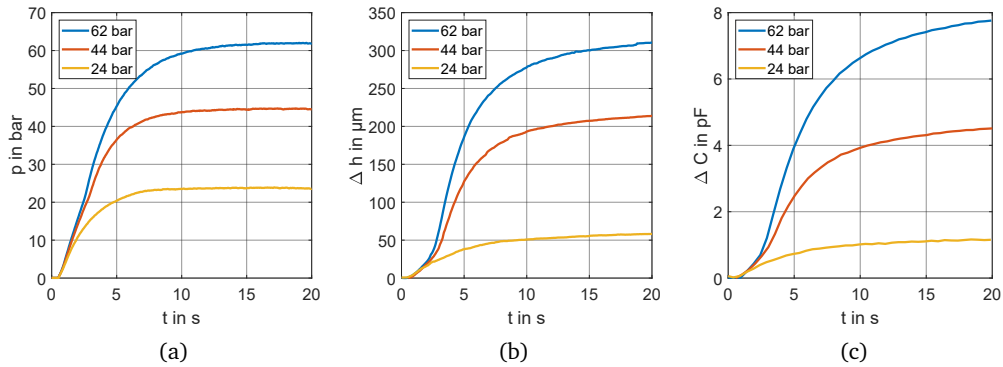


**Figure 4.26:** Results of the system characterization for the  $1 \times 1 \text{ cm}^2$  DES, pressure (a), expansion (b) and capacitance change (c) over time.

4, column 4 states. These results are as expected concerning the discussion of the wrapping process and its influence on the sensor capacitance.

#### 4.2.4 Experimental Validation and Sensor Comparison

The in this section described measurements are split in two parts. First, the characterization of the first sensor is described in detail, deriving characteristic curves for the sensor properties and providing an evaluation. Subsequently, only the final results of the other three sensors are shown and compared to the first sensor, in order to achieve a geometry comparison for the overall sensor concept.

The measurements in Section 4.2.2 are repeated for a tube with sensor 1 attached, extended by the capacitance measurement. Results are shown in Figure 4.26 for all three pressure levels, pressure  $p$  over time (a), tube expansion  $\Delta h$  over time (b) and capacitance change  $\Delta C$  over time (c). There are several observations visible in those measurements. Whereas the pressure reaches a constant level over time, the tube keeps expanding, as already discussed in Section 4.2.2. This behavior is due to viscoelastic effects of the polymer tube. Comparing the tube expansion (b) and capacitance change (c), this effect is visible as well. The maximal achieved capacitance change equals 7.8 pF at 62 bar and deviates from the expected value of 9.8 pF. This is due to the fact, that the sensor is not wrapped entirely around the tube, as described in Section 4.2.3, in order to avoid a short circuit. The sensor length  $w_0^1 = 10 \text{ mm}$  differs from the tube circumference  $2\pi r_0 = 11.6 \text{ mm}$ . The amount of covered tube surface is proportional to the capacitance change, as equation (4.5) states. Hence, the expected capacitance change is scaled by a factor  $10 \text{ mm}/11.6 \text{ mm}$ . Concluding, the expected change of 9.8 pF drops to a change of 8.4 pF, which provides a more satisfying match to the measurement of 7.8 pF. In order to compare the resulting quantities, namely pressure, tube expansion and capacitance

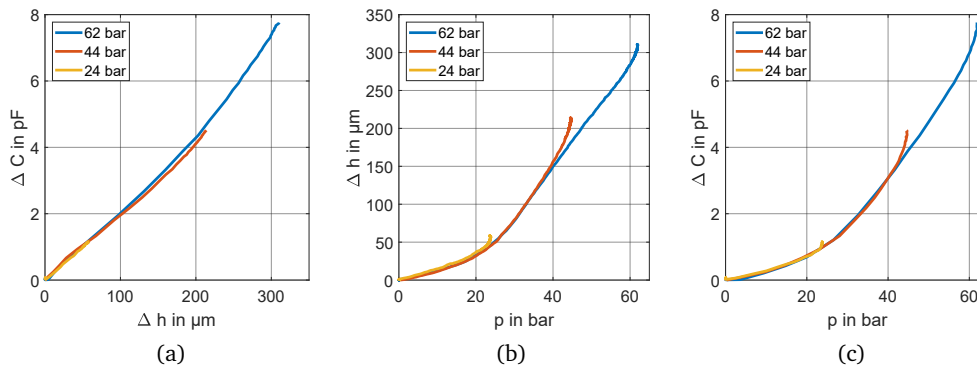


**Figure 4.27:** Characteristic curves for the  $1 \times 1 \text{ cm}^2$  DES tube system, correlations between expansion and capacitance change (a), pressure and expansion (b), and pressure and capacitance change (c).

change, properly, they are plotted against each other in Figure 4.27. The first characteristic curve in Figure 4.27 (a) shows capacitance change over tube expansion and is highly important to the validation of the measurement concept. No matter how far the tube expands or which viscoelastic effects might occur, the sensor expands equally to the tube. Hence, the capacitance change is obliged to change identically, which means that for all three pressure levels, the curves have to match. This match is confirmed in Figure 4.27 (a). The next characteristic curve is tube expansion over pressure in Figure 4.27 (b). Here, the material behavior is displayed. The tube connects the applied pressure to the capacitance change over the intermediate quantity  $\Delta h$ . Neglecting viscoelastic effect, a match of all three experiments is expected as well. Figure 4.27 (b) shows this behavior for nearly the whole pressure range. Although, due to the viscoelasticity, notches at the end of the curves are visible. These notches are a different representation of the effect described above, that the tube keeps expanding at constant pressure levels. Combining both curves by eliminating the intermediate quantity  $\Delta h$ , the characteristic sensor curve is obtained (Figure 4.27 (c)), which correlates the system pressure (input) to the capacitance change (output). Due to the combination of Figure 4.27 (a) and (b), the viscoelastic effects are translated and also visible in the characteristic sensor curve. There are diverse consequences of this system behavior. First, the pressure measurement is restricted to the range without viscoelastic behavior, because otherwise the distinct relation between pressure and capacitance change is compromised. Therefore, the sensor needs to be restricted to pressure signals where no constant pressure level is maintained.

For the application inside a pressure measurement for injector systems, the primary goal is to prevent that the pressure exceeds the maximum allowed threshold. The introduced sensor system overestimates the pressure due to viscoelasticity when a constant pressure level is held. However, an underestimation does not arise. This behavior is practicable for pressure monitoring inside an injector system, because the largest possible pressure level is a peak value, which

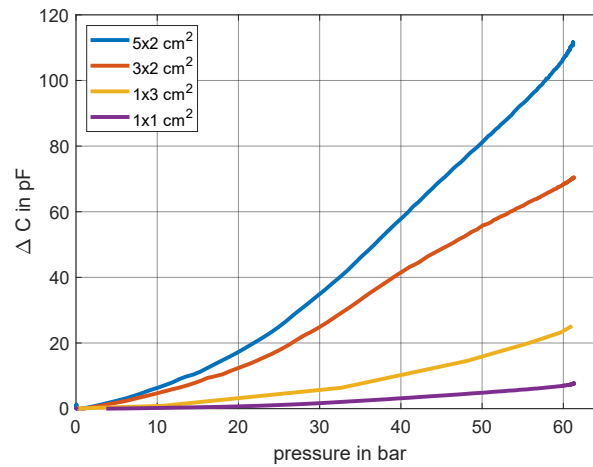


**Figure 4.28:** A comparison of the characteristic curve of all 4 sensors yields different sensitivities dependent on the geometry.

is not held over a longer period. In order to expand the sensor capabilities by considering the viscoelastic effects, a modeling approach of the tube is to be developed, which considers not only the tube expansion, but also the rate-dependency, e.g., with Maxwell branches in a lumped modeling approach as introduced in [103, Chapter 6.10]. Based on such a model, the viscoelastic behavior can be estimated and therefore considered in the sensor characteristics. Note that the viscoelastic effects of the DES can be neglected due to the slow deformation of the tube, where the time constants of the DE's viscoelastic behavior are safely negligible [104].

Equal measurements are performed for the remaining sensor geometries. The characteristic curves for all sensors are shown in Figure 4.28, whereas all calculated and measured capacitances are shown and compared in Table 6. The second sensor with  $3 \times 1 \text{ cm}^2$  is three times longer as the first sensor and is also wrapped around the tube once. The same capacitance change approximation is done for this sensor, including the beforementioned scaling factor, leading to an estimated capacitance change of 25.2 pF and a measured change of 24.7 pF, yielding again a satisfactory agreement. For the third ( $2 \times 3 \text{ cm}^2$ ) and fourth ( $2 \times 5 \text{ cm}^2$ ) sensor, the capacitance estimation is more complex, as discussed in Section 4.2.3. The wrapping process is increasing the capacitance by the insulating capacitance  $C_{ins}$ . The wrapping process results in an increase in capacitance due to the insulating capacitance. Hence, this behavior is expected and does not influence the measurement concept proposed in this work. The feasibility of the nonintrusive sensor concept for an angiography and CT injector system is hereby shown. However, there are further improvements of the sensor concept and additional functionalities, which are discussed next.

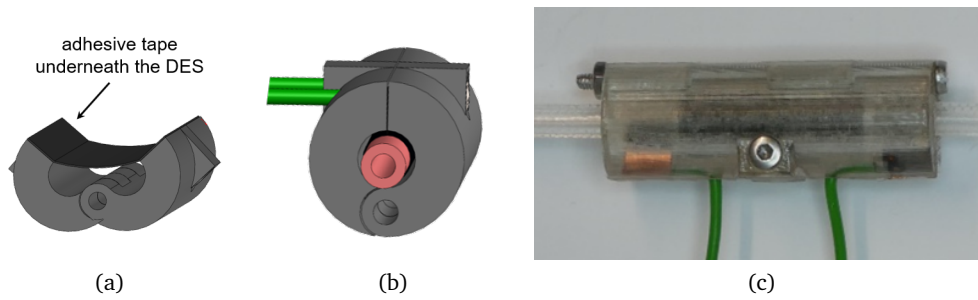


**Figure 4.29:** A reusable clamp including a  $3 \times 1 \text{ cm}^2$  DES (a), the connection is realized with wires and contacts with the DES when the clamp is closed (b), and an assembled prototype (c).

#### 4.2.5 Further System Enhancements

While all sensor geometries perform as desired, the mechanical stability, especially of the electrical connection for the capacitance measurement, is unsatisfying. In order to overcome this issue, a clamp is designed where the DES is attached into with adhesive tape, leading two connecting wires to the LCR bridge. Figure 4.29 shows the CAD design in (a) and (b), with the integrated DES (black) and the connection wires (green). In Figure 4.29 (c), the assembled 3D printed clamp is shown, including a DES ( $3 \times 1 \text{ cm}^2$ ) and attached onto a polymer tube. The electrical connection is generated by closing the clamp, which pushes the wire ends onto the copper contacts. This mechanism is thereby strain-relieved. Another advantage is the reusability of the clamp. The sensor is attached onto the tube by opening the clamp, inserting the tube into the DES and closing the clamp with a screw. The inner radius of the clamp is chosen in such way, that the tube is not fixed in the closed state (Figure 4.29 (b)), so that an expansion while applying pressure is not prohibited by the clamp.

Measurements equal to Figure 4.27 are performed with the system and shown in Figure 4.30. The qualitative behavior agrees with the performance of the DES which are just wrapped around the tube. However, the maximal achieved capacitance change  $\Delta C_{clamp}$  equals 18.7 pF, whereas the wrapped version of the  $3 \times 1 \text{ cm}^2$  sensor achieved a capacitance change of 24.7 pF. The deviation can be explained due to the concept, where the DES is glued into the clamp. In this process, a part of the active area of the DES is also glued into the clamp. This part does not expand anymore, thereby reduces the capacitance change while applying pressure. Note that the clamp design prohibits sensors that wrap around the tube several times. Also, the sensor is not attached onto the tube with an additional layer of plain silicone film. The advantage of this system lies in the fast and straight-forward mounting procedure of the sensor clamp onto the tube, yielding a recyclable sensor system which can be used for several measurements with different tubes. This factor is of interest, because an injection tube is a disposable item which is used once. For the wrapped sensor concept, the sensor needs to be disposed with every tube.

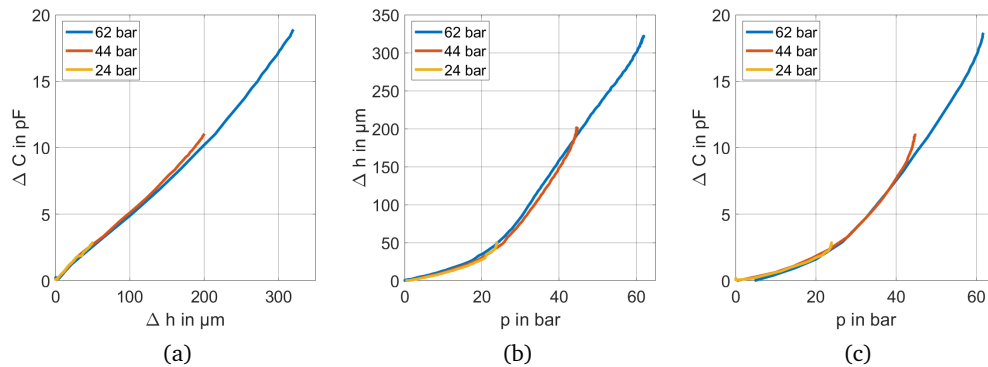


**Figure 4.30:** Characteristic curves for the  $3 \times 1 \text{ cm}^2$  DES system including a clamp, correlations between expansion and capacitance change (a), pressure and expansion (b), and pressure and capacitance change (c).

A further feature the DES offers for angiography and CT scans is its possibility to detect air bubbles inside the system. Injecting air into the cardiovascular system leads to an air embolism, with possible severe consequences such as traumata or reduced cardiac output. A detection of bubbles inside the tube is thereby an important task. In order to study the effect of an air bubble inside the fluid, air is inserted into the system. Air bubbles inside a polymer tube are shown in Figure 4.31, with a larger bubble traveling from left to right, followed by a smaller bubble. The effect of a separated second bubble arises due to the way the air was inserted into the tube for the following experiments. First, the tube is filled with fluid, then a three-way valve at the beginning of the tube is opened in order to insert the air bubble. After the valve is closed again and further fluid flows through the system, some air residue from inside the valve is drawn right behind the large air bubble. This process has been observed for all experiments with manually inserted air bubbles. State-of-the-art systems for a bubble detection are based on optic or ultrasonic sensors. For the DES, the sensor effect is different. Whereas with an optic or an ultrasonic sensor, the reflection between the two media (fluid and air) is detected, the DES measures the change in capacitance due to parasitic capacitances at the edge of the sensor. This parasitic capacitance is influenced by the medium inside the tube. For water, which has a relative permittivity  $\epsilon_r$  of 80 at  $20^\circ\text{C}$ , this secondary capacitance is large compared to an air bubble, due to the relative permittivity of air being 1. Hence, the small and usually negligible secondary capacitance of the DES is detectable, because it decreases by a factor of 80 due to the difference in media. For the measurement, the with fluid and air loaded tube was attached to



**Figure 4.31:** Zoom on air bubbles flowing from left to right inside the fabric-reinforced tube.

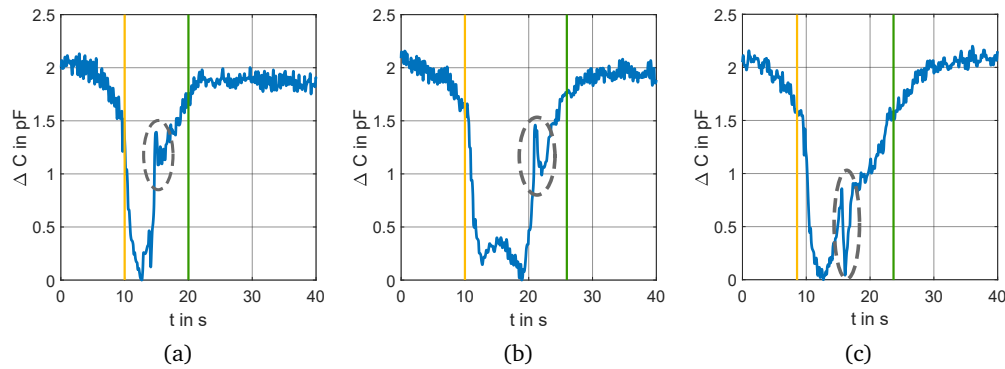


**Figure 4.32:** The bubbles wandering through the DES are detectable by drops in the capacitance for all three measurements.

the injector system, pumping fluid and air through the DES with the smallest possible flow rate of 0.1 ml/s. Due to the small flow rate and the throttle valve at the end of the tube open, no pressure develops inside the tube. Figure 4.32 shows three measurements of the capacitance change over time. The moment the air bubble enters the DES is marked with a yellow line in all three plots, whereas the green line indicates the small air bubble leaving the sensor. A distinct drop in capacitance is visible when the air bubble travels through the tube. After leaving the tube, the original capacitance is regained. Even the transition from the large bubble to the small bubble is clearly visible, marked with a grey dashed circle in the measurements in Figure 4.32. In order to eliminate a change in capacitance due to pressure in the tube, a laser sensor monitors the tube expansion during all experiments. However, no change in tube diameter is measured with the laser sensor, concluding that the change in capacitance is due to the mentioned secondary capacitance changing with the medium inside the tube.

#### 4.2.6 Discussion of Results

In this section, a pressure sensor based on dielectric elastomer technology has been introduced. It is developed in order to perform a nonintrusive pressure measurement inside a polymer tube for contrast fluid injection during a CT scan, MRI scan or an angiography. The tube expansion is characterized for pressures up to 62 bar. In order to design the sensor, a model for the capacitance change is developed. Furthermore, an analytic model for the tube expansion is employed in order to estimate the unknown mechanical properties of the fabric-reinforced tube material. Based on modeling and experiments, sensors with different geometries are designed, manufactured, attached to the polymer tube and characterized. The correlation between pressure and capacitance change is investigated for all manufactured sensor geometries. For constant pressure levels, viscoelastic behavior of the polymer tube is observed, which limits the sensor to specific conditions of the monitored system. However, for contrast fluid injection, the sensor

is feasible. Furthermore, mechanical stability of the sensor mounted onto the tube is increased by the design of a clamping mechanism. The clamp allows a reuse of the sensor for several polymer tubes. The possibility of performing a bubble detection with the DES is investigated and confirmed, which is an important feature for any medical injection device.

### **4.3 Summary and Future Work: High Pressure Sensors**

In this chapter, two advanced high pressure sensors based on dielectric elastomers are developed. An intrusive sensor, which enables pressure measurements up to 10 bar and a nonintrusive sensor for pressures up to 62 bar. The design process is similar for both sensors. After a characterization of the transmission barrier, the DES geometry is designed based on an analytical model. The system consisting of transmission barrier and DES is experimentally examined and validated. Both sensor concepts show remarkable results and outperform state-of-the-art DES in terms of pressure range. While the intrusive sensor shows comparable performance against a commercially available sensor, the nonintrusive sensor raises the bar of integrated pressure sensors concerning system size.

In future works, the pressure range of the intrusive sensor can be increased by the usage of a stiffer transmission barrier. Additionally, the size of the housing can be decreased by machined parts and the sensor connection is to be optimized. Suitable electronics which permit a faster and more exact capacitance measurement would improve the overall system further. Especially the integration of such electronics into the housing is an important step towards a final manufacturable prototype. For the nonintrusive sensor, a deeper investigation of the viscoelastic behavior is of interest. A modeling approach based on lumped elements, which includes viscoelastic behavior, would open up the ability to map these effects and identify the system pressure for arbitrary scenarios. In addition, the examination of larger pressure domains is of interest, in order to identify the limits of the developed sensor concept for further use cases besides medical injection, which is restricted to 83 bar. An important pursue would also be the development of suitable electronics for the capacitance measurement, which is low-cost, optimized for the measurement range and small in size.

Overall, DES for high pressure regimes are a promising field of application. Their advantages, such as high flexibility, small size and low-cost production can be harnessed ideally in this field. Further applications can surely be found, e.g., for the nonintrusive concept with larger tube systems, such as any kind of pressurized pipeline.



## **Part II**

# **Efficient Finite Element Modeling of Membrane Dielectric Elastomer Actuators**



## 5 Fundamentals

The development of numerical tools for computationally efficient simulation of dielectric elastomer actuators is an ongoing topic of research. In order to predict the actuation behavior of a DEA, a design assisted by numerical approach offers several advantages over simple graphical designs based on empirical data. As an example, if one is interested in optimizing an actuator geometry for a specific application, e.g., by changing the diameters of a cone-shaped DEA, different geometries must be manufactured and electromechanically characterized. Rules for parameter dependencies can be derived by means of simplified models, as done by Hau [61]. However, this approach still requires the need of manufacturing and testing several prototypes with different parameter values, resulting in a time-consuming and expensive design process. By means of a numerical simulation, an accurate prediction of the actuator performance is possible, making it possible to tailor an actuator to specific requirements. As a result, the optimized geometry can be directly manufactured in a (quasi) non-iterative way. Additionally, quantities which are hard to investigate experimentally, such as the electric field or mechanical strains and stresses, can be examined by using a simulation model. The evaluation of such quantities during the design stage can be used to prevent overloads on the material and, in turn, premature failure of the actuator.

Numerical simulation approaches for DEAs can be divided into two main categories, namely analytic models based on concentrated elements, and distributed models such as a Finite Element (FE) analysis. By means of concentrated elements approaches, fast predictions of the actuator performance are possible, including large deformations, viscoelasticity and electromechanical coupling. Detailed works based on such elements have been proposed by Rizzello [105, 106], Kaal [107] and further authors [108, 109]. However, since in these approaches the DE structure is represented as a combination of concentrated elements (springs, dampers), a calculation of global values only is possible. As a result, the overall force-displacement characteristic of an actuator can be effectively simulated, but not local stress and strain distributions. For distributed models, as provided by a FE analysis, the discretization of the whole structure into small elements allows a calculation of global as well as local quantities, such as stress and strain fields. The computational costs are larger compared to concentrated elements, but relevant quantities such as maximal stresses of the silicone film or the thickness change during actuation can be obtained. FE simulations of DEA structures have already been performed for stack actuators by Kaal [110], Park [111] or Wissler [112]. For membrane ac-

tuators, FE analysis have been introduced by several authors, e.g., Vertechy *et al.* [113] or Jabareen [114]. These membrane actuator simulations have in common that the electrodes are not discretized separately. Instead, the compound of silicone and electrodes is homogenized in a unique equivalent body. The reason for this modeling choice lies in the aspect ratio of a membrane structure, which has a large surface area in combination with a small thickness. For example, the aspect ratio for a DEA with a silicone film thickness of  $50\ \mu\text{m}$  and an area of  $1 \times 1\ \text{cm}^2$  can be calculated as 1:200. A discretization of the silicone film with 3D continuum elements would demand a large number of elements. For instance, a discretization of the thickness with 3 hexahedron elements with an aspect ratio of 1 the mesh consists of  $3 \times 600 \times 600 = 1.08 \cdot 10^6$  elements. By doing so, only the silicone is discretized, not the electrodes. As the example clearly shows, meshing a membrane structure with 3D continuum elements leads to a numerically expensive problem, which is not suitable for fast computations and resulting parameter studies.

This second Part of the thesis addresses the problem of inefficient FE modeling for DEAs. Two approaches are presented in order to reduce the computation time, one based on two-dimensional continuum elements and one based on three-dimensional membrane elements. In this chapter, the fundamentals for the simulation of membrane DEA structures are revisited, by defining all required mechanical and electrostatic quantities for continuous bodies. The field formulation for both approaches, i.e., the quasi-static mechanical and the electrostatic boundary value problem, are derived briefly. The electromechanical coupling, which interconnects both formulations when the DEA is electrically actuated, is also described by including a reduced form with approximations for incompressible capacitor-like structures. All FE implementations are performed in Comsol Multiphysics. The basics of FE modeling in Comsol is discussed in this chapter as well, in order to accomplish a basic understanding of the workflow, as well as to properly understand how the modules already implemented in Comsol can be manipulated to effectively simulate a DEA.

## 5.1 Continuum Mechanics

This section discusses the basic principles of continuum mechanics, which are necessary to understand the challenges of simulating a large, deformable structure, such as DEAs. In order not to affect the thesis readability, these theoretical considerations are kept as concise as possible. For further details on mathematical development the reader may refer to the textbook *Nonlinear Solid Mechanics* [103], with which this work shares the mathematical notation. All field formulations are represented in both tensor form and component-wise. Whereas the tensor notation offers a more compact notation, the implementation in Comsol Multiphysics is

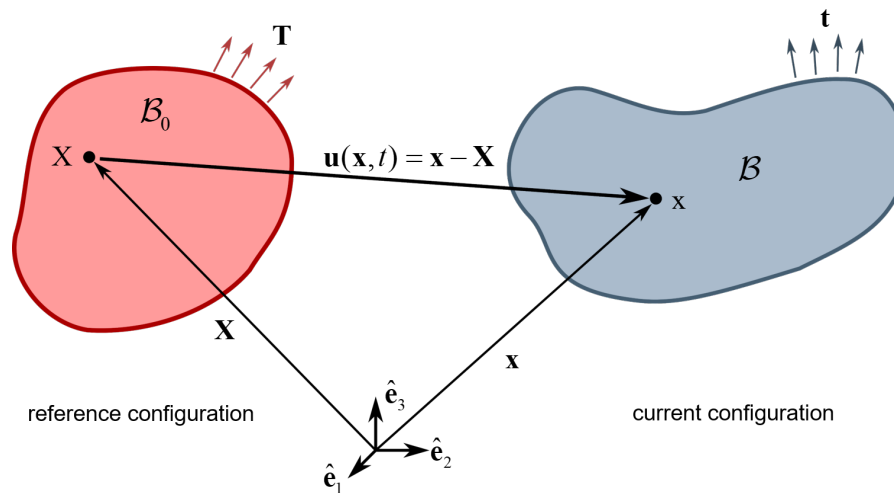


**Figure 5.1:** Configurations of a continuous body with a representation of the displacement of one point.

performed component-wise. For the component representation, the Einstein sum convention is assumed to hold.

In order to simulate a DEA, a mechanical field formulation is required. A DEA undergoes considerable deformations during actuation. Hence, the deformation of the continuous body must be taken into account, including resulting strains and stresses. To achieve this goal, the theory of continuum mechanics can be used. Continuum mechanics studies the motion of deformable bodies under external loads. In here, materials are modeled as a continuous mass, rather than as discrete particles. An important aspect of continuum mechanics is the difference between configurations. While a body deforms, its configuration changes (e.g., area, velocity, density). In order to track those changes, two configurations are introduced in Figure 5.1. The reference configuration in red shows a body  $\mathcal{B}_0$  at time  $t_0$ , with a point  $X$  defined by the vector  $\mathbf{X}$  in the depicted coordinate system. In contrast, the current configuration shows the deformed and translated body  $\mathcal{B}$  at time  $t$ , where the point  $X$  has shifted to  $x$ . Again, the vector  $\mathbf{x}$  is defined in the depicted coordinate system.

The displacement of every point is described by the displacement field  $\mathbf{u}(\mathbf{x}, t) = \mathbf{x} - \mathbf{X}$ . In order to transform vectors among the two configurations, the deformation gradient  $\mathbf{F}$  is introduced, defined as

$$d\mathbf{x} = \mathbf{F} d\mathbf{X} \quad \text{or} \quad dx_i = F_{iA} dX_A. \quad (5.1)$$

As equation (5.1) states, the deformation gradient maps material (undeformed) line elements  $d\mathbf{X}$  to spatial (deformed) line elements  $d\mathbf{x}$ . Note that both line elements have different indices.

The indices  $\{A, B, C\}$  describe the reference configuration, whereas the indices  $\{i, j, k\}$  describe the current configuration. The deformation gradient is crucial in continuum mechanics due to its nature of transforming quantities between both configurations. This is true not only for the mechanical domain, but also for the electrical one, thus it can be used to transform quantities such as electric field as well. The existence of different configurations for continuous bodies shows, that there is no scalar representation of quantities such as strains, acting forces and stresses. Depending on which configuration is examined, line, surface and volume elements change, and with these elements the forces that act on them. Hence, strains and stresses must be defined for both configurations. From here on, the most important strain and stress measures are defined, in order to formulate the mechanical boundary value problem.

A common strain measure for FE analysis is the Green-Lagrange strain tensor  $\mathbf{E}^{GL}$ , which is defined as

$$\mathbf{E}^{GL} = \frac{1}{2} (\mathbf{C} - \mathbf{I}) \quad \text{or} \quad E_{AB}^{GL} = (C_{AB} - \delta_{AB}), \quad (5.2)$$

where  $\mathbf{C} = \mathbf{F}^T \mathbf{F}$  describes the right Cauchy-Green deformation tensor,  $\mathbf{I}$  the identity tensor and  $\delta$  the Kronecker Delta. It describes deformations in the reference configuration, as one can see by its indices.

A force increment  $d\mathbf{f}$ , which acts onto a surface increment, produces a mechanical stress vector. The resulting stress is based on whether the surface increment in the reference frame  $d\mathbf{S}$  or the increment in the current frame  $d\mathbf{s}$  is considered,

$$d\mathbf{f} = \mathbf{T} d\mathbf{S} = \mathbf{t} d\mathbf{s}. \quad (5.3)$$

The resulting stress vectors  $\mathbf{T}$  and  $\mathbf{t}$  are depicted in Figure 5.1. These represent important quantities for determining the mechanical boundary conditions. Based on those stress vectors, the Cauchy stress tensor  $\boldsymbol{\sigma}$  for the current configuration and the first Piola-Kirchhoff stress tensor  $\mathbf{P}$  for the reference configuration can be expressed as

$$\begin{aligned} \mathbf{t} &= \boldsymbol{\sigma} \hat{\mathbf{n}} & \text{or} & & t_i &= \sigma_{ij} n_j, \\ \mathbf{T} &= \mathbf{P} \hat{\mathbf{N}} & \text{or} & & T_i &= \mathbf{P}_{iB} N_B, \end{aligned} \quad (5.4)$$

with  $\hat{\mathbf{n}}$  and  $\hat{\mathbf{N}}$  being the normal vectors in current and in reference configuration, respectively. A transformation between both stress tensors is defined by

$$\mathbf{P} = J \boldsymbol{\sigma} \mathbf{F}^T \quad \text{or} \quad P_{iA} = J \sigma_{ij} F_{Aj}^{-1}, \quad (5.5)$$

with  $J = \det \mathbf{F}$  being the local volume ratio. For an incompressible body, the following holds

$$J = 1. \quad (5.6)$$

For a FE implementation, a conjugate stress measure (see [115] for more details) is desired, corresponding to the Green-Lagrange strain tensor  $\mathbf{E}^{GL}$ . The second Piola-Kirchhoff stress  $\mathbf{S}$  is the conjugated stress to the Green-Lagrange strain tensor and is defined as  $\mathbf{S} = \mathbf{F}^{-1} \mathbf{P}$ , yielding in combination with equation (5.5) the transformation to the current configuration to

$$\mathbf{S} = J \mathbf{F}^{-1} \boldsymbol{\sigma} \mathbf{F}^T \quad \text{or} \quad S_{AB} = J F_{Aj}^{-1} F_{Bj}^{-1}. \quad (5.7)$$

This transformation is crucial in this work, because the electromechanical coupling which is described in detail in Section 5.2, is defined by means of Cauchy stresses. In order to use this result in a FEM framework, this transformation rule is applied.

The mechanical boundary value problem arises from the balance of momentum, which is also known as Newton's second law. It states that the linear momentum  $\mathbf{l}$  of a material body changes due to force  $\mathbf{f}$  applied to it. Integration over the whole body and vector calculus transforms this relationship to the representation

$$\text{Div}(\mathbf{FS}) = \rho_0 \ddot{\mathbf{x}} \quad \text{or} \quad \frac{\partial}{\partial X_A} (F_{iA} S_{AB}) = \rho_0 \ddot{x}_i, \quad (5.8)$$

with the material divergence operator  $\text{Div}(\bullet)$  and the density  $\rho_0$ . In this thesis, equation (5.8) is simplified by neglecting inertial effects, implying that the right hand side reduces to  $\rho_0 \ddot{\mathbf{x}} = 0$ . In order to solve this partial differential equation (PDE), boundary conditions must be defined. There are two types of boundary conditions for the quasi-static formulation, shown in Figure 5.2 with a red and a blue line. A Dirichlet boundary condition on  $\partial \mathcal{B}_0^U$ , which describes

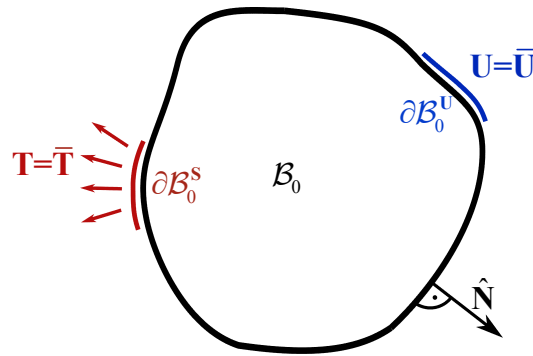


**Figure 5.2:** Mechanical boundary value problem in the reference configuration.

external displacements  $\bar{\mathbf{U}}$ , and a Neumann boundary on  $\partial\mathcal{B}_0^S$ , which describes external stresses  $\bar{\mathbf{T}}$  in normal direction. Figure 5.1 shows these boundary conditions acting onto the body  $\mathcal{B}_0$  in the reference configuration, with the reference normal vector  $\hat{\mathbf{N}}$ . The complete boundary value problem (BVP) results to

$$\text{Div}(\mathbf{FS}) = \mathbf{0} \quad \text{in } \mathcal{B}_0, \quad (5.9)$$

$$(\mathbf{FS}) \cdot \hat{\mathbf{N}} = \bar{\mathbf{T}} \quad \text{in } \partial\mathcal{B}_0^S, \quad (5.10)$$

$$\mathbf{U} = \bar{\mathbf{U}} \quad \text{in } \partial\mathcal{B}_0^U \quad (5.11)$$

Note that there is no need for any initial values, because the problem is reduced to its quasi-static form, i.e., it is time-invariant. This field formulation is used by Comsol for modeling mechanical problems which include large deformations. Silicone film and electrode of the DEA are modeled based on these equations, with the addition of hyperelasticity for the stress-strain relationship and viscoelasticity, which will be discussed in detail in Chapter 6.

## 5.2 Electrostatics for Continuous Bodies

The deformation that a DEA undergoes during actuation is due to the application of an electric voltage. Therefore, a FE modeling approach does not only include mechanical, but also electric fields. The movement and the charging time of a DEA are in a range in which the electrostatics can be approximated to electrostatics. In this case, any time derivatives of the Maxwell equations vanish, as well as any contributions concerning magnetic fields. To formulate the electrostatic boundary value problem, a potential formulation is common, as derived in [116, Chapter 4]. Here, the electric potential  $\varphi$  results from combining the Gauss law,

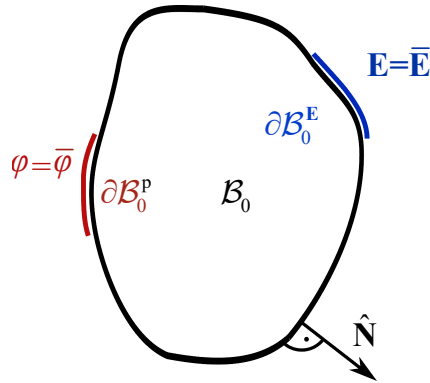


**Figure 5.3:** Electrostatic boundary value problem in the reference configuration.

$$\nabla \cdot \mathbf{D} = \varrho_0, \quad (5.12)$$

with the material relationship between the electric field  $\mathbf{E}$  and the dielectric displacement  $\mathbf{D}$ ,

$$\mathbf{D} = \varepsilon_0 \varepsilon_r \mathbf{E}, \quad (5.13)$$

and the electric potential  $\varphi$  defined as

$$\mathbf{E} = -\nabla \varphi. \quad (5.14)$$

The quantities  $\varrho_0$  and  $\nabla$  being the charge density and the Nabla operator, respectively. Combining these results, the electric potential calculates by solving the partial differential equation

$$\Delta \varphi = -\frac{\varrho_0}{\varepsilon_0 \varepsilon_r}, \quad (5.15)$$

with  $\Delta$  being the Laplace operator. This equation holds for electrostatic fields with homogeneous dielectrics. Note that equation (5.14) arises from the fact, that in electrostatics, the electric field is curl-free. Any curl-free vector field can be expressed as the gradient of a scalar field.

In a FE formulation, equation (5.15) is solved and the electric field results from equation (5.14). However, in order to be consistent with the continuum mechanics in Section 5.1, the electric BVP is defined as a field formulation as well. Similar to the mechanical BVP, boundary conditions must be defined in order to allow a unique solution. Similar to the mechanical boundary conditions, there are Dirichlet boundaries  $\partial \mathcal{B}_0^p$ , where a constant potential  $\bar{\varphi}$  is defined, and Neumann boundaries  $\partial \mathcal{B}_0^E$ , where the electric field  $\bar{\mathbf{E}}$  is defined, as shown in Figure 5.3. The complete BVP results then to

$$\text{Div } \mathbf{E} = \frac{\rho_0}{\varepsilon_0 \varepsilon_r} \quad \text{in } \mathcal{B}_0, \quad (5.16)$$

$$\mathbf{E} = -\nabla \varphi \quad \text{in } \mathcal{B}_0, \quad (5.17)$$

$$\varphi = \bar{\varphi} \quad \text{in } \partial \mathcal{B}_0^p, \quad (5.18)$$

$$\frac{\partial \varphi}{\partial \hat{\mathbf{N}}} = -\hat{\mathbf{E}} \quad \text{in } \partial \mathcal{B}_0^E \quad (5.19)$$

Also here, there is no need for initial values due to the formulation being quasi-static. The electrodes of the DEA are represented by a constant potential boundary condition, in order to simulate the high voltage source acting on the electrodes. Note that this formulation is derived in the reference configuration, in order to be consistent with the mechanical formulation. Hence,  $\mathbf{E}$  is the electric field vector in the reference configuration.

The electromechanical coupling between the mechanical and the electrical field formulation is performed via boundary conditions. Based on the Maxwell equations, the Maxwell stress tensor  $\boldsymbol{\sigma}^{MW}$  is derived as

$$\boldsymbol{\sigma}^{MW} = \varepsilon_0 \varepsilon_r \left( \mathbf{e} \otimes \mathbf{e} - \frac{1}{2} \mathbf{e} \cdot \mathbf{e} \mathbf{I} \right) \quad \text{or} \quad \sigma_{ij}^{MW} = \varepsilon_0 \varepsilon_r \left( e_i e_j - \frac{1}{2} \delta_{ij} e^2 \right), \quad (5.20)$$

where  $\otimes$  denotes the dyadic product,  $\mathbf{e}$  the electric field vector in the current configuration and  $\mathbf{I}$  the unity tensor [117]. The Maxwell stress tensor is defined in the current configuration, therefore it is calculated with the electric field in the current configuration. In order to transform the electric field to the current configuration, the crucial relation

$$\mathbf{e} = \mathbf{F}^T \mathbf{E} \quad (5.21)$$

holds [114, 118], which once again shows the importance of the deformation gradient  $\mathbf{F}$ , which translates between both configurations. In order to receive the Maxwell stress tensor in the reference configuration, equation (5.7) yields

$$\mathbf{S}^{MW} = J\mathbf{F}^{-1}\boldsymbol{\sigma}^{MW}\mathbf{F}^T \quad \text{or} \quad S_{AB}^{MW} = JF_{Ai}^{-1}\sigma_{ij}^{MW}F_{Bj}^{-1}. \quad (5.22)$$

For the coupling, the Maxwell stress is inserted as a mechanical boundary condition as stated in equation (5.10). Simultaneously, the electric field formulation changes due to the deformation gradient acting on the electric field in equation (5.21). More details on how the coupling is implemented in Comsol are provided in Section 6.3.

### 5.3 Finite Element Modeling with Comsol Multiphysics

Comsol offers the possibility of implementing multi-physical problems in a FE environment based on physical equations. This means that the user input is based on the PDEs which are the physical representation of a given problem. Hence, equations such as the components of the electric field or the second Piola-Kirchhoff stress tensor can be modified component-wise. Comsol offers different modules with pre-implemented physical interfaces. In this thesis, the Nonlinear Mechanics Module for mechanical deformation of the DEA and the AC/DC module for electrostatic calculations are used. Apart from that, standard ODE and PDE solvers are available, in which the user is able to implement its own equations. Comsol offers its own implemented coupling mechanisms, which offer interconnections between the modules. However, in this thesis, different electromechanical coupling implementations are compared. In order to do that, the coupling is implemented by hand, without using the Comsol-internal coupling. The reason lies in the inability to observe all variables of the Comsol-internal coupling, which makes it overly complicated to monitor and, if necessary, to debug.

To perform simulations in Comsol, the user needs to implement the geometry, boundary conditions, form and size of the mesh and its elements. At the same time, Comsol handles automatically the mathematical problems such as building a weak formulation and solving the set of linear equations. In order to confirm numerical results which do not depend on the mesh size, convergence studies are performed, which monitor specific quantities over the number of mesh elements. For all FE models in this thesis, such convergence studies are performed. As an example, the convergence study of a two-dimensional FE model of a DEA, which is developed in Chapter 6, is shown in Figure 5.4. Two kind of quantities are examined, i.e., global quantities, such as reaction forces and system energies, and local field quantities at one spe-

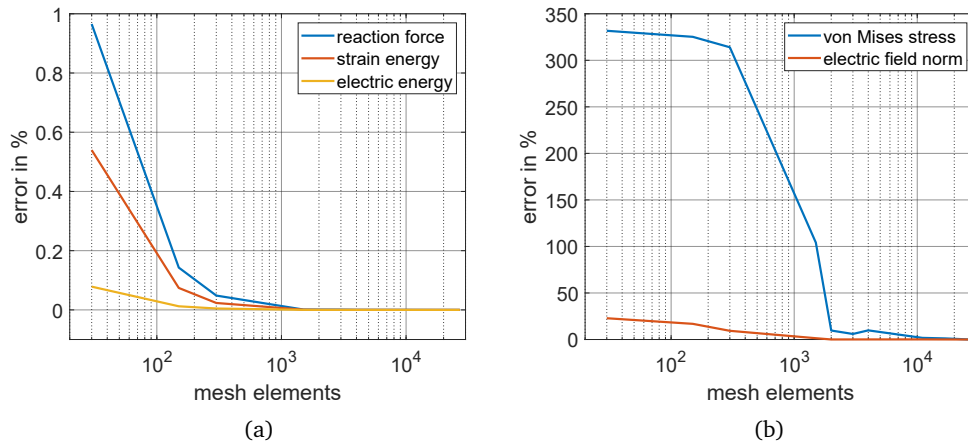


**Figure 5.4:** Exemplary convergence study for a two-dimensional FE DEA model, global values (a) and local values evaluated at a distinct coordinate (b).

cific point, such as stresses and the electric field norm. Figure 5.4 (a) shows the convergence of three global values over the number of mesh elements, namely the reaction force of a DEA when stretched to 50 %, the total strain energy of the model and the total electric energy of the model. As one can see, the error converges for a small number of elements, starting with an error under 1 % for the coarsest discretization. This fast convergence is due to the averaging nature of global quantities. In order to show convergence for local quantities, Figure 5.4 (b) shows the convergence of the von Mises stress and the norm of the electric field at one specific coordinate of the model, which is marked by a red dot in Figure 6.2 (b), right hand side. Both local quantities require a larger number of mesh elements in order to reach convergence. Hence, the number of elements for every model is determined by a convergence study which includes global and local quantities.

Unless differently stated, the simulations performed in this thesis use the following parameters. All geometries are discretized with quadratic serendipity elements. Simulations are performed by neglecting inertial effects, and considering viscoelastic behavior, leading to a dynamic model. The Comsol built-in direct solver MUMPS (MULTifrontal Massively Parallel Sparse) direct solver is chosen, with a nonlinear Newton-Raphson method for solving the system of equations. The essential solver parameters are chosen as follows: initial damping factor of  $10^{-4}$ , maximum number of iterations of 50 and a tolerance factor of  $10^{-2}$ . All models have been solved on an Intel i7-4770 processor with 32 GB DDR3 random access memory (RAM), which is stated for interpreting the given model solution times.

Based on the theory described in this chapter, and the process of modeling with Comsol Multiphysics, multiple FE models are developed in the subsequent chapters, first based on a two-

dimensional continuum formulation in Chapter 6, followed by a three-dimensional membrane formulation in Chapter 7.



## 6 Finite Element Modeling of Plane Strain Geometries

The FE modeling described in this chapter is based on the main idea of reducing a DEA with a specific geometry to a two-dimensional model. The remarkably high reduction in computational cost provided by this reduction method allows a separate discretization of the electrodes, as well. Such a model can be used in order to investigate the interaction between electrode and silicone and arising stresses or electric field distributions in this region. Figure 2.7 shows two characteristic force-displacement curves of a COP-DEA. Key features are the nonlinear material behavior and hysteretic effects, with and without applied voltage. The goal of this chapter is the development of a two-dimensional continuum formulation for the simulation of a DEA, which maps these features. Therefore, it includes large deformations, hyperelasticity, viscoelasticity and electromechanical coupling. First, the exact procedure to reduce the model of a DEA to a two-dimensional model is discussed, followed by a brief examination on how the material modeling and viscoelastic behavior is implemented. Subsequently, different approaches on how to implement the electromechanical coupling are discussed. The resulting FE model is evaluated in order to identify material parameters in accordance to performed experiments and the model is validated by further simulations and corresponding experiments. Finally, the model structure with separately discretized electrodes is harnessed by simulating different electrode geometry variations.

### 6.1 Simplifications for Two-Dimensional Continuum Modeling

The challenge of modeling a DEA with a three-dimensional FE formulation lies in the discretization of a membrane structure with continuum elements, as discussed in Chapter 5. The aspect ratio of a membrane generates an extremely large number of required mesh elements, leading to large computation times of the resulting model. A sketch of a DEA strip is shown in Figure 6.1, meshed with hexahedron three-dimensional continuum elements. Due to the dimensions and a discretization of the membrane thickness with 4 elements, the number of elements results to  $80 \cdot 10^6$ . A computation of this structure with Comsol Multiphysics does not converge for a small deformation of  $100 \mu\text{m}$  (computation canceled after 6 hours, due to memory buffer overflow). In order to avoid this clear disadvantage and build a computing model, the reduction to a two-dimensional model for specific membrane DEA geometries is discussed. Figure 6.2 (a) shows an in-plane deflected strip (SIP) DEA with the dimensions

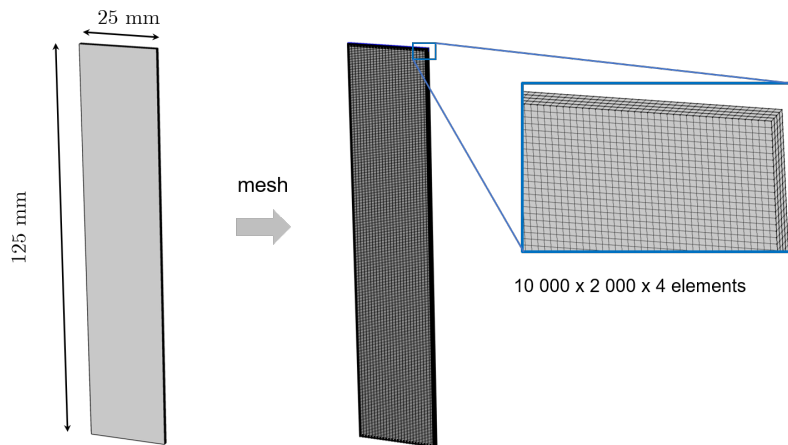


**Figure 6.1:** In order to mesh the silicone film for a standardized 1:5 sample with hexahedron elements, 80 million elements are required, yielding tremendous computational cost.

25 mm  $\times$  125 mm, in its undeflected state and with a maximal stretch of 50 %. The thickness of the sandwich structure equals  $d_s = 50 \mu\text{m}$  for the silicone and  $d_e = 5 \mu\text{m}$  for each electrode, resulting in an overall initial thickness of  $d_0 = 60 \mu\text{m}$ . Based on the standards of Carpi *et al.* [33], this sample size with a ratio of 1:5 is suited for pure shear approximations. In a pure shear tensile test, the necking of the upper and lower edges, as visible in Figure 6.2, are neglected. In other words, pure shear describes the three-dimensional homogeneous flattening of the membrane, without any rotational influence. The possibility of neglecting any necking leads to the simplification of a plane strain state in the  $y$ -direction according to Figure 6.2. More concretely, only one slice of the membrane is simulated, namely the  $x$ - $z$ -plane, as shown in Figure 6.2 (b).

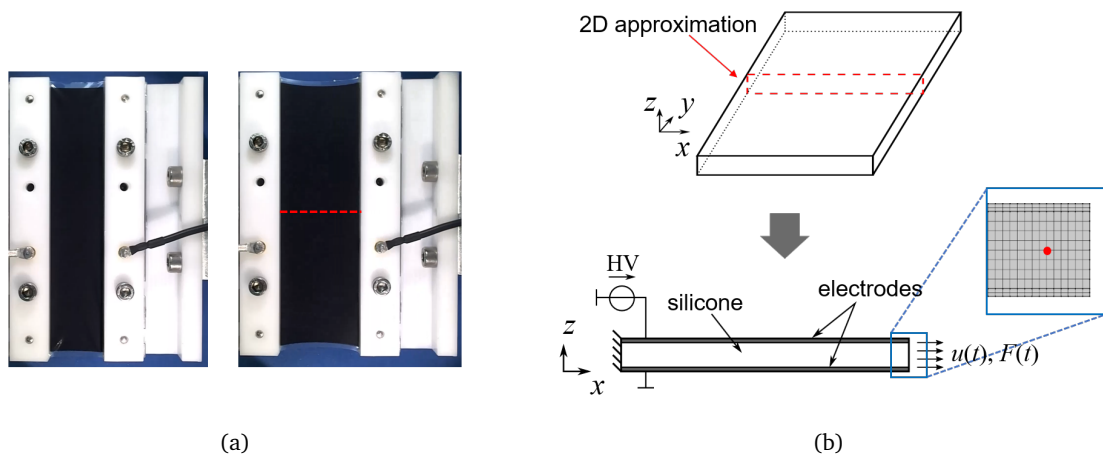


**Figure 6.2:** The standardized pure shear sample without pre-stretch and with the maximal applied stretch of 50 % (a), and the reduction to a two-dimensional model (b).

The two-dimensional model consists of three layers, one for the silicone and two for the compliant electrodes. Thus, the influence of the electrodes onto the actuator performance can be studied without the need of homogenizing silicone and electrode in one combined layer. In this case, a discretization with two-dimensional continuum elements is much more feasible on the numerical viewpoint, e.g., for the model in Figure 6.2 (b), a discretization of silicone with 8 elements and electrodes with 2 elements, the overall element count would be around 300 000. Hence, the number of elements decreases by a factor of approximately 270. The limitation of this model is the fact that necking at the edges is neglected. While this assumption is legit for plane strain samples, with changing aspect ratios towards a uniaxial sample (ratio 5:1), the necking is an important part of the deformation and cannot be neglected anymore. However, this chapter is restricted to the in Figure 6.2 depicted sample, where the plane strain approximation is feasible.

## 6.2 Hyperelasticity and Viscoelasticity

One of the main features of DEAs is their compliance. Large deformations up to 200 % are possible for the material [10], and during actuation stretches around 60 % arise [11]. A linear-elastic material behavior is not expected for such stretches. In fact, the nonlinear material behavior of rubber-like materials is well studied [119]. In order to describe large deformations for rubber-like materials, hyperelastic material models are used. Despite the concept of hyperelasticity has been deeply described in literature [103], the required background is discussed in this thesis. Based on the free strain-energy density  $\psi_s$  of the material, the stress can be calculated by differentiating the free strain-energy density with respect to the strain. Due to the existence of different stress and strain measures, a suitable combination of stress and strain must be chosen, in such ways that they are energetically conjugates (for more details to conjugated strain and stress tensors, see [103, Chapter 4.4]). One such pair is the second Piola-Kirchhoff stress  $\mathbf{S}$  and the Green-Lagrange strain  $\mathbf{E}^{GL}$ . Hence,  $\mathbf{S}$  is calculated as

$$\mathbf{S} = \frac{\partial \psi_s}{\partial \mathbf{E}^{GL}}. \quad (6.1)$$

This correlation between stress and strain is the most general one, depending on the free strain-energy density of the system. There are many hyperelastic material models for representing the free strain-energy density, such as Neo-Hooke, Mooney-Rivlin, Saint Venant-Kirchhoff or Ogden (for more details, see [106, Chapter 3.3]). The material model used in this work is the Yeoh model, which defines the free strain-energy density as

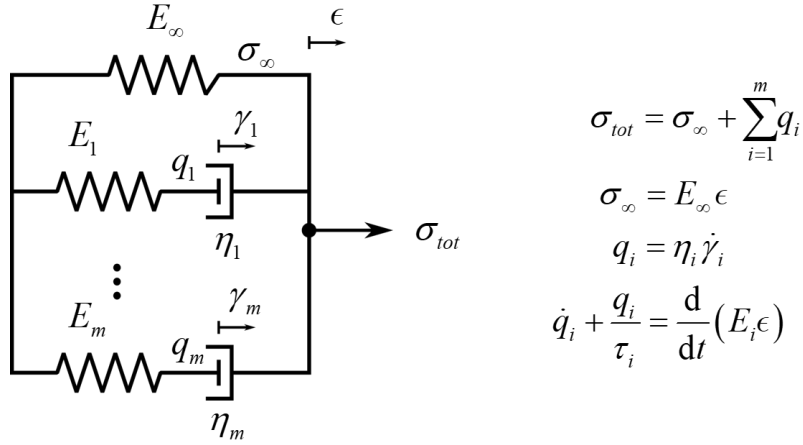


**Figure 6.3:** A one-dimensional viscoelastic lumped model and its governing equations.

$$\psi_s(I_1) = \sum_{i=1}^3 C_i (I_1 - 3)^i, \quad (6.2)$$

where  $I_1$  describes the first invariant of the Cauchy-Green Deformation tensor  $\mathbf{C}$ . The material parameters  $C_i$  must be identified for the investigated material. The Yeoh model is chosen in this work, because it is suitable for large deformations characteristics of silicone [119]. By using this model, the nonlinear-elastic material behavior is mapped. However, the curves of a DEA, as shown in Figure 2.7, show also rate-dependent behavior. In order to implement viscoelastic material behavior into the FE formulation as well, a viscoelastic model based on lumped elements as presented in [120] is chosen. Figure 6.3 shows the model, which consists of a nonlinear spring with stiffness  $E_\infty$  and  $m$  Maxwell branches with stiffness  $E_i$  and damper coefficient  $\eta_i$ . The nonlinear spring represents the hyperelastic material response, whereas the linear Maxwell branches represent viscoelasticity. When loaded, each Maxwell branch exhibits a non-equilibrium stress  $q_i$ , which is added to the overall stress  $\sigma_{tot}$ . Those stresses describe the distance to the equilibrium state and are released over time, until the equilibrium stress  $\sigma_\infty$  is reached. For each stress  $q_i$ , the ordinary differential equation

$$\dot{q}_i + \frac{q_i}{\tau_i} = \frac{d}{dt} (E_i \epsilon) \quad (6.3)$$

holds, with  $\tau_i = \eta_i/E_i$  being the relaxation time of the  $i^{th}$  dashpot. This model can be extended to three dimensions, leading to the representation

$$\dot{\mathbf{Q}}_i + \frac{\mathbf{Q}_i}{\tau_i} = \frac{d}{dt} (\beta_i \mathbf{S}_{iso}^\infty), \quad (6.4)$$

with the non-equilibrium stress tensor  $\mathbf{Q}_i$ , which is a second Piola-Kirchhoff type stress, the isochoric second Piola-Kirchhoff stress  $\mathbf{S}_{iso}^\infty$  and the strain-energy factor  $\beta_i$ . For more details on the derivation of these equations, see [120]. In order to implement equation (6.4) in a numerically efficient way, a state transformation is performed in order to cancel the time derivative. The overstresses  $\mathbf{Q}_i$  are transformed to an additional stress tensor  $\underline{\mathbf{Q}}_i$  by applying

$$\mathbf{Q}_i = \beta_i \mathbf{S}_{iso}^\infty - \underline{\mathbf{Q}}_i. \quad (6.5)$$

This transformation leads to an alternative presentation of equation (6.4) as

$$\tau_i \dot{\underline{\mathbf{Q}}}_i + \underline{\mathbf{Q}}_i = \beta_i \mathbf{S}_{iso}^\infty, \quad (6.6)$$

canceling the time derivative on the right-hand side. The number of Maxwell branches which are needed to map the material behavior is dependent on the applied mechanical and electrical frequencies and therefore not unique. In this thesis, only one branch is considered. However, the following simulation results fit the experimental data sufficiently, which is why no further branches have been implemented. The inhomogeneous ordinary differential equation (6.4) is implemented into the ODE module in Comsol Multiphysics, which solves the equation on the whole domain, and the resulting stress tensor  $\mathbf{Q}_i$  is added to the second Piola-Kirchhoff stress  $\mathbf{S}$  of the hyperelastic material model. Thus, viscoelasticity and hyperelasticity are implemented into the two-dimensional FE model. In order to simulate a DEA, the coupling between the electrostatic and the mechanical BVP must be performed. The next section derives different approaches for this electromechanical coupling.

### 6.3 Electromechanical Coupling

There are different ways of realizing the electromechanical coupling. In this section, three different approaches are discussed and compared. First, the general way of coupling mechanics and electrostatics is described by the three-dimensional Maxwell stress tensor in equation (5.20). Secondly, a derivation for inducing external stresses onto the membrane without cal-

culating the Maxwell stress tensor is introduced, which is based on simplifications concerning the electric field. Finally, a coupling approach via an expansion of the free strain-energy density is introduced, which results in a coupling without applying any boundary conditions onto the membrane surface.

In order to implement the Maxwell stress tensor, the procedure is as follows. The electric field  $\mathbf{E}$  is calculated by Comsol in the reference configuration. However, the Maxwell stress tensor is defined in the current configuration, as stated in equation (5.20). The electric field computed by Comsol is transformed to the current configuration following the transformation rule (5.21) and then inserted into the Maxwell stress tensor. In order to apply the stress boundary condition onto the surface between silicone and electrode, the Maxwell stress tensor  $\boldsymbol{\sigma}^{MW}$  is converted to the reference configuration by means of equation (5.22), yielding the Maxwell stress tensor in the reference configuration  $\mathbf{S}^{MW}$ . The Maxwell stress tensor is then added to the second Piola-Kirchhoff stress tensor  $\mathbf{S}$ , which is computed in equation (6.1).

The second implementation of the Maxwell stress tensor is the reduction to a reduced form with only one component in  $z$ -direction, thus, normal to the membrane surface. It is derived by Pelrine *et al.* [37] for incompressible, deformable parallel plate capacitors. The electric field is approximated with only one component  $e_z$  between the electrodes, neglecting all fringe fields. In this case, the Maxwell stress calculates in correspondence to equation (2.2) to

$$\sigma_{zz}^{MW} = -\varepsilon_0 \varepsilon_r e_z^2. \quad (6.7)$$

Inserting the one component electric field into the Maxwell stress tensor (5.20) results into a further representation,

$$\boldsymbol{\sigma}^{MW} = \frac{1}{2} \varepsilon_0 \varepsilon_r e_z^2 \begin{pmatrix} 1 & 0 & 0 \\ 0 & 1 & 0 \\ 0 & 0 & -1 \end{pmatrix}, \quad (6.8)$$

which, other than equation (6.7), contains three stress components for the coupling. However, as shown by Kaal [110, Chapter 2.5], both stress states lead to the same deformation when inserted into the Hooke's law for isotropic continuous materials. Due to this correlation, only one of the two representations is implemented for the comparison of the proposed coupling methods, more precisely the representation in equation (6.7).

The third method of coupling the electric and the mechanic BVP is based on the free energy density. Based on the work from Suo [121], the free strain-energy density, from which the stresses are derived (equation (6.1)), can be expanded by an electrical term. This term represents the energy stored in a dielectric due to an electrostatic field. The stored electric energy density of a deformed body  $\tilde{\psi}_e$  is computed as

$$\tilde{\psi}_e = -\frac{\varepsilon_0 \varepsilon_r}{2} \mathbf{e}^T \mathbf{e} = -\frac{\varepsilon_0 \varepsilon_r}{2} \mathbf{E}^T \mathbf{F}^{-1} \mathbf{F}^{-T} \mathbf{E} = -\frac{\varepsilon_0 \varepsilon_r}{2} \mathbf{E}^T \mathbf{C}^{-1} \mathbf{E}. \quad (6.9)$$

Note that this equation describes the deformed body, while the free strain-energy density in Comsol describes the undeformed body. In order to compensate for the deformation, the volume ratio  $J$  is added to the energy density, in order to compensate for arising volumetric changes, yielding

$$\psi_e = -\frac{\varepsilon_0 \varepsilon_r}{2} J \mathbf{E}^T \mathbf{C}^{-1} \mathbf{E}. \quad (6.10)$$

This energy is added to the free strain-energy density, yielding  $\psi = \psi_s + \psi_e$ , out of which the resulting stresses are calculated as stated in equation (6.1).

In order to justify the expansion of the free-energy density in terms of the electric field, following qualitative considerations are performed. Including the electromechanical coupling, thermodynamics states the change of the free strain-energy density as

$$d\psi(\lambda_i, \mathbf{D}) = \sum_{i=1}^3 \sigma_i d\lambda_i + \mathbf{E} d\mathbf{D}, \quad (6.11)$$

with  $\sigma_i$ ,  $\lambda_i$ ,  $\mathbf{E}$  and  $\mathbf{D}$  being stress, stretch, electric field and electric displacement, respectively [121]. Hence, the free strain-energy depends on the stretches  $\lambda_i$  and the electric displacement  $\mathbf{D}$ , which prohibits a formulation of the electric energy density in terms of the electric field. Therefore, a Legendre transformation is performed, which introduces an alternative representation of the strain-energy as

$$\Gamma(\lambda_i, \mathbf{E}) = \psi - \mathbf{E} \mathbf{D}. \quad (6.12)$$

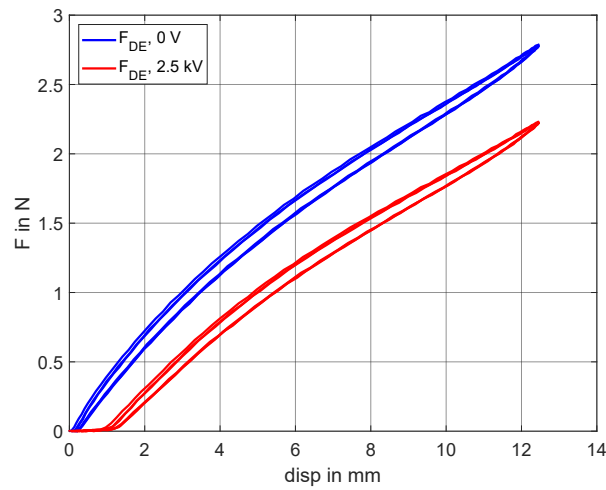


**Figure 6.4:** Experimental data of the SIP DEA, including silicone and electrodes, with and without applied voltage.

Based on this representation, equation (6.11) can be written as follows

$$d\Gamma(\lambda_i, \mathbf{E}) = \sum_{i=1}^3 \sigma_i d\lambda_i - \mathbf{D} d\mathbf{E}, \quad (6.13)$$

which now allows the derivation of electrical quantities by deriving the energy after the electric field  $\mathbf{E}$ .

Before comparing all three coupling variations, a two-dimensional model as described in Section 6.1 is implemented in Comsol, which includes all the aforementioned features, namely hyperelasticity and viscoelasticity. The model parameters for silicone and electrodes must be determined by comparison of simulations with experiments.

## 6.4 Parameter Identification and Model Validation

Within the identification process, the material parameters of silicone film and electrode material are determined in order to match the force-displacement behavior of the actuator. Figure 6.4 shows the measured force-displacement curves for the in this chapter described SIP DEA with dimensions of 25 mm × 125 mm. The parameters to be determined are the hyperelastic material parameters  $C_1$ ,  $C_2$  and  $C_3$ , as well as the viscoelasticity parameters  $\tau$  and  $\beta$ . The identification process is divided into two steps, as follows:

1. The hyperelastic material parameters are approximated by fitting an analytical pure-shear model onto experimental data. A similar procedure is described in [122].
2. Starting with the approximated parameters from step 1, a numerical optimization process is performed with a FE model, where the parameters  $C_i$  are fine tuned. First, no time-dependency is implemented into the model. Subsequently, the viscoelasticity parameters  $\tau$  and  $\beta$  are determined by expanding the FE model by viscoelasticity and fitting the viscoelastic parameters onto experimental data.

Both steps are discussed in detail below.

The analytical model for approximating the material parameters is derived by combining the Yeoh free strain-energy density model (6.2) with a more general version of equation (6.1), which combines stresses and strains without consideration of different configurations, yielding a simplified one-dimensional stress  $\sigma_1$  as

$$\sigma_1 = \frac{\partial \psi_Y(I_1)}{\partial \lambda_1}, \quad (6.14)$$

with  $\lambda_1$  being the principal stretch in the direction of deformation (here the  $x$ -direction in Figure 6.2 (b)) and  $I_1$  being the first invariant of the right Cauchy-Green tensor  $\mathbf{C}$ . It is defined as

$$I_1 = \lambda_1^2 + \lambda_2^2 + \lambda_3^2. \quad (6.15)$$

In case of incompressibility ( $\lambda_1 \lambda_2 \lambda_3 = 1$ ) and for pure shear geometries ( $\lambda_2 = 1$ ), it can be simplified to

$$I_1 = \lambda_1^2 + 1 + \lambda_1^{-2}. \quad (6.16)$$

Inserting this result into equation (6.14), the one-dimensional stress  $\sigma_1$  is calculated as

$$\sigma_1 = \frac{\partial \psi_Y}{\partial \lambda_1} = \frac{\partial \psi_Y}{\partial I_1} \frac{\partial I_1}{\partial \lambda_1} = \sum_{i=1}^3 C_i i (\lambda_1^2 + \lambda_1^{-2} - 2)^{i-1} (2\lambda_1 - 2\lambda_1^{-3}). \quad (6.17)$$

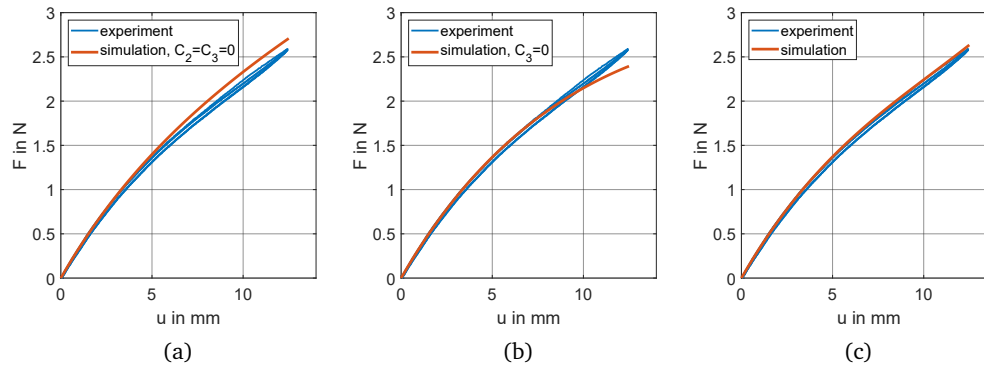


**Figure 6.5:** Approximation of the Yeoh material parameters based on an analytical plane strain model.

The parameters  $C_i$  are then tuned one by one. The results are shown in Figure 6.5. First, in Figure 6.5 (a),  $C_2$  and  $C_3$  neglected, which reduces the model to the Neo-Hooke material model. This simpler hyperelastic material model describes only right curvature in the stress-strain characteristic of a material, which means a softening of the material. Hence, the parameter  $C_1$  describes the overall right curvature. Figure 6.5 (b) adds the parameter  $C_2$  to the model, which influences the curvature for larger deformations, while Figure 6.5 (c) considers all three material parameters and is able to fit the analytical model to the experimental data. The approximated hyperelastic parameters for silicone and electrode are shown in Table 7.

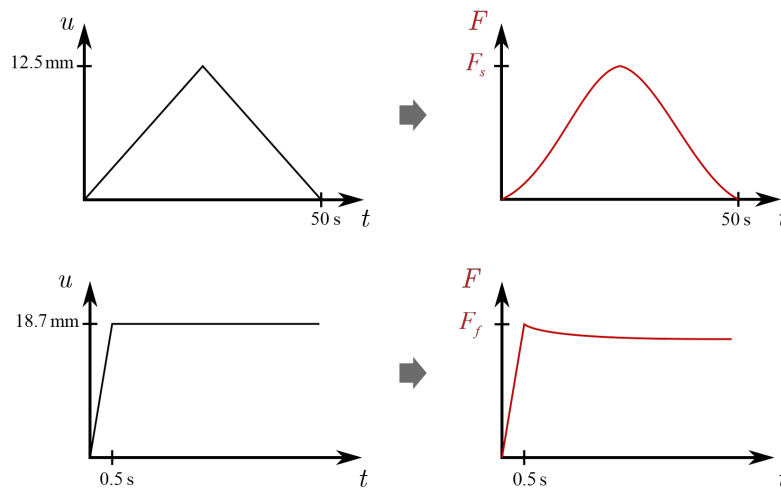


**Figure 6.6:** The identification of material parameters is performed in two steps: a slow experiment characterizes the hyperelastic parameters (upper row), while a fast experiment characterizes the viscoelastic parameters (lower row).

The second step of the identification process is based on the FE model and a numerical optimization process in order to improve the approximated parameters. Therefore, a cost function  $f$  is defined as

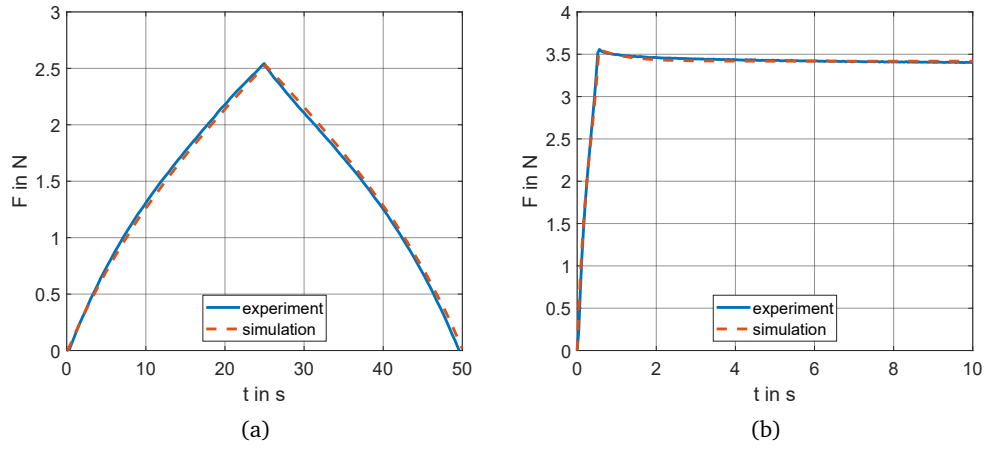


**Figure 6.7:** A comparison between experiment and simulation for the silicone film, without viscoelastic effects (a) and with viscoelastic effects (b).

$$f(\theta) = |F_c(\theta) - F_m|, \quad \theta = [C_1 \ C_2 \ C_3 \ \tau \ \beta]^T, \quad (6.18)$$

where  $F_c$  describes the in Comsol simulated reaction force of the FE model and  $F_m$  describes the force determined by experiments. With the in Matlab implemented Levenberg-Marquardt algorithm for nonlinear optimization problems [123], the cost function is minimized,

$$\min f(\theta) = f(\theta^*), \quad (6.19)$$

yielding the optimal material parameters  $\theta^*$ . For the identification of the hyperelastic parameters, no viscoelastic effects are simulated. In order to map the material behavior without viscoelasticity, experiments are performed in which the strip is deformed slowly (50 s for one cycle of 50 % deformation). A qualitative representation is shown in Figure 6.6, upper row. For the identification of the viscoelastic parameters, relaxation experiments are performed, which show the spring-dashpot behavior of the lumped model in Figure 6.3. A fast pull of the strip to a deformation of 75 % within 0.5 s generates non-equilibrium stresses which vanish over time. A qualitative representation is shown in Figure 6.6, lower row, where the force response shows the decay of the non-equilibrium stresses. The optimal parameters for both materials are shown in Table 7. For the case of the silicone film, force over time of experiment and FE simulation with optimal parameters are shown in Figure 6.7 and show good agreement.

	Silicone approx.	Silicone optimized	Electrode approx.	Electrode optimized
$C_1$ in Pa	$1.8 \cdot 10^5$	$1.73 \cdot 10^5$	$1.1 \cdot 10^5$	$9.84 \cdot 10^4$
$C_2$ in Pa	$-1.5 \cdot 10^4$	$-1.85 \cdot 10^4$	$-1 \cdot 10^5$	$-7.67 \cdot 10^4$
$C_3$ in Pa	$1.1 \cdot 10^4$	$8.1 \cdot 10^3$	$8 \cdot 10^4$	$7.52 \cdot 10^4$
$\tau$ in s	–	0.7	–	0.5
$\beta$ in s	–	0.03	–	0.15

**Table 7:** Material parameters for silicone film and electrode, analytical estimation and numerically optimized.

The identification of all material parameters is an important step in the development of a FE model. Nevertheless, all parameters require a validation by means of experiments.

For validation, four different experiments are performed and compared to a corresponding simulation. The model inputs, displacement and voltage, are shown in Figure 6.8 for all four experiments. The first validation for the material parameters without electromechanical coupling is shown in Figure 6.8 (a), which consists of a sinusoidal displacement of the DEA strip with a frequency of 0.25 Hz without applied voltage. In order to validate all discussed implementations for the electromechanical coupling, Figure 6.8 (b) shows the second validation experiment, which equals the first validation with an applied voltage of 2.5 kV. Figure 6.8 (c) shows the third input, which is a triangular 2.5 kV voltage signal of 1 Hz at a constant displacement of 12 mm. Finally, the input parameters in Figure 6.8 (d) show a biased sinusoidal displacement (maximal displacement of 12.5 mm and an offset of 2.5 mm), with a ramped voltage to 2.5 kV. A comparison between experimental results and simulation for all four experiments is shown in Figure 6.9 and show satisfying results. The validation of the material parameters without coupling shows a remarkable agreement in Figure 6.9 (a). In fact, both curves lie on

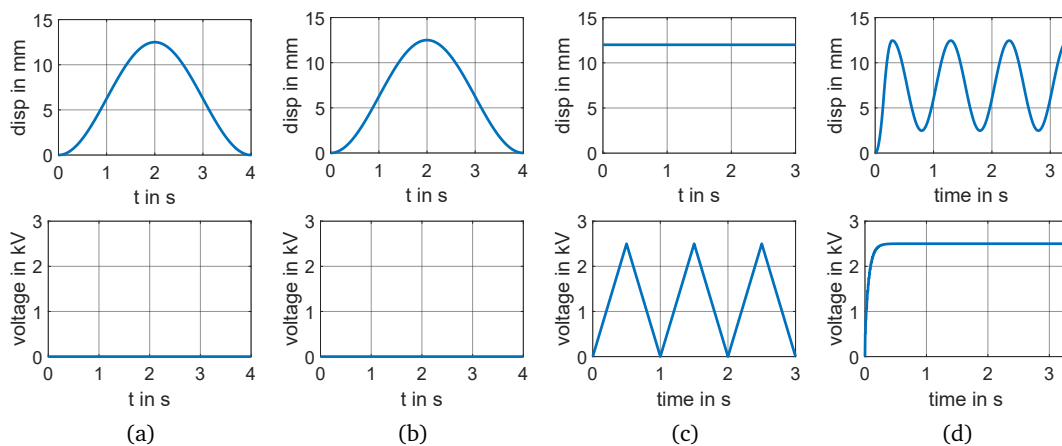


**Figure 6.8:** Input signals for all validation experiments: sinusoidal displacement without voltage (a), sinusoidal displacement with high voltage (b), constant displacement with triangular voltage (c) and biased sinusoidal displacement with ramped voltage (d).

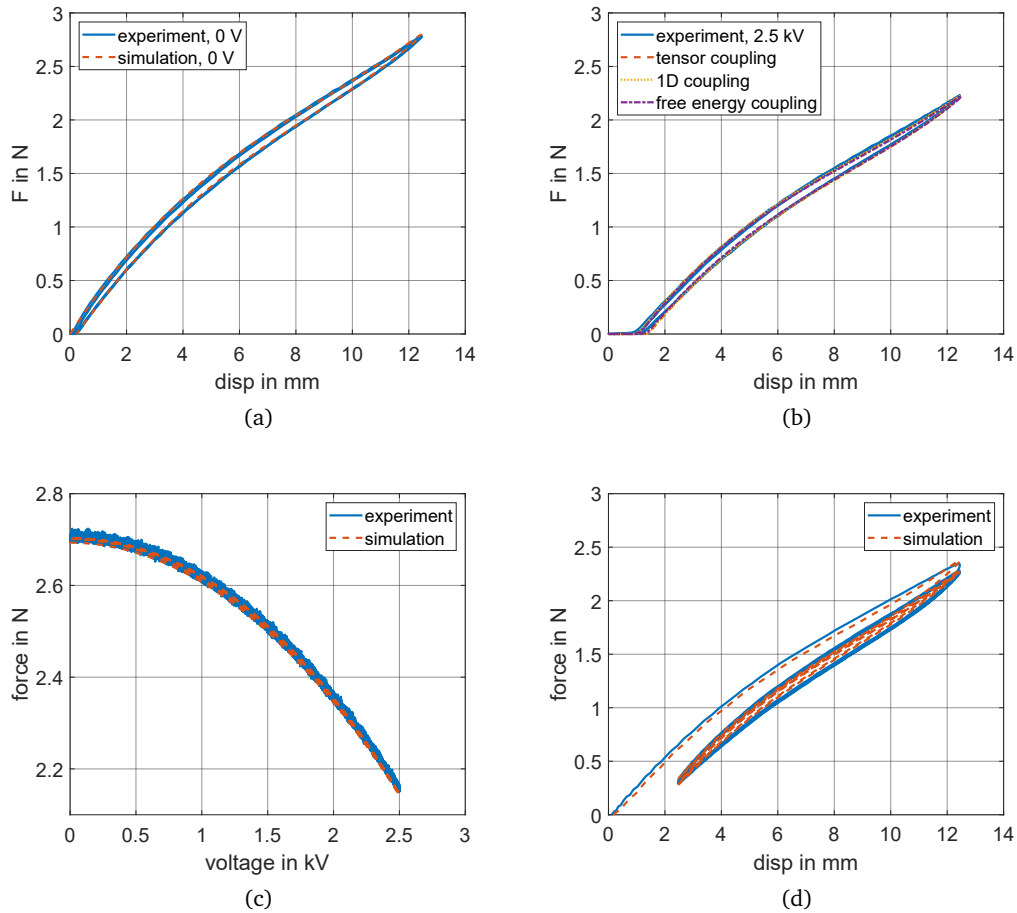


**Figure 6.9:** Model validations: 0.25 Hz sinusoidal displacement without voltage (a), 0.25 Hz sinusoidal displacement with high voltage (b), 1 Hz triangular voltage with constant displacement (c) and biased sinusoidal displacement with high voltage (d).

top of each other. For the validation of the electromechanical coupling, all three coupling approaches described in Section 6.3 are implemented into the Comsol FE model, completing the two-dimensional FE model. Figure 6.9 (b) shows experimental data and simulation with all three coupling implementations for the second experiment. A remarkable agreement between experiment and all three coupling implementations is visible. Between the coupling implementations, there are only small deviations. The implementation of the complete Maxwell stress tensor produces results which differ slightly from the other two implementations (maximum deviation smaller than 0.02 N). The one-dimensional coupling and the coupling based on the free energy both include the simplification of an electric field with only one component in  $z$ -direction, therefore yielding the exact same results. Experimental data for the third and fourth validation is shown in Figure 6.9 (c) and (d), both showing remarkable accordance as well. The match for the fourth experiment is slightly worse. In any case, a match between FE implementation and different experiments in this dimension is remarkable, due to deviations

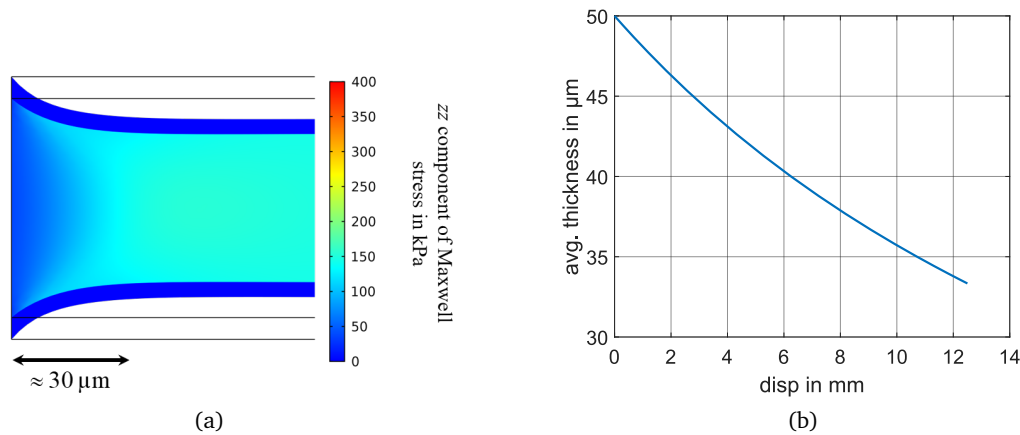


**Figure 6.10:** The narrowing of the strip is negligible after approximately  $30\ \mu\text{m}$  (a), therefore yielding an average thickness of the strip depending on its displacement (b).

in the experiments while adjusting the experimental setup or exchanging the DEA specimen. Note that, for these experiments, the electromechanical coupling implementation is based on the full Maxwell stress tensor. The agreement between all coupling mechanisms in the second validation experiment allows the negligence of a comparison for all coupling mechanisms.

Concerning the computation times, the first validation solves in 96 s, whereas the second validation with electromechanical coupling solves in 120 s (tensor and one-component coupling) and 123 s (free strain-energy coupling). Hence, all three coupling mechanisms are comparable in terms of computational cost. The third and fourth simulations solve in 360 s respectively 412 s. The longer computation times are due to the larger number of oscillations mapped by the simulation and are therefore expected. It is mentioned that for all in given simulation times axial symmetry of the structure is harnessed, thus only half the structure is modeled, reducing the computational cost.

Due to the simulation based on the FE method, local quantities such as stresses and strains can be investigated. Therefore, the narrowing at the edges of the strip are investigated in Figure 6.10 (a), which shows the deformed geometry with a surface plot of the Maxwell stress normal to the membrane. The deformation shows that the narrowing decays already after approximately  $30\ \mu\text{m}$ . Compared to the whole length of 25 mm, this narrowing is negligible. Therefore, the actual thickness of the DEA is practically equal to the approximated one, i.e., the strip practically deforms as an incompressible rectangle. This average thickness is depicted in Figure 6.10 (b) and represents an important quantity for a DEA. The electric field is prohibited to the breakdown field strength of the material, for the here used Wacker Elastosil 2030, the breakdown field strength equals  $80\ \text{V}/\mu\text{m}$ . For the applied voltage of 2.5 kV, a minimal allowed thickness results to approximately  $31\ \mu\text{m}$ . Within those experiments, the thickness does not fall below  $33\ \mu\text{m}$ , thus, electric breakdown does not occur. Note that the two-dimensional

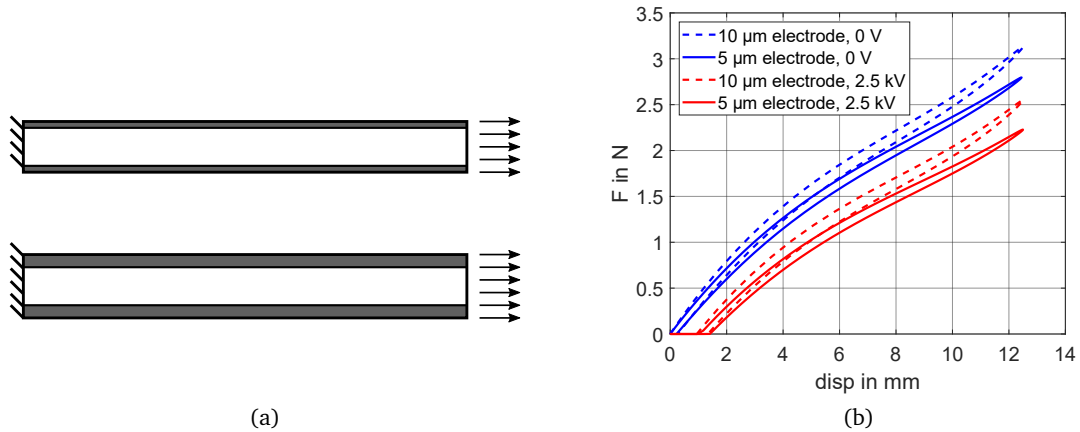


**Figure 6.11:** Comparison of a simulation with twice as thick electrodes, geometry sketch (a) and force-displacement curves (b).

approximation includes the simplification of no strain in the  $z$ -direction. This assumption influences the thickness of the strip, which is discussed in Chapter 7, where a three-dimensional representation based on membrane elements allows an examination of necking in  $y$ -direction at the unclamped edges of the DEA.

## 6.5 Effects of Discretized Electrodes

One of the main features of the presented model is the possibility of separately discretizing electrodes. Hereby, a variation of the electrode geometry can be examined. In this section, a variation in electrode thickness and its effect to the force-displacement characteristics of the DEA is discussed first, followed by a simulation with a patterned electrode and an examination of boundary effects between electrode and silicone film.

In order to vary the electrode thickness, Figure 6.11 (a) shows a sketch of the DEA with 5 μm thick electrodes from the previous chapter and a sketch with 10 μm thick electrodes. The resulting force-displacement plots are given in Figure 6.11 (b), 5 μm electrodes in solid lines and 10 μm electrodes in dashed lines. As expected, the stiffness of the actuator increases for thicker electrodes, while the effect of the electromechanical coupling (the work area between 0 V and 2.5 kV curves) remains constant. This result shows the magnitude of electrode influence onto the overall stiffness of the DEA. Adding further electrode material to the silicone film equals more material which has to be deformed when stretching the DEA, while the arising Maxwell stress does not change. This behavior is studied in [62]. Additionally, the hysteretic effect is amplified, which is explained by investigating the material parameters in Table 7. The energy factor  $\beta$  of the electrode material, which influences the width of the hysteresis, is more than

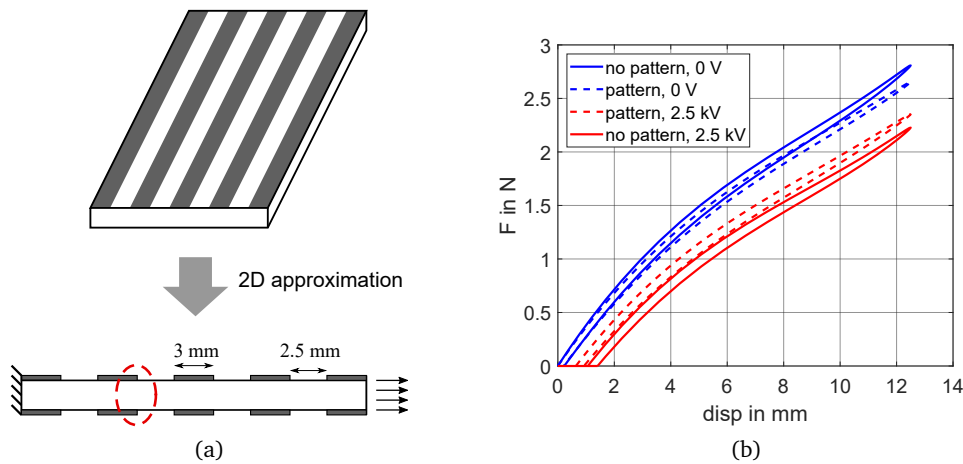


**Figure 6.12:** A patterned electrode (a) leads to a decrease in electromechanical coupling (b).

three times as large as for the silicone. Therefore, adding more electrode material increases the hysteretic effects, as shown in [59].

A further performed investigation is the effect of a patterned electrode structure, as shown in Figure 6.12 (a). Instead of simulating one continuous electrode on the  $25 \text{ mm} \times 125 \text{ mm}$  silicone surface, 5 strips with a width of 3 mm are applied onto the silicone surface, with a distance of 2.5 mm. This geometry is chosen as an exemplary division of the DEA, in order to investigate the transition from plain silicone to electrodes.

For the global quantities, namely force over displacement, the results are shown in Figure 6.12 (b). The solid lines show the reference strip with continuous electrodes, whereas the dashed lines represent the patterned structure. In the 0 V case (blue line and dashes), the stiffness of the patterned sample is smaller, due to the lack of electrode material compared to the continuous electrode. With applied high voltage (red line and dashes), the active area which generates the Maxwell stress, is smaller in the patterned case, leading to less Maxwell stress, and, in turn, to a smaller work area compared to the continuous electrode strip. Hence, the performance of the strip decreases.

Investigating local values, such as stresses in the strip and the electric field shows remarkable distributions. The upper row of Figure 6.13 shows mechanical stresses, the  $xx$ -component of the second Piola-Kirchhoff stress (a) and the  $zz$ -component of the Maxwell stress (b) at the maximum stretch of 12.5 mm. The part of the DEA shown in these plots is the transition between silicone with electrode and plain silicone, which is marked with a red dashed circle in Figure 6.12 (a). Comparing the thickness of the silicone strip between the electrodes  $d_e$  and at the silicone without electrode  $d_s$ , the thickness differs by  $2 \mu\text{m}$ . This additional compression between the electrodes is generated by the Maxwell stress, which squeezes the silicone between the electrodes. A further observation is that the  $xx$ -component in Figure 6.13 (a) between the electrodes (208 kPa) is smaller than outside the electrodes (257 kPa). This effect

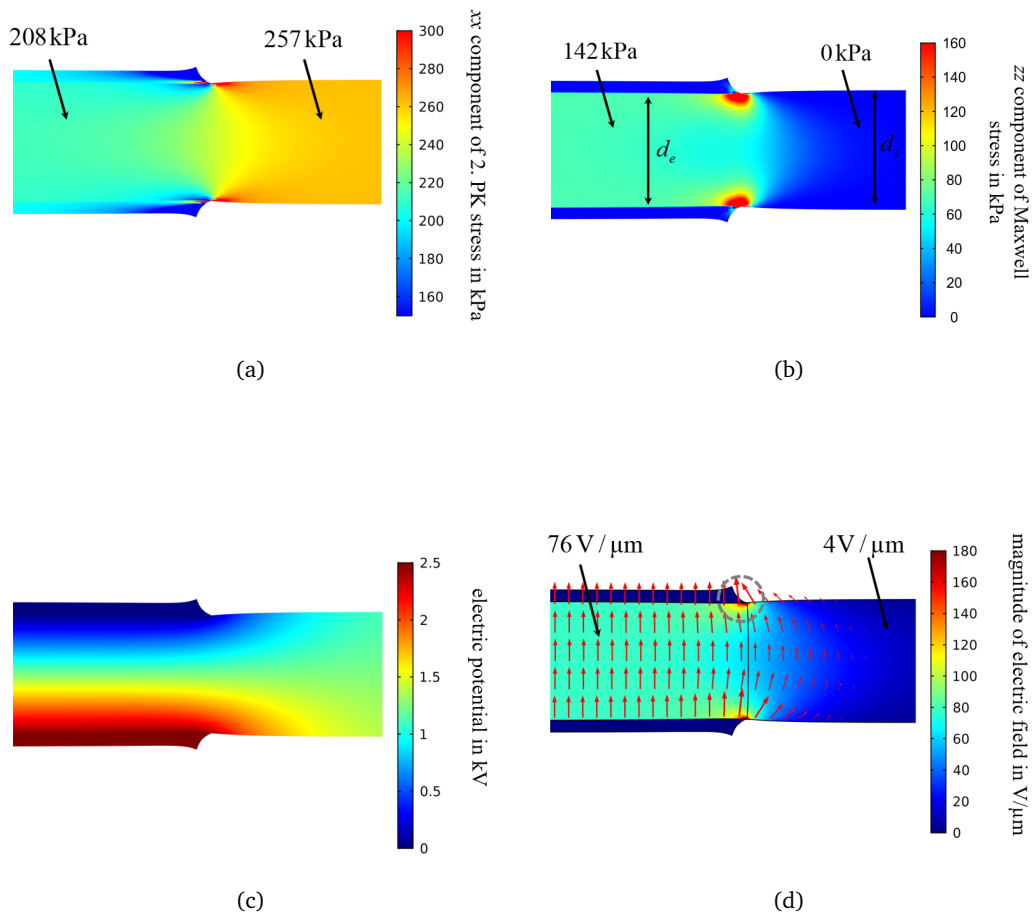


**Figure 6.13:** Different field distributions at the electrode edge:  $xx$ -component of the 2. PK stress (a),  $zz$ -component of the Maxwell stress (b), electric potential (c) and magnitude of the electric field (d).

is explained by the fact that the force which deforms the strip distributes the stress onto a larger area between the electrodes (silicone and electrodes), whereas in the free silicone region, the thickness consists of the silicone only. The Maxwell stress distribution in Figure 6.13 (b) shows a continuous distribution between the electrodes (142 MPa) and vanishes outside the electrodes, as expected. Both field distributions in Figure 6.13 (a) and (b) show peaks at the sharp edges between electrode and silicone film. For the mechanical stress in Figure 6.13 (a), they arise due to singularities at sharp corners, as described in [124]. In nature, usually no perfectly sharp edges exist. Therefore, this overstresses do not arise in the actual DEA. Furthermore, the strain energy in the system converges, leading to a physical result in the simulation, as discussed in Section 5.3. At the electrode edge, the actual screen-printed material blurs, which also prevents the development of a sharp corner. However, in order to explain the overstress in the Maxwell stress in Figure 6.13 (b), the electric field must be investigated. The lower row of Figure 6.13 shows electric quantities, namely the electric potential (c) and the magnitude of the electric field including a vector plot (d). As stated in equation

(6.7) and (6.8), the Maxwell stress is approximately proportional to the square of the electric field, so the peaks in the edges in this case arise from the peaks in the electric field in Figure 6.13 (d), gray circle. Those edges are visible, although the electric potential in Figure 6.13 (c) is smooth. The reason is the so called edge effect, which is discussed in [125]. Basically, the surface charges are gathered at the edges of the electrodes, which increases the electric field at the edges as well. Although this peak represents a singularity similar to the one in Figure 6.13 (a), the overall electric energy converges once again for the whole system, therefore producing physical results. Such a field peak in the silicone would lead to an instantaneous electric breakdown, since the breakdown strength of the material is exceeded. However, the peak decays after a few micrometers. Additionally, due to the electric field fringing outside of the electrodes, the field strength on the vertical line between the field peaks is decreased. Hence, these parts of the material are not exposed to large electric fields as the edges are. The overall electric fringe field is depicted in the vector plot in Figure 6.13 (d). The logarithmic scale of the vector arrows allows a qualitative representation of the field decrease, forming the fringe field pattern of a non-ideal parallel plate capacitor.

## 6.6 Discussion of Results

In this chapter, a Finite Element model for the simulation of membrane DEAs has been introduced, which includes large deformations, hyperelastic material behavior, viscoelasticity and electromechanical coupling. It is based on two-dimensional continuum elements and suitable for geometries which deform approximately in manners of a plane strain state. The use of a two-dimensional model allows a fine discretization of the DEA cross-section with acceptable computational cost compared to a fully three-dimensional model. In order to validate the model, experiments with a standardized DEA strip have been performed and the material parameters have been identified. Subsequently, the model has been validated with further experiments and three different approaches for implementing the electromechanical coupling have been discussed and compared. The model feature of separately discretized electrodes allows a deeper investigation of effects such as electrode thickness or patterned electrodes. Both have been studied and the discussed. In particular, the simulation of a patterned electrode shows remarkable field distributions (electric field, mechanical stress) which differ from averaged values based on a lumped model.

Further model expansions by inertial effects would provide the possibility of a membrane vibration analysis. Such investigations are highly interesting in the field of acoustics, e.g., for DE loudspeakers [39, 126], or general investigations of the resonant behavior of dielectric elastomers [127, 128]. Resonances and corresponding modes can be suppressed or amplified by an excitation with a suitable patterned electrode, whose geometry can be optimized by using an FE model.

The limitations of the model introduced here are due to the demand of a plane strain geometry, which is not true for all DEA geometries. In order to avoid this drawback, which also improves the computational cost compared to three-dimensional continuum elements, the next chapter introduces an implementation based on three-dimensional membrane elements. The results in this chapter are compared to this membrane formulation and advantages and disadvantages are exhibited.



## 7 Finite Element Modeling of Three-Dimensional Membrane Geometries

In the previous chapter, a FE model for plane strain DEA geometries is derived, based on two-dimensional continuum elements. The model produces satisfactory results, especially for local field distributions at the transition between silicone and electrodes. However, its applications are restricted to plane strain deformed geometries. In order to overcome this limitation, an enhanced model based on theory developed for the two-dimensional case is derived in this chapter, which allows the simulation of arbitrary DEA geometries deforming in all three dimensions. As studied in Section 6.1, a three-dimensional discretization of a membrane with continuum elements leads to large FE models with computations times which are unsuitable for multiple model evaluations. Hence, the formulation in this chapter is based on membrane elements, which permit a three-dimensional deformation while the surface discretization remains two-dimensional. In other words, the level of discretization remains on a level comparable to the model in Chapter 6, while the membrane can be deflected in three dimensions. Hence, effects such as necking or thickness field distributions are observed. The model does not offer the possibility of separately discretized electrodes, which is a drawback compared to the two-dimensional model. The arbitrary deformation, though, allows the simulation of out-of-plane deflected DEA geometries, such as COP (cone-shaped out of plane) or SOP (strip out of plane). In this chapter, a first membrane model is developed and the standardized strip geometry from Chapter 6 is simulated, for comparison with the two-dimensional model results. For this purpose, the chapter is divided as follows. First, the basics on membrane elements, their overall functionality, advantages, disadvantages and included simplifications are discussed. Next, the theory from the two-dimensional model is adapted in order to develop a membrane element for large deformations, including hyperelasticity, viscoelasticity and electromechanical coupling. Particularly, the electromechanical coupling must be adapted due to the structure of membrane elements, which prohibits stresses normal to the membrane surface. The model is then validated and compared to the results of the two-dimensional model in Chapter 6. Effects which could not be mapped by the two-dimensional model are investigated with the membrane model, such as thickness fields, necking, and their influence on global values such as the reaction force. Finally, further electrode geometries are investigated and evaluated.

## 7.1 Discretization of Three-Dimensional Membrane Structures

Membrane formulations are suited for the FE modeling of membrane-like structures, which means structures with an area much larger than their thickness. A discretization with continuum elements for such geometries is, as stated in Chapter 6, highly inefficient due to the need of many elements in order to discretize the small thickness. The overall idea is a local assumption of a plane stress state for each element, which means the negligence of stresses normal to the membrane surface. As a result, bending stiffness is neglected. In order to pursue this task, the deformation gradient  $\mathbf{F}$  for membrane elements is decomposed into a tangential component  $\mathbf{F}_T$  and a normal component  $\mathbf{F}_N$ , leading to  $\mathbf{F} = \mathbf{F}_T \mathbf{F}_N$ . Membrane elements are defined in the three-dimensional space, being discretized with two-dimensional elements, hence are defined on a surface. Thus, not all spatial derivatives exist. In order to account for tangential derivatives only, we introduce the tangential derivative operator  $\nabla_T$ . Based on the general representation of the deformation gradient as  $\mathbf{F} = \mathbf{I} + \nabla \mathbf{u}$ , the normal component is subtracted, yielding

$$\mathbf{F}_T = \mathbf{I} - \mathbf{N} \cdot \mathbf{N}^T + \nabla_T \mathbf{u}, \quad (7.1)$$

with  $\mathbf{u}$  being the spatial displacement field vector. The qualitative idea is that the deformation in the normal direction is induced by an additional term dependent on the transversal stretch  $\lambda_n$  in direction of the membrane normal vector  $\mathbf{n}$  in the deformed, respectively  $\mathbf{N}$  in the undeformed configuration,

$$\mathbf{F}_N = \lambda_n \mathbf{n} \cdot \mathbf{N}^T. \quad (7.2)$$

For further details, see [129, 130].

Although the discretization is performed on a two-dimensional level, a membrane element allows deformations in three dimensions, offering arbitrary geometries and deformations of the modeled membrane. Although the thickness  $d$  is not discretized with two-dimensional membrane elements, it can be calculated due to the known transversal stretch  $\lambda_n$  and the initial thickness  $d_0$ , as follows

$$d = \lambda_n d_0. \quad (7.3)$$

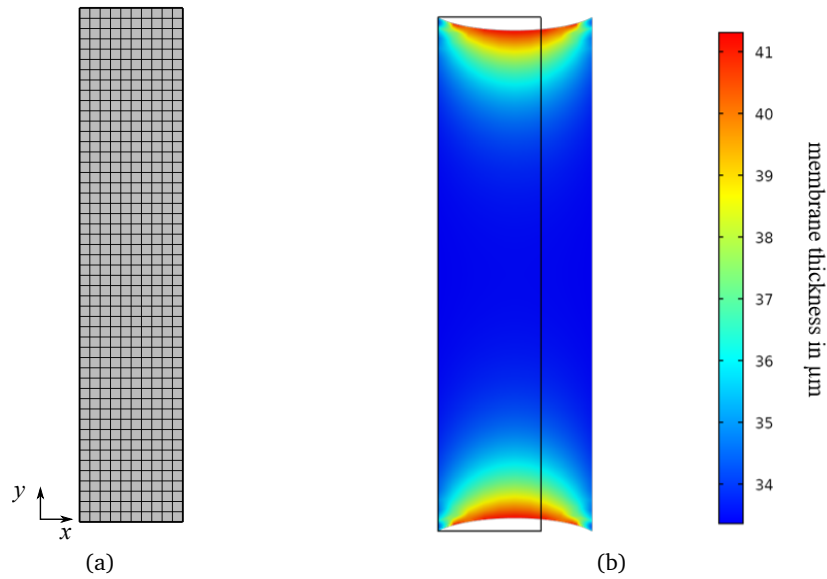


**Figure 7.1:** A discretization with two-dimensional hexahedron membrane elements permits a highly efficient DEA model (a), effects such as necking and thickness change can be mapped by the model (b).

The membrane geometry examined in Chapter 6 is chosen in this chapter for comparison, with the dimensions  $25\text{ mm} \times 125\text{ mm} \times 60\text{ }\mu\text{m}$ . The discretization is performed with hexahedron membrane elements, as shown in Figure 7.1 (a). An exemplary thickness distribution is shown in Figure 7.1 (b), which also exhibits necking. In the two-dimensional model in Chapter 6, necking effects are prohibited due to the plane strain approximation. Concerning the solver parameters in Comsol Multiphysics, all settings remain as defined in Chapter 6. Any deviations from these settings are noted at the corresponding simulation results.

In order to use a membrane formulation for the simulation of a DEA, all features of the two-dimensional model must be implemented as well, namely large deformations, hyperelasticity, viscoelasticity and electromechanical coupling. Whereas the first three features can be implemented in the same way as performed in Section 6.2 or are already available in Comsol, the electromechanical coupling requires a deeper discussion, which is performed in the subsequent section.

## 7.2 Electromechanical Coupling for a Membrane Formulation

Whereas the implementation of hyperelasticity and viscoelasticity is adapted by the usage of the newly defined deformation gradient, realizing the Maxwell stress must be discussed further. The physical principle of the Maxwell stress is the attraction of both electrodes, inducing

a compressive stress normal to the membrane surface. However, the membrane formulation is based on a plane stress approximation which neglects stresses in normal direction. The first two of the three coupling implementations discussed in Section 6.3 are based on stresses normal to the membrane. Hence, these methods are not suitable for the membrane element model. Additionally, the first method uses the electric field calculated by solving the electrostatic field formulation (5.16)-(5.19). Without a discretization of the membrane thickness, there are no opposite electrode surfaces, hence, the Dirichlet boundary conditions for the electric potential cannot be applied. Consequently, there is no comparable way of simulating the electric field distribution of the membrane as shown in Figure 6.13. This leaves the approximation of the electric field under negligence of fringe effects. The normal component of the electric field is then calculated based on the applied electric potential and the calculation of the thickness in equation (7.3), yielding

$$e_z = \frac{V_{el}}{d} = \frac{V_{el}}{\lambda_n d_s}, \quad (7.4)$$

with  $d_s$  being the initial thickness of the silicone film without electrodes. The exact same simplification is performed for the second method of Section 6.3. The third discussed method, which is based on the expansion of the strain free-energy, does not depend on a discretized thickness of the membrane and is suitable for the membrane theory, because also here the stresses are derived from the free strain-energy density and the given deformations.

A second possible implementation for the membrane theory is based on the free strain-energy description in [121] and the assumption of incompressibility, which leads to a further representation of the Maxwell stress tensor as

$$\boldsymbol{\sigma}^{MW} = \varepsilon_0 \varepsilon_r e_z^2 \begin{pmatrix} 1 & 0 & 0 \\ 0 & 1 & 0 \\ 0 & 0 & 0 \end{pmatrix}. \quad (7.5)$$

This representation describes a transformation of the Maxwell stress as a normal component onto the membrane to in-plane components which lead to the same deformation. This conclusion is verified by inserting both Maxwell stress tensor representations (6.8) and (7.5) into the Hooke's law for isotropic continuous materials. Both stresses yield the same deformation for isotropic media, as discussed by Kaal [110, Chapter 2.5] for the second coupling mechanism in Section 6.3 as well. Further details to the transformation of the in-plane Maxwell stress can be found in [21]. For both implementations, it must be considered, that the membrane structure

has a thickness of 60  $\mu\text{m}$ , but the area on which the Maxwell stresses act is the silicone with a thickness of 50  $\mu\text{m}$ .

### 7.3 Model Validation and Comparison to Two-Dimensional Model

In order to compare both coupling mechanisms, the initial thickness of the modeled membrane is crucial. In the two-dimensional case in Chapter 6, the thickness of the silicone film is given as 50  $\mu\text{m}$ , whereas the thickness of the electrodes is given as 5  $\mu\text{m}$ . From a mechanical point of view, the membrane has a combined thickness of 60  $\mu\text{m}$ . However, from an electrical point of view, the Maxwell stress acts on the silicone surface of the membrane, which leads to an overall membrane thickness of 50  $\mu\text{m}$ . In order to map both behaviors, both thicknesses are considered in this model. As mechanical thickness 60  $\mu\text{m}$  is chosen, which reflects the combination of silicone film and imprinted electrodes. The hyperelastic material parameters are averaged, following the composition of the sandwich structure, proportional to the thicknesses. For the averaged three material parameters  $C_i^m$  of the membrane follows

$$C_i^m = \frac{d_s}{d_0} C_i^s + \frac{2d_e}{d_0} C_i^e, \quad (7.6)$$

with  $C_i^s$  and  $C_i^e$  being the Yeoh parameters of silicone and electrode, respectively (see Table 7). The viscoelastic parameters are treated the same way, resulting to a relaxation time  $\tau_m$  of 0.67 s and an energy factor  $\beta_m$  of 0.07.

The resulting force-displacement curves of the two-dimensional model and the membrane model are compared in Figure 7.2. (b), with the solution of the two-dimensional model (blue curve), the membrane solution without necking as plane strain deformation (yellow dashed curve) and the membrane with necking (red curve). The comparison between two-dimensional model and plane strain deformed membrane model shows a perfect fit and validates the parameter averaging in equation (7.6). The simulation without pure shear boundaries yields a necking of the membrane, as shown in Figure 7.2 (a), right hand side. The force-displacement curve of the membrane with necking (see Figure 7.2 (b), red curve) shows a decrease in stiffness, with the maximal force value at 50 % stretch changing from 2.8 N (pure shear) to 2.7 N (necking). This decrease in force is expected, because the necking effect softens the actuator. The thickness distribution in Figure 7.2 (a) additionally shows the increase in thickness at the necking edges. Due to the geometry being close to a pure shear deformation case, the thickness in the middle of the strip is approximately the same for the pure shear and for the necking simulation. In order to map the necking of the membrane model, the material

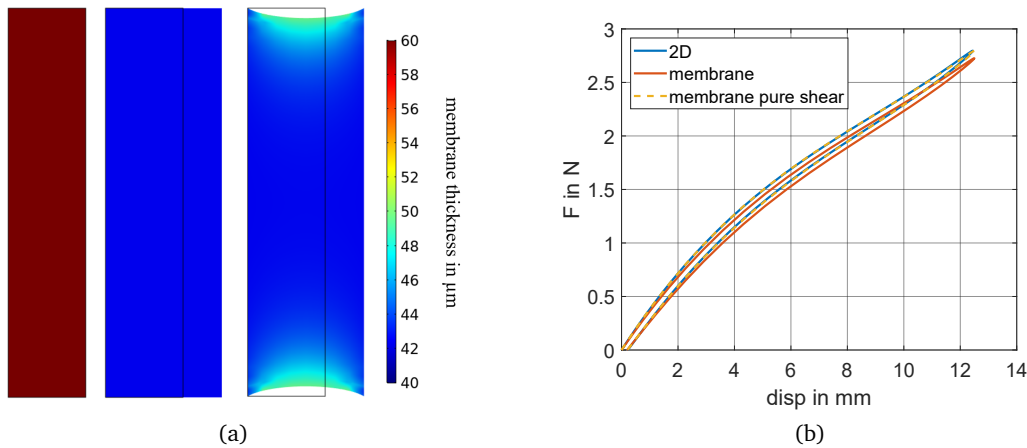


**Figure 7.2:** A comparison of a non-deflected membrane, pure-shear deformed membrane and a membrane with necking (a), the simulation with the identified two-dimensional material parameters yields a perfect fit for pure shear membranes (dashed yellow curve) and shows a softening (red curve) due to necking (b).

parameters must be adjusted. In order to achieve this goal, the hyperelastic parameters  $C_i$  are scaled by the quotient of the maximal forces of two-dimensional model and membrane model, which calculates to  $2.8 \text{ N}/2.7 \text{ N}$ . Then, the optimization algorithm as described in Section 6.4 is utilized in order to match the force-displacement curve in Figure 7.2 (b). The adjusted membrane parameters are shown in Table 8. A comparison of necking membrane and experimental data is shown in Figure 7.3 (a), producing a remarkable fit. Further validation simulations are performed in the style of the validation experiments of Section 6.4, with results displayed in Figure 7.3 (b)-(d). The results are comparable to the validation in Section 6.4. Both described implementations of electromechanical coupling for membranes are compared in Figure 7.3 (b), which show a marginally lower force than the two-dimensional continuum model in Figure 6.9 (b), and a second validation of the coupling is shown in Figure 7.3 (c), again showing a smaller force as the two-dimensional simulation in Figure 6.9 (c). This effect shows a decrease in actuator stiffness due to electrical actuation, as soon as the pure shear changes to a uniaxial deformation state, in other words, provides necking. This effect is also observed and discussed in detail in [21]. The last validation experiment in Figure 7.3 (d) also shows comparable results to the two-dimensional case in Figure 6.9 (d). Note that for the electromechanical coupling in the last two validation simulations, in-plane stresses as described by equation (7.5) are chosen. Combining these results, the membrane model shows

$C_1$ in Pa	$C_2$ in Pa	$C_3$ in Pa	$\tau_m$ in s	$\beta_m$
$1.61 \cdot 10^5$	$-2.82 \cdot 10^4$	$2.17 \cdot 10^4$	0.67	0.07

**Table 8:** Material parameters for the membrane simulation model.

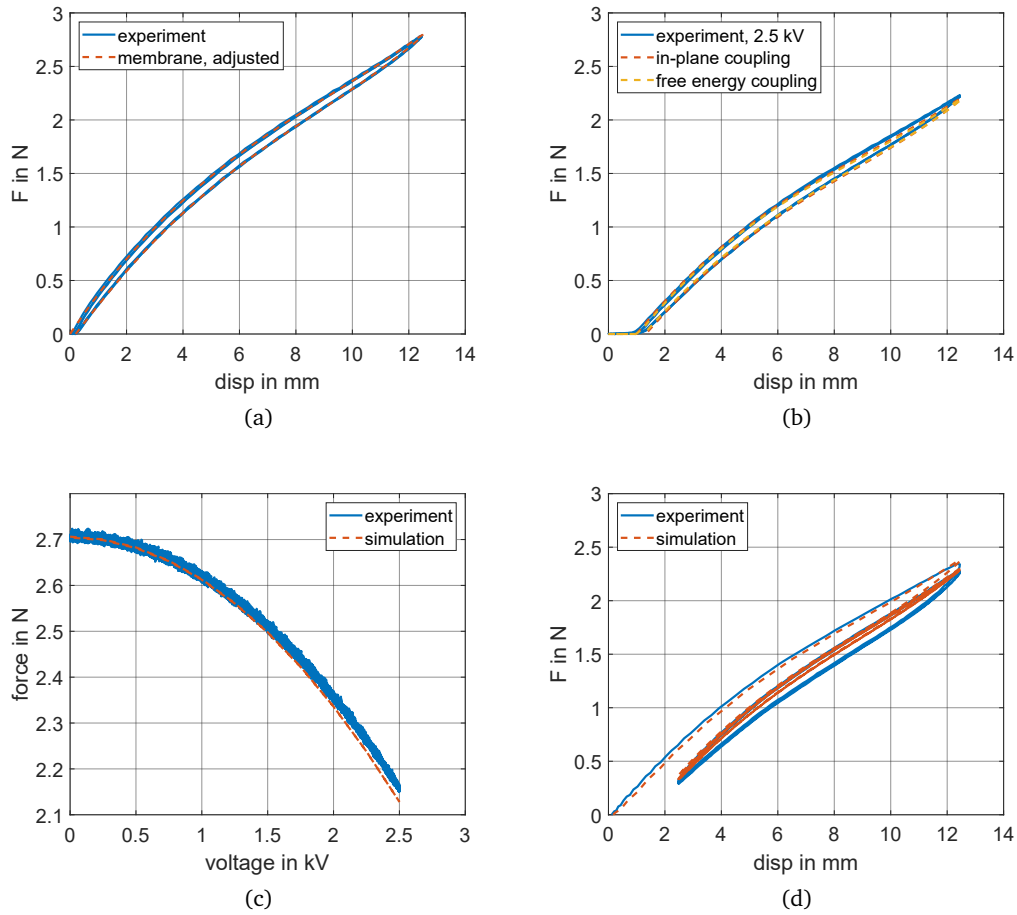


**Figure 7.3:** Model validation for same experiments as shown in Figure 6.9, with input signals as shown in Figure 6.8. The results are as satisfying as the two-dimensional simulations, with a slightly larger coupling effect.

its capability of simulating DEAs with including the effects of overall thickness change and necking effects at unclamped edges.

Concerning the simulation times, the membrane model shows a faster, and therefore more efficient computation due to the better aspect ratio and therefore smaller number of elements. The first validation model without electromechanical coupling solves in 33 s, while the second validation with electromechanical coupling solve in 53 s (in-plane coupling), respectively 49 s (free-energy coupling). The last two validation simulations solve in 62 s respectively 203 s. In comparison to the computation times of the two-dimensional model, it can be concluded that the membrane model solves substantially faster, by a factor between 2 to 6, depending on the simulation scenario. In order to verify the calculated thickness field, a further comparison between simulation and experiment is drawn. Figure 7.4 (a) shows an undeflected and a deflected DEA membrane, whose thickness is measured at a fixed line in the middle of the DEA in the reference state. The measurement is performed with the test rig described in [131], where

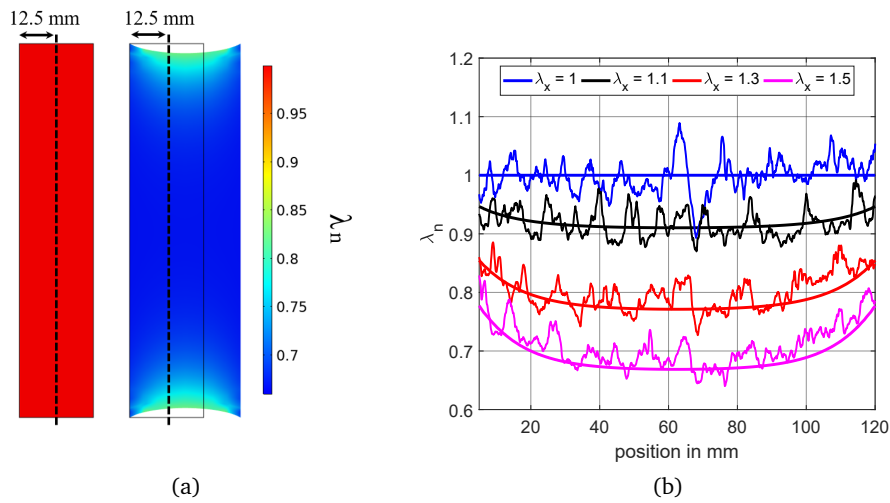


**Figure 7.4:** A thickness scan along a fixed line in the middle of the unstretched probe (a) shows a remarkable agreement between measurements and simulation for different stretches (b).

the membrane thickness is measured with two confocal displacement sensors (Micro-epsilon, confocalDT IFS 2405). Note that the measurement line does not move in  $x$ -direction during deformation of the DEA. For every stretch, the thickness is measured at 12.5 mm displacement referring to the left edge, as shown in Figure 7.4 (a). Different measurements are performed without applied voltage, where the strip is stretched by 0 %, 10 %, 30 % and 50 %. Before the thickness measurement starts, a dead time of 10 s is maintained in order to decay any viscoelastic effects. The same procedure is followed in the numerical model, with the results shown in Figure 7.4 (b). The noise of the thickness measurement results from the uneven surface of the screen-printed electrodes. Nonetheless, the simulation results show remarkable results compared to the experimental data. Note that not the whole strip length of 125 mm is depicted, because the necking of the strip permits measurements at the edges. The hereby thoroughly validated membrane model can be used to simulate further geometric influences onto the DEA, which is performed in the next section, where a patterned electrode similar to Section 6.5 is modeled and examined.

## 7.4 Effects of Patterned Electrodes

For the investigation of an electrode pattern as described in Section 6.5, the model structure differs between two-dimensional model and membrane model. Whereas the two-dimensional model inherits a different thickness for areas with and without electrodes due to the discretized electrodes, which provide a thickness of  $5 \mu\text{m}$  each, the membrane material model is averaged, as described above. Thus, the model is not suitable for an electrode pattern with changing thickness for plain silicone and silicone with applied electrodes. In order to overcome this

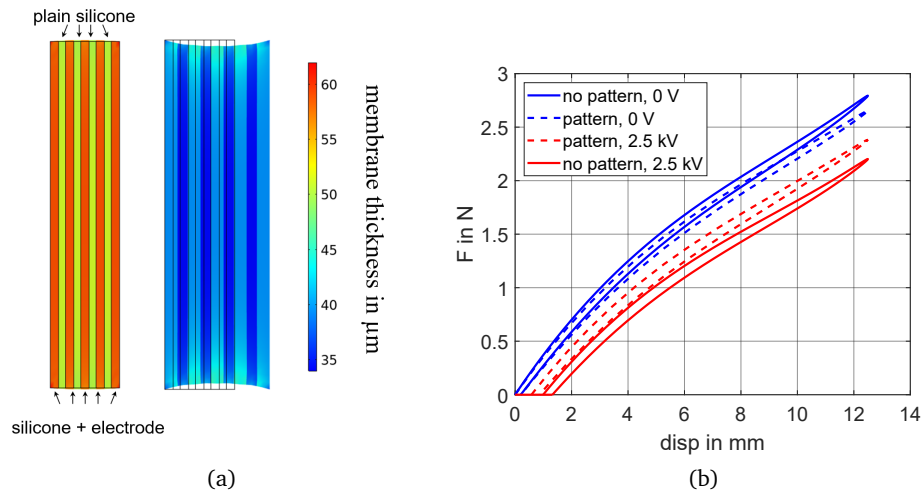


**Figure 7.5:** The actuated patterned membrane shows necking and a thickness distribution (a), while the force-displacement curves match the two-dimensional simulation (b).

issue, the membrane model is expanded for the patterned electrode by using two material models with different properties, as shown in Figure 7.5 (a).

The model for silicone with electrodes is exactly as described above, with the material parameters in Table 8 and a thickness of  $60\ \mu\text{m}$ . Electromechanical coupling is implemented in terms of in-plane stresses, as stated by equation (7.5). For the passive areas without electrodes, the material parameters for plain silicone are chosen, which are described in Table 7, while the thickness for this material model is reduced to  $50\ \mu\text{m}$ . Electromechanical coupling is not implemented into the silicone model, therefore no Maxwell stresses are applied to these areas. The model geometry is then split in active DEA parts and plain silicone parts, which are assigned to the corresponding material model. The evaluated model is depicted in Figure 7.5 (a), undeflected (left) and 50 % stretch (right), with the thickness field showing a clear distinction between silicone and electrode area. The model is solved with applied voltage of 2.5 kV, which is visible at the slight positive necking in the undeflected state. This necking occurs due to the applied Maxwell stress, which leads to a pressure state in the membrane. This pressure state leads to a squeezing of the membrane in  $y$ -direction. When the DEA is stretched to 50 %, the necking leads to an increase in membrane thickness, which is visible in the necking area of the deflected strips, which is also shown in Figure 7.2 (a). The force-displacement characteristic of the patterned DEA is shown in Figure 7.5 (b), and shows the same behavior as in the two-dimensional case in Figure 6.12 (b). For further model evaluation, local field distributions are shown in Figure 7.6, with the  $xx$ -component of the second Piola-Kirchhoff stress (a), the norm of the Maxwell stress (b) and the norm of the electric field (c). For each field in Figure 7.6, values in the middle of the DEA and in the necking area are depicted.

A comparison with the values of the two-dimensional simulation in Figure 6.13 shows a satisfying match between both models in the middle area, whereas in the necking area, all values of

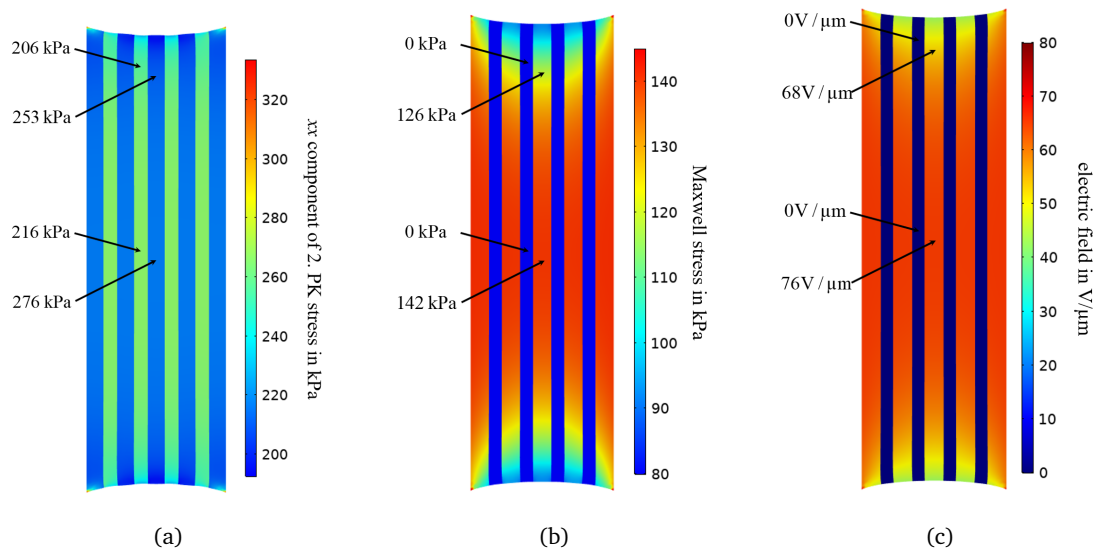


**Figure 7.6:** Local field distributions of the  $xx$ -component of the second Piola-Kirchhoff stress (a), the Maxwell stress (b) and the electric field (c).

the membrane model decrease. This effect is due to the advantage of mapping necking effects with the membrane model. Due to the necking, the thickness in this area increases, as shown in Figure 7.2 (a). The increase in thickness leads to a decrease in stresses and in the electric field. The middle area deforms closest to a pure shear state, hence, the results reproduce the two-dimensional simulation, which assumes a plane strain deformation. In conclusion, the membrane model includes the necking effect, hence, the results derived by the model concerning field quantities in the necking areas are superior over the results of the two-dimensional model.

Overall, a satisfying match between both models is shown. Note that field peaks as in the two-dimensional model do not appear in the membrane formulation, due to the lack of discretized electrodes and therefore intersecting edges in the model. This drawback is compensated by the benefits of the membrane model, which maps necking effects and resulting thickness distributions.

## 7.5 Discussion of Results

In this chapter, a FE model for the simulation of membrane DEAs is presented, which is based on membrane theory. Similarly to the two-dimensional model in Chapter 6, the formulation includes large deformations, hyperelastic material behavior, viscoelasticity and electromechanical coupling. The use of a membrane formulation allows the mapping of necking effects of

the membrane as well as precise thickness fields. To harness these features, the model is tuned in order to fit the experimental data of the DEA specimen. Alongside the validation simulations of Chapter 6, also thickness measurements of a stretched DEA are reproduced with the membrane model, yielding satisfying results. The simulation of a patterned electrode shows the differences to the two-dimensional modeling. While the two-dimensional model is able to map field peaks due to the separately discretized electrodes, the membrane formulation shows changes in stress and electric field in  $y$  direction, which is neglected in the two-dimensional modeling approach. Especially in the necking area, the electric field and the resulting electromechanical coupling are influenced significantly. Hence, a mapping of these effects in a FE model is highly valuable. The computation time of the membrane model exceeds the computation time of the two-dimensional model by a factor 2 to 6, leading to a fast FE model for DE membrane actuators.

Further research direction can potentially focus on different actuator geometries, especially uniaxial DEA strips or conical shapes, because such geometries are prohibited in the two-dimensional model, but can be investigated with a membrane simulation. An inclusion of inertial effects would allow the simulation of vibrations modes and resonance frequencies, as have been studied experimentally in [127]. Additionally, an optimal electrode geometry could be suitable for amplifying or attenuation of a resonance mode. A deeper investigation of electrode patterns could lead to optimal electrode designs based on parameter sweeps. The fast computation times of the model allow a fine sampling of a parameter space.



## 8 Conclusion and Outlook

This thesis provides advanced design concepts for membrane dielectric elastomer actuators and sensors, including an efficient Finite Element analysis of membrane DEAs based on a two-dimensional continuum formulation and a three-dimensional membrane formulation. In order to further the use of dielectric elastomer technology in applications, such design concepts and simulation models are crucial for system developers. The aim of this thesis is the provision of advanced tools, on experimental and simulation basis. Only such tools allow the reliable and optimal development of actuator and sensor devices.

The first part of this thesis examines design concepts for actuator and sensor systems and their experimental validation. Even though different design approaches are proposed in literature, new design concepts for large stroke actuator systems with advanced biasing systems are investigated in this work, which enhance technology capabilities in the actuator field. Optimal designs are deduced and verified with experimental data. Further work in this field could focus on the dynamic behavior of actuator systems in order to harness dynamic forces, e.g., by running a system in resonance.

For the development of sensors based on DE technology, the field of high pressure measurements, so far neglected, is studied in detail, and its potential is shown by investigating two main measurement topologies. First, an intrusive measurement concept with a pressure range up to 10 bar shows results which are comparable to a commercially available pressure sensor. As a second case study, a nonintrusive, high pressure measurement inside a polymer tube for pressures up to 62 bar shows further capabilities of the technology. The investigated concept for injection pumps shows the capability of DE sensors for applications in the medical field. For future research, both concepts could be expanded for larger pressure ranges, exhibiting the limits of high pressure measurements with DE sensors. Additionally, the development of suitable electronics for capacitance measurement, which are small and low-cost, is of interest.

The second part of this thesis has examined numerically efficient Finite Element modeling approaches for fast simulations of membrane DEAs, enabling computation times in the sub-minute order. The first approach based on a two-dimensional representation of plane strain deformed structures includes a separate discretization of both electrodes and maps hyperelastic as well as viscoelastic material behavior. Different implementations of the electromechanical coupling mechanism during electrical actuation are derived and compared. The separate

electrode discretization allows the investigation of field distributions at the edges between electrode and polymer, which is examined for the special case of a DEA with a patterned electrode. The second approach based on a three-dimensional membrane formulation expands the capability of the two-dimensional model by canceling the restriction of plane strain deformed geometries. This formulation enables the efficient simulation of arbitrary DE membrane actuators and an examination of local quantities such as stress, strain or electric field. A comparison between two-dimensional and membrane model is drawn by simulating equal structures, showing the up- and downsides of both modeling approaches. Future work in the simulation field should include inertial effects of the membrane in order to map further dynamic behavior besides viscoelasticity. The development of an optimization algorithm for optimal electrode geometries or actuator performance could harness the fast computation time of the presented models, resulting in an advanced layout process of any membrane DEA system.

DE technology is a promising field for many applications due to numerous advantages such as small weight and energy consumption and the versatility to adapt to many requirements. The work performed in this thesis expands the availability of design tools in order to push towards the utilization of DE systems.

## List of Figures

Figure 2.1	Basic structure of a DE as a sandwich consisting of polymer and electrodes. . .	7
Figure 2.2	Electrical actuation of a DE actuator increases the surface area . . . . .	9
Figure 2.3	CIP DEA and SIP DEA, at 0V and at high voltage . . . . .	10
Figure 2.4	A COP DEA, without biasing (a) and biased out-of-plane with a linear spring (b). . . . .	11
Figure 2.6	Experimental setup to characterize DEA, schematics (a) and real setup (b) [23]. . . . .	13
Figure 2.7	Characteristic force-displacement curves of a DEA, without voltage (blue) and with applied high voltage (red). . . . .	14
Figure 2.8	An external force leads to an increase in area and a decrease in thickness, both increasing the capacitance. . . . .	15
Figure 2.9	Application field for DES. . . . .	16
Figure 3.1	Example for linear biasing mechanisms and their force equilibrium with a DEA. . . . .	19
Figure 3.2	Parameter variations for LBS, change of spring pre-compression (a) and stiffness (b). . . . .	20
Figure 3.3	Optimal design for a LBS working against an 8 layered DEA, yielding a stroke of 1.2 mm. . . . .	21
Figure 3.4	System design for a fictive biasing element with negative linear stiffness. . .	22
Figure 3.5	Actuator schematics with force equilibrium working against an external load.	24
Figure 3.6	The actuator diagram of the optimal LBS design also yields 1.2 mm stroke. .	25
Figure 3.7	Actuator schematics with external load for NLS biasing (a) and correspond- ing force vs. displacement (b). . . . .	26
Figure 3.8	Force equilibrium for DEA, LBS and NLS in the DEA coordinate system (a) and corresponding energies (b). . . . .	28
Figure 3.9	The energies of DEA and LBS (a), their combination generates two stable energy minima (black circles) for 0V and HV (b). . . . .	29
Figure 3.10	The energies of DEA and NLS generates unstable energy maxima and stable energy minima. . . . .	30
Figure 3.11	A NBS as nonlinear biasing element, inner force equilibrium (a) and actua- tor force representation (b). . . . .	31

---

Figure 3.12	A sketch of a PM biased DEA system with free-body diagram, and different commercially available permanent magnet characteristics. . . . .	32
Figure 3.13	Different stability areas for arbitrary magnet curve. . . . .	33
Figure 3.14	Varying the initial magnet displacement changes the actuator performance. . . . .	34
Figure 3.15	Optimal design for PM biased system, inner forces (a) and actuator force (b). . . . .	36
Figure 3.16	A combined biasing mechanism consisting of LBS and PM for performance improvement. . . . .	37
Figure 3.17	Variation of design parameters for PM+LBS biased system. . . . .	38
Figure 3.18	All 4 design steps to maximize the actuator stroke for the given load case of 1.5 N constant force (a)-(c), and final design (d). . . . .	40
Figure 3.19	Design for unstable system in order to increase the actuator stroke, inner forces (a) and actuator force (b). . . . .	42
Figure 3.20	Assembled demonstrators, CAD model and 3D printed prototypes. . . . .	43
Figure 3.21	Stroke over voltage measurements for all designed actuator systems: LBS (a), stable PM (b), LBS+PM (c) and unstable PM (d). . . . .	44
Figure 4.1	Concept of a fluidic pressure sensor. . . . .	48
Figure 4.2	Commercially available pressure sensor SMP137 with a pressure range of 20 bar [93] (left), and a corrugated metal membrane (right). . . . .	48
Figure 4.3	Concept of DES with metal membrane as transmission barrier. . . . .	49
Figure 4.4	Measurement paradigm for intrusive pressure sensor. . . . .	50
Figure 4.5	Different metal membranes in comparison to the Bosch SMP137 pressure sensor. . . . .	51
Figure 4.6	Test setup for measuring the metal membrane's force-displacement characteristics. . . . .	52
Figure 4.7	Force-displacement measurements of all metal membranes show the difference in stiffness. . . . .	52
Figure 4.8	Schematics of a test setup for characterizing the metal membranes under pressure application. . . . .	53
Figure 4.9	Displacement-pressure characterization of metal membrane 10407. . . . .	53
Figure 4.10	Two designed DES with different geometries, the CAD drawing and the manufactured sensors. . . . .	54
Figure 4.11	The capacitance change over displacement for both DES shows different sensitivities. . . . .	55
Figure 4.12	Measurement paradigm with characterized metal membrane and DES leads to a prediction of the sensor characteristics. . . . .	56
Figure 4.13	CAD drawings and prototype of a sensor housing (a) and a test setup for comparison between DES prototype and Bosch SMP137. . . . .	57
Figure 4.14	Characterization of DES sensor, system pressure (a), membrane displacement (b) and capacitance change (c) over time. . . . .	58

Figure 4.15	Characteristic curves of DES sensor. . . . .	59
Figure 4.16	A comparison between DES and Bosch SMP137 shows a remarkable correlation. . . . .	60
Figure 4.17	An injector system for contrast fluids (a) applies pressure inside a fabric-reinforced polymer tube (b). . . . .	61
Figure 4.18	A comparison of two concepts, DE stack sensors (left) versus a DE membrane sensor (right). . . . .	62
Figure 4.19	Test setup to characterize the tube expansion, schematics (a) and CAD drawing (b). . . . .	64
Figure 4.20	To ensure a proper fixation of the tube during pressure application, the tube is fixed in a convex pod. . . . .	64
Figure 4.21	Tube displacement measurements for different pressure levels. . . . .	65
Figure 4.22	Experimental results of three tube expansion measurements, system pressure over time (a) and expansion over time (b). . . . .	66
Figure 4.23	DES approximated as a rectangle which increases its length while applying pressure. . . . .	67
Figure 4.24	When the DES is wrapped around the tube, an overlap would short-circuit the sensor. . . . .	68
Figure 4.25	DES with different geometries (a), cut from the metal frame and mounted onto the polymer tube (b). . . . .	70
Figure 4.26	Results of the system characterization for the $1 \times 1 \text{ cm}^2$ DES, pressure (a), expansion (b) and capacitance change (c) over time. . . . .	71
Figure 4.27	Characteristic curves for the $1 \times 1 \text{ cm}^2$ DES tube system. . . . .	72
Figure 4.28	A comparison of the characteristic curve of all 4 sensors yields different sensitivities dependent on the geometry. . . . .	73
Figure 4.29	A reusable clamp including a $3 \times 1 \text{ cm}^2$ DES. . . . .	74
Figure 4.30	Characteristic curves for the $3 \times 1 \text{ cm}^2$ DES system including a clamp. . . . .	75
Figure 4.31	Zoom on air bubbles flowing from left to right inside the fabric-reinforced tube. . . . .	75
Figure 4.32	The bubbles wandering through the DES are detectable by drops in the capacitance for all three measurements. . . . .	76
Figure 5.1	Configurations of a continuous body with a representation of the displacement of one point. . . . .	83
Figure 5.2	Mechanical boundary value problem in the reference configuration. . . . .	86
Figure 5.3	Electrostatic boundary value problem in the reference configuration. . . . .	87
Figure 5.4	Exemplary convergence study for a two-dimensional FE DEA model. . . . .	90
Figure 6.1	In order to mesh the silicone film, 156.25 million elements are required. . . . .	94

Figure 6.2	The standardized pure shear sample without pre-stretch and with the maximal applied stretch of 50 % . . . . .	94
Figure 6.3	A one-dimensional viscoelastic lumped model and its governing equations. .	96
Figure 6.4	Experimental data of the SIP DEA, including silicone and electrodes, with and without applied voltage. . . . .	100
Figure 6.5	Approximation of the Yeoh material parameters based on an analytic plane strain model. . . . .	102
Figure 6.6	A slow experiment characterizes the hyperelastic parameters, while a fast experiment characterizes the viscoelastic parameters. . . . .	102
Figure 6.7	A comparison between experiment and simulation for the silicone film, without viscoelastic effects (a) and with viscoelastic effects (b). . . . .	103
Figure 6.8	Input signals for all validation experiments. . . . .	104
Figure 6.9	Results of all model validations. . . . .	105
Figure 6.10	The narrowing of the strip is negligible after approximately 30 $\mu\text{m}$ . . . . .	106
Figure 6.11	Comparison of a simulation with twice as thick electrodes, geometry sketch (a) and force-displacement curves (b). . . . .	107
Figure 6.12	A patterned electrode (a) leads to a decrease in electromechanical coupling (b). . . . .	108
Figure 6.13	Different mechanic and electric field distributions at the electrode edge. . . .	109
Figure 7.1	A discretization with two-dimensional hexahedron membrane elements permits a highly efficient DEA mode. . . . .	115
Figure 7.2	A comparison of a non-deflected membrane, pure-shear deformed membrane and a membrane with necking. . . . .	118
Figure 7.3	Model validation for same experiments as shown in Figure 6.9, with input signals as shown in Figure 6.8. . . . .	119
Figure 7.4	A thickness scan along a fixed line in the middle of the unstretched probe. .	120
Figure 7.5	The actuated patterned membrane shows necking and a thickness distribution.	121
Figure 7.6	Local field distributions of the $xx$ -component of the second Piola-Kirchhoff stress, the Maxwell stress and the electric field. . . . .	122

## List of Tables

Table 1	Performance of best acrylics and silicones DEs [28]. . . . .	8
Table 2	Results of the design section for all biasing systems. . . . .	42
Table 3	Theoretical predictions and experimental measurements for all examined actuator systems. . . . .	45
Table 4	Comparison of metal membranes: geometry, thickness and measured force at 0.7 mm displacement. . . . .	51
Table 5	Comparison of DES: dimensions and capacitance. . . . .	55
Table 6	Comparison for all DES sizes: modeled and measured capacitances and capacitance changes during pressure application. . . . .	70
Table 7	Material parameters for silicone film and electrode, analytical estimation and numerically optimized. . . . .	104
Table 8	Material parameters for the membrane simulation model. . . . .	118



## Bibliography

- [1] H. P. Monner, “Smart materials for active noise and vibration reduction,” *Noise and Vibration: Emerging Methods*, no. April, pp. 18–21, 2005.
- [2] L. Riccardi, G. Rizzello, D. Naso, B. Holz, S. Seelecke, H. Janocha, and B. Turchiano, “Modeling and control of innovative smart materials and actuators: A tutorial,” *2014 IEEE Conference on Control Applications, CCA 2014*, pp. 965–977, 2014.
- [3] A. O’Halloran, F. O’Malley, and P. McHugh, “A review on dielectric elastomer actuators, technology, applications, and challenges,” *Journal of Applied Physics*, vol. 104, no. May 2014, 2008.
- [4] A. York, J. Dunn, and S. Seelecke, “Systematic approach to development of pressure sensors using dielectric electro-active polymer membranes,” *Smart Materials and Structures*, vol. 22, p. 094015, 2013.
- [5] R. E. Pelrine, R. D. Kornbluh, P. Qibing, and J. S. Eckerle, “Electroactive polymer sensors,” 2004.
- [6] P. Zanini, J. Rossiter, and M. Homer, “Self-stabilizing dielectric elastomer generators,” *Smart Materials and Structures*, vol. 26, no. 3, 2017.
- [7] —, “Modelling the effect of actuator-like behavior in dielectric elastomer generators,” *Applied Physics Letters*, vol. 107, no. 15, 2015.
- [8] C. W. Röntgen, “Ueber Die Durch Electricität Bewirkten Form- Und Volumenänderungen von Dielectrischen Körpern,” *Annalen der Physik und Chemie*, 1880.
- [9] R. Pelrine, J. S. Eckerle, and S. Chiba, “Review of Artificial Muscle Approaches,” in *Proceedings of the 3rd International Symposium on Micro Machine and Human Science*, 1992, pp. 1–19.
- [10] R. Pelrine, R. Kornbluh, Q. Pei, and J. Joseph, “High-speed electrically actuated elastomers with strain greater than 100%,” *Science*, vol. 287, no. 5454, pp. 836–9, 2000.
- [11] D. Bruch, P. Loew, S. Hau, G. Rizzello, and S. Seelecke, “Fast model-based design of large stroke dielectric elastomer membrane actuators biased with pre-stressed buckled

- beams,” *Electroactive Polymer Actuators and Devices (EAPAD) XX*, p. 15, 2018.
- [12] S. Hau, G. Rizzello, and S. Seelecke, “A novel dielectric elastomer membrane actuator concept for high-force applications,” *Extreme Mechanics Letters*, vol. 23, no. July, pp. 24–28, 2018.
- [13] S. Rosset and H. R. Shea, “Flexible and stretchable electrodes for dielectric elastomer actuators,” *Applied Physics A: Materials Science and Processing*, vol. 110, no. 2, pp. 281–307, 2013.
- [14] P. Loew, G. Rizzello, and S. S. Seelecke, “Permanent magnets as biasing mechanism for improving the performance of circular dielectric elastomer out-of-plane actuators,” in *Proc. SPIE 10163, Electroactive Polymer Actuators and Devices (EAPAD)*, vol. 1, 2017, p. 101630Y.
- [15] P. Loew, G. Rizzello, and S. Seelecke, “A Novel Biasing Mechanism for Circular out-of-plane Dielectric Actuators Based on Permanent Magnets,” *Journal on Mechatronics*, 2018.
- [16] —, “Pressure monitoring inside a polymer tube based on a dielectric elastomer membrane sensor,” *Electroactive Polymer Actuators and Devices (EAPAD) XX*, vol. 1, no. March, p. 53, 2018.
- [17] P. Loew, M. Brill, G. Rizzello, and S. Seelecke, “Development of a nonintrusive pressure sensor for polymer tubes based on dielectric elastomer membranes,” *Sensors & Actuators: A. Physical*, 2019.
- [18] J. Hofmann, S. Porscha, B. Schuch, P. Loew, and S. Seelecke, “Elektro-Aktive Polymer Derucksensor (EAP-Sensor) in Automotive Produkten,” GER Patent 102 018 217 654.4, 2018.
- [19] P. Loew and S. Seelecke, “Finite-Element Simulation of mechanically coupled elastomer and electrode layered DEAP membrane actuators,” in *SMASIS, Technical Presentation*, 2015.
- [20] P. Loew, G. Rizzello, F. Simone, and S. Seelecke, “Finite element simulation of plane strain dielectric elastomer membranes actuated by discretized electrodes,” in *SPIE Smart Structures and Materials + Nondestructive Evaluation and Health Monitoring*, 2019.
- [21] G. Rizzello, P. Loew, D. Naso, and S. Seelecke, “Analytical Modeling of Clamped Dielectric Elastomer Strip Membranes Exhibiting Necking Effect,” in *Mathematical Modelling*, vol. 51, no. 2, 2018.

- 
- [22] A. York and S. Seelecke, "Towards Self-Sensing of DEAP Actuators: Capacitive Sensing Experimental Analysis," in *ASME 2010 Conference on Smart Materials, Adaptive Structures and Intelligent Systems*. American Society of Mechanical Engineers, 2010, pp. 307–314.
- [23] S. Hau, "High-Performance dielectric elastomer actuators," Ph.D. dissertation, Saarland University, 2018.
- [24] M. Hodgins, "Design of diaphragm dielectric elastomer actuators (DEAs) and experimental characterization techniques," Ph.D. dissertation, Saarland University, 2016.
- [25] S. Rosset and H. R. Shea, "Small, fast, and tough: Shrinking down integrated elastomer transducers," *Applied Physics Reviews*, vol. 3, no. 3, 2016.
- [26] N. Ni and L. Zhang, *Dielectric Elastomer Sensors*. IntechOpen, 2017.
- [27] A. Koh, C. Keplinger, T. Li, S. Bauer, S. Member, and Z. Suo, "Dielectric Elastomer Generators: How Much Energy Can Be Converted ?" *IEEE/ASME Transactions on Mechatronics*, vol. 16, no. 1, pp. 33–41, 2011.
- [28] F. Carpi, D. De Rossi, R. Kornbluh, R. E. Pelrine, and P. Sommer-Larsen, *Dielectric elastomers as electromechanical transducers: Fundamentals, materials, devices, models and applications of an emerging electroactive polymer technology*. Elsevier, 2008.
- [29] B. Fasolt, M. Hodgins, and S. Seelecke, "Characterization of screen-printed electrodes for dielectric elastomer (DE) membranes: influence of screen dimensions and electrode thickness on actuator performance," *Sensors Actuators A: Physical*, vol. 9798, no. under review, p. 97983E, 2016.
- [30] P. Lotz, M. Matysek, and H. F. Schlaak, "Fabrication and Application of Miniaturized Dielectric Elastomer Stack Actuators," *IEEE/ASME Transactions on Mechatronics*, vol. 16, no. 1, pp. 58–66, feb 2011.
- [31] J. Maas, D. Tepel, and T. Hoffstadt, "Actuator design and automated manufacturing process for DEAP-based multilayer stack-actuators," *Meccanica*, vol. 50, no. 11, pp. 2839–2854, 2015.
- [32] G. Kovacs, L. Düring, S. Michel, and G. Terrasi, "Stacked dielectric elastomer actuator for tensile force transmission," *Sensors and Actuators A: Physical*, vol. 155, no. 2, pp. 299–307, oct 2009.
- [33] F. Carpi, I. Anderson, S. Bauer, G. Frediani, G. Gallone, M. Gei, C. Graaf, C. Jean-Mistral, W. Kaal, G. Kofod, M. Kolloche, R. Kornbluh, B. Lassen, M. Matysek, S. Michel,

- S. Nowak, B. O'Brien, Q. Pei, R. Pelrine, B. Rechenbach, S. Rosset, and H. Shea, "Standards for dielectric elastomer transducers," *Smart Materials and Structures*, vol. 24, no. 10, 2015.
- [34] G. Kovacs, P. Lochmatter, and M. Wissler, "An arm wrestling robot driven by dielectric elastomer actuators," *Smart Materials and Structures*, vol. 16, no. 2, pp. S306–S317, apr 2007.
- [35] F. Carpi, D. De Rossi, R. Kornbluh, R. Pelrine, and P. Sommer-Larsen, "Dielectric elastomers as electromechanical transducers: Fundamentals, Materials, Devices, Models and Applications of an Emerging Electroactive Polymer Technology," *Dielectric Elastomers as Electromechanical Transducers*, p. 329, 2008.
- [36] D. J. Griffiths, *Introduction to Electrodynamics*. Cambridge University Press, 2008.
- [37] R. E. Pelrine, R. D. Kornbluh, and J. P. Joseph, "Electrostriction of polymer dielectrics with compliant electrodes as a means of actuation," *Sensors and Actuators A: Physical*, vol. 64, no. 1, pp. 77–85, 1998.
- [38] F. B. Madsen, A. E. Daugaard, S. Hvilsted, and A. L. Skov, "The Current State of Silicone-Based Dielectric Elastomer Transducers," *Macromolecular Rapid Communications*, vol. 37, pp. 378–413, 2016.
- [39] R. Heydt, R. Kornbluh, J. Eckerle, and R. Pelrine, "Sound radiation properties of dielectric elastomer electroactive polymer loudspeakers," in *Smart Structures and Materials 2006: Electroactive Polymer Actuators and Devices (EAPAD)*, Y. Bar-Cohen, Ed., vol. 6168, mar 2006, pp. 61 681M–61 681M–8.
- [40] F. Carpi, C. Menon, and D. De Rossi, "Electroactive Elastomeric Actuator for All-Polymer Linear Peristaltic Pumps," *IEEE/ASME Transactions on Mechatronics*, vol. 15, no. 3, pp. 460–470, jun 2010.
- [41] R. E. Pelrine, R. D. Kornbluh, R. Heydt, and J. R. Heim, "Electroactive polymer devices for moving fluid," 2008.
- [42] T. Kobayashi and S. K. Smoukov, "Pulsed actuation avoids failure in dielectric elastomer artificial muscles," *International Journal of Smart and Nano Materials*, vol. 5, no. 4, pp. 217–226, 2015.
- [43] M. Hill, G. Rizzello, and S. Seelecke, "Development and Experimental Characterization of a Pneumatic Valve Actuated by a Dielectric Elastomer Membrane," *Smart Materials and Structures*, 2017.

- [44] S. Hau, A. York, and S. Seelecke, "A Compact High-Force Dielectric Elastomer Membrane Actuator," *Actuator 2016, 15th International Conference on New Actuators & 9th International Exhibition on Smart Actuators and Drive Systems*, pp. 282–285, 2016.
- [45] F. Carpi, G. Frediani, and D. De Rossi, "Electroactive elastomeric haptic displays of organ motility and tissue compliance for medical training and surgical force feedback," *IEEE Transaction Biomed. Eng.*, vol. 56, 2009.
- [46] J. D. N. H. R. Choi, S. M. Ryew, K. M. Jung, H. M. Kim, J. W. Jeon, "Soft Actuator for Robotic Applications Based on Dielectric Elastomer: Quasi-static Analysis," *International Conference on Robotics & Automation*, no. May, pp. 2–7, 2002.
- [47] S. Hau, G. Rizzello, M. Hodgins, A. York, and S. Seelecke, "Design and Control of a High-Speed Positioning System Based on Dielectric Elastomer Membrane Actuators," *IEEE/ASME Transactions on Mechatronics*, 2017.
- [48] D. Mccoul, S. Rosset, N. Besse, and H. Shea, "Multifunctional shape memory electrodes for dielectric elastomer actuators enabling high holding force and low-voltage multi-segment addressing," *Smart Materials and Structures*, vol. 025015, 2017.
- [49] O. A. Araromi, I. Gavrilovich, J. Shintake, S. Rosset, M. Richard, V. Gass, and H. R. Shea, "Rollable Multisegment Dielectric Elastomer Minimum Energy Structures for a Deployable Microsatellite Gripper," *IEEE/ASME Transactions on Mechatronics*, vol. 20, no. 1, pp. 438–446, feb 2015.
- [50] G. Kofod, P. Sommer-Larsen, R. Kornbluh, and R. Pelrine, "Actuation response of polyacrylate dielectric elastomers," *Journal of Intelligent Materials Systems and Structures*, vol. 14, no. 12, pp. 787–793, 2003.
- [51] G. Kofod, "The static actuation of dielectric elastomer actuators: How does pre-stretch improve actuation?" *Journal of Physics D: Applied Physics*, vol. 41, no. 21, 2008.
- [52] M. Hodgins, A. York, and S. Seelecke, "Experimental comparison of bias elements for out-of-plane DEAP actuator system," *Smart Materials and Structures*, vol. 22, no. 9, p. 094016, 2013.
- [53] S. Hau, D. Bruch, G. Rizzello, P. Motzki, and S. Seelecke, "Silicone based dielectric elastomer strip actuators coupled with nonlinear biasing elements for large actuation strains," *Smart Materials and Structures*, vol. 27, no. 7, 2018.
- [54] M. Hill, S. Seelecke, D. C. Rodegheri, M. Konstandin, and P. Krippner, "Folienwandler," 2017.

- [55] M. Hill, G. Rizzello, and S. Seelecke, "Development and experimental characterization of a dielectric elastomer membrane strip actuator," *Smart Materials and Structures*, vol. 27, no. 2, 2018.
- [56] A. Poulin, S. Rosset, and H. Shea, "Fully printed 3 microns thick dielectric elastomer actuator," in *Proc. SPIE 9798, Electroactive Polymer Actuators and Devices (EAPAD)*, 2016, p. 97980L.
- [57] S. Schlatter, S. Rosset, and H. Shea, "Inkjet printing of carbon black electrodes for dielectric elastomer actuators," *Proc. SPIE 10163, Electroactive Polymer Actuators and Devices (EAPAD)*, vol. 1016311, p. 1016311, 2017.
- [58] O. A. Araromi, S. Rosset, and H. R. Shea, "High-Resolution, Large-Area Fabrication of Compliant Electrodes via Laser Ablation for Robust, Stretchable Dielectric Elastomer Actuators and Sensors," *ACS Applied Materials and Interfaces*, vol. 7, no. 32, pp. 18 046–18 053, 2015.
- [59] B. Fasolt, M. Hodgins, G. Rizzello, and S. Seelecke, "Effect of screen printing parameters on sensor and actuator performance of dielectric elastomer (DE) membranes," *Sensors and Actuators, A: Physical*, vol. 265, no. October, pp. 10–19, 2017.
- [60] S. Zakaria, P. H. F. Morshuis, M. Y. Benslimane, L. Yu, and A. L. Skov, "The electrical breakdown strength of pre-stretched elastomers, with and without sample volume conservation," *Smart Materials and Structures*, vol. 24, no. 5, p. 055009, 2015.
- [61] S. Hau, A. York, and S. Seelecke, "Performance prediction of circular dielectric electroactive polymers membrane actuators with various geometries," in *SPIE Smart Structures and Materials+ Nondestructive Evaluation and Health Monitoring*, Y. Bar-Cohen, Ed., apr 2015, p. 94300C.
- [62] B. Fasolt, M. Hodgins, and S. Seelecke, "Characterization of screen-printed electrodes for dielectric elastomer (DE) silicone membranes: Influence of screen dimensions and electrode thickness on actuator and sensor performance," *Sensors & Actuators: A. Physical*, 2017.
- [63] A. Tröls, A. Kogler, R. Baumgartner, R. Kaltseis, C. Keplinger, R. Schwödiauner, I. Graz, and S. Bauer, "Stretch dependence of the electrical breakdown strength and dielectric constant of dielectric elastomers," *Smart Materials and Structures*, vol. 22, no. September, 2013.
- [64] M. Rosenthal, N. Bonwit, C. Duncheon, and J. Heim, "Applications of dielectric elastomer EPAM sensors," in *The 14th International Symposium on: Smart Structures and*

- Materials \& Nondestructive Evaluation and Health Monitoring*. International Society for Optics and Photonics, 2007, p. 65241F.
- [65] D. Rychkov, F. He, J. Wang, M. Schulze, G. Gidion, W. Wirges, and R. Gerhard, “Soft Stretchable All-Silicone Sensor for Transport-Infrastructure Monitoring,” in *Sensors and Measuring Systems; 19th ITG/GMA-Symposium*, 2018.
- [66] G. Buchberger, B. Mayrhofer, B. Jakoby, W. Hilber, and S. Bauer, “Dynamic capacitive extensometry setup for in-situ monitoring of dielectric elastomer actuators,” *2012 IEEE I2MTC - International Instrumentation and Measurement Technology Conference, Proceedings*, pp. 75–80, 2012.
- [67] B.-C. Kim, S. Shin, J. Chung, Y. Lee, J.-D. Nam, H. Moon, H. R. Choi, and J. C. Koo, “A dual axis shear force film sensor for robotic tactile applications,” *Electroactive Polymer Actuators and Devices (EAPAD) 2011 A4 - The Society of Photo-Optical Instrumentation Engineers (SPIE); American Society of Mechanical Engineers*, vol. 7976, p. 797628, 2011.
- [68] L. Viry, A. Levi, M. Totaro, A. Mondini, V. Mattoli, B. Mazzolai, and L. Beccai, “Flexible three-axial force sensor for soft and highly sensitive artificial touch,” *Advanced Materials*, vol. 26, no. 17, pp. 2659–2664, 2014.
- [69] “StretchSense,” April 24, 2019. [Online]. Available: [www.stretchsense.com](http://www.stretchsense.com)
- [70] “ElastiSense: Robust Industrial Sensors with Electro-Active Polymer technology,” April 24, 2019. [Online]. Available: [www.elastisense.com](http://www.elastisense.com)
- [71] “Parker FlexSense Evaluation Kits | Parker Quick Coupling Division.” April 24, 2019. [Online]. Available: <http://solutions.parker.com/FlexSenseKit>
- [72] H. Vandeparre, D. Watson, and S. P. Lacour, “Extremely robust and conformable capacitive pressure sensors based on flexible polyurethane foams and stretchable metallization,” *Applied Physics Letters*, vol. 103, no. 20, 2013.
- [73] H. Böse, E. Fuß, and P. Lux, “Influence of design and material properties on the performance of dielectric elastomer compression sensors,” *Electroactive Polymer Actuators and Devices (EAPAD)*, vol. 9430, p. 943029, 2015.
- [74] M. Hodgins, G. Rizzello, D. Naso, A. York, and S. Seelecke, “An electro-mechanically coupled model for the dynamic behavior of a dielectric electro-active polymer actuator,” *Smart Materials and Structures*, vol. 23, no. 10, p. 104006, 2014.
- [75] M. Hodgins, G. Rizzello, A. York, D. Naso, and S. Seelecke, “A smart experimental technique for the optimization of dielectric elastomer actuator (DEA) systems,” *Smart*

- Materials and Structures*, vol. 24, no. 9, p. 094002, 2015.
- [76] G. Berselli, R. Vertechy, G. Vassura, and V. Parenti-Castelli, "Optimal Synthesis of Conically Shaped Dielectric Elastomer Linear Actuators: Design Methodology and Experimental Validation," *IEEE/ASME Transactions on Mechatronics*, vol. 16, no. 1, pp. 67–79, feb 2011.
- [77] M. Hodgins, A. York, and S. Seelecke, "Modeling and experimental validation of a bistable out-of-plane DEAP actuator system," *Smart Materials and Structures*, vol. 20, no. 9, p. 094012, aug 2011.
- [78] "EAP," April 24, 2019. [Online]. Available: <https://promo.parker.com/promotionsite/eap/us/en/products/Actuators>
- [79] M. Hodgins and S. Seelecke, "Systematic experimental study of pure shear type dielectric elastomer membranes with different electrode and film thicknesses," *Smart Materials and Structures*, vol. 25, no. 9, p. 095001, 2016.
- [80] G. Berselli, R. Vertechy, G. Vassura, and V. P. Castelli, "Design of a Single-Acting Constant-Force Actuator Based on Dielectric Elastomers Title," *J. Mechanisms Robotics 1(3)*, 2009.
- [81] X.-Q. Li, W.-B. Li, W.-M. Zhang, H.-X. Zou, Z.-K. Peng, and G. Meng, "Magnetic force induced tristability for dielectric elastomer actuators," *Smart Materials and Structures*, vol. 26, no. 10, 2017.
- [82] V. V. Smirnov, J. V. Rau, V. Rossi, D. Ferro, S. M. Barinov, and V. R. Albertini, "Performance improvement of planar dielectric elastomer actuators by magnetic modulating mechanism," *Smart Materials and Structures*, pp. 1–20, 2018.
- [83] D. Bruch, "Designmethode zur Auslegung dielektrischer Elastomeraktoren mit nichtlinearen Vorspannmechanismen," Ph.D. dissertation, Universität des Saarlandes, 2017.
- [84] G. Rizzello, D. Naso, P. Bari, A. York, and P. H. Corp, "A Self-Sensing Approach for Dielectric Elastomer Actuators Based on Online Estimation A Self-Sensing Approach for Dielectric Elastomer Actuators Based on Online Estimation Algorithms," *IEEE/ASME Transactions on Mechatronics*, vol. 22, no. 2, pp. 728–738, 2017.
- [85] D. Vokoun, M. Beleggia, L. Heller, and P. Šittner, "Magnetostatic interactions and forces between cylindrical permanent magnets," *Journal of Magnetism and Magnetic Materials*, vol. 321, no. 22, pp. 3758–3763, 2009.
- [86] "K&J Magnetics: R624," April 24, 2019. [Online]. Available: <https://www.kjmagnetics.com/proddetail.asp?prod=R624>

- [87] G. Rizzello, D. Naso, A. York, and S. Seelecke, "Closed loop control of dielectric elastomer actuators based on self-sensing displacement feedback," *Smart Materials and Structures*, 2016.
- [88] D. J. Lipomi, M. Vosgueritchian, B. C. Tee, S. L. Hellstrom, J. A. Lee, C. H. Fox, and Z. Bao, "Skin-like pressure and strain sensors based on transparent elastic films of carbon nanotubes," *Nature Nanotechnology*, vol. 6, no. 12, pp. 788–792, 2011.
- [89] S. Laflamme, H. S. Saleem, B. K. Vasan, R. L. Geiger, D. Chen, M. R. Kessler, and K. Rajan, "Soft elastomeric capacitor network for strain sensing over large surfaces," *IEEE/ASME Transactions on Mechatronics*, vol. 18, no. 6, pp. 1647–1654, 2013.
- [90] T. Q. Trung and N. E. Lee, "Flexible and Stretchable Physical Sensor Integrated Platforms for Wearable Human-Activity Monitoring and Personal Healthcare," *Advanced Materials*, vol. 28, no. 22, pp. 4338–4372, 2016.
- [91] P. Roberts, D. D. Damian, W. Shan, T. Lu, and C. Majidi, "Soft-matter capacitive sensor for measuring shear and pressure deformation," *Proceedings - IEEE International Conference on Robotics and Automation*, pp. 3529–3534, 2013.
- [92] S. C. B. Mannsfeld, B. C.-K. Tee, R. M. Stoltenberg, C. V. H.-H. Chen, S. Barman, B. V. O. Muir, A. N. Sokolov, C. Reese, and Z. Bao, "Highly sensitive flexible pressure sensors with microstructured rubber dielectric layers," *Nature Materials*, vol. 9, no. 10, pp. 859–864, 2010.
- [93] "Bosch SMP137," April 24, 2019. [Online]. Available: <https://www.elektroniknet.de/elektronik-automotive/sonstiges/drucksensor-misst-druecke-zwischen-10-und-100-bar-30909.html>
- [94] "Membranenbeck," April 24, 2019. [Online]. Available: <http://www.membranenbeck.de/>
- [95] G. Dieter, *Mechanical Metallurgy*. McGraw-Hill, 1986.
- [96] "Membranenbeck Membranen," April 24, 2019. [Online]. Available: <http://www.membranenbeck.de/membranen>
- [97] "Accutron HP: Medtron AG," April 24, 2019. [Online]. Available: <http://www.medtron.com/de/angiographie/accutron-hp/>
- [98] T. Hoffstadt and J. Maas, "Self-sensing Algorithms for Dielectric Elastomer Multilayer Stack-Transducers," *IFAC-PapersOnLine*, vol. 49, no. 21, pp. 373–379, 2016.

- [99] H. Böse and E. Fuß, “Novel dielectric elastomer sensors for compression load detection,” *Electroactive Polymer Actuators and Devices (EAPAD)*, vol. 9056, p. 905614, 2014.
- [100] V. Vullo and S. Analysis, *Circular Cylinders and Pressure Vessels*. Springer, 2014.
- [101] M. Johlitz and S. Diebels, “Characterisation of a polymer using biaxial tension tests. Part I: Hyperelasticity,” *Archive of Applied Mechanics*, vol. 81, no. 10, pp. 1333–1349, 2011.
- [102] WackerChemieAG, “Neue Perspektiven Und Innovative Anwendungen Mit Elastosil ® Film Hauchdünne Siliconfolie,” April 24, 2019. [Online]. Available: [http://www.wacker.com/cms/media/publications/downloads/7091\\_DE.pdf](http://www.wacker.com/cms/media/publications/downloads/7091_DE.pdf)
- [103] G. Holzapfel, *Nonlinear Solid Mechanics*. Wiley, 2000.
- [104] G. Rizzello, M. Hodgins, D. Naso, A. York, and S. Seelecke, “Dynamic Modeling and Experimental Validation of an Annular Dielectric Elastomer Actuator With a Biasing Mass,” *Journal of Vibration and Acoustics*, vol. 137, no. 1, p. 011014, 2015.
- [105] —, “Dynamic Electromechanical Modeling of a Spring-biased Dielectric Electroactive Polymer Actuator System,” in *SMASIS*, 2014, pp. 1–10.
- [106] G. Rizzello, “Modeling , Control and Self-Sensing of Dielectric Elastomer Actuators,” Ph.D. dissertation, Politecnico di Bari, 2016.
- [107] W. Kaal and S. Herold, “Electroactive polymer actuators in dynamic applications,” *IEEE/ASME Transactions on Mechatronics*, vol. 16, no. 1, pp. 24–32, 2011.
- [108] T. Hoffstadt and J. Maas, “Analytical modeling and optimization of DEAP-based multi-layer stack-transducers,” *Smart Materials and Structures*, vol. 24, no. 9, p. 94001, 2015.
- [109] G. Berselli, R. Vertechy, M. Babič, and V. Parenti Castelli, “Dynamic modeling and experimental evaluation of a constant-force dielectric elastomer actuator,” *Journal of Intelligent Material Systems and Structures*, vol. 24, no. 6, pp. 779–791, 2013.
- [110] W. Kaal, “Dielektrische Elastomer-Stapelaktoren mit gelochten Elektroden für strukturdynamische Anwendungen,” Ph.D. dissertation, TU Darmstadt, 2014.
- [111] H. S. Park, Z. Suo, J. Zhou, and P. A. Klein, “A dynamic finite element method for inhomogeneous deformation and electromechanical instability of dielectric elastomer transducers,” *International Journal of Solids and Structures*, vol. 49, no. 15-16, pp. 2187–2194, 2012.

- 
- [112] M. Wissler and E. Mazza, "Modeling and simulation of dielectric elastomer actuators," in *Smart Materials and Structures* 142, 2005, pp. 1396–1402.
- [113] R. Vertechy, A. Frisoli, M. Bergamasco, F. Carpi, G. Frediani, and D. D. Rossi, "Modeling and experimental validation of buckling dielectric elastomer actuators," *Smart Materials and Structures*, vol. 21, 2012.
- [114] M. Jabareen, "On the Modeling of Electromechanical Coupling in Electroactive Polymers Using the Mixed Finite Element Formulation," *Procedia IUTAM*, vol. 12, pp. 105–115, 2015.
- [115] S. N. Atluri, "Alternate stress and conjugate strain measures, and mixed variational formulations involving rigid rotations, for computational analyses of finitely deformed solids, with application to plates and shells-I. Theory," *Computers and Structures*, vol. 18, no. 1, pp. 93–116, 1984.
- [116] D. K. Cheng, *Field and Wave Electromagnetics*, 2nd ed. Eddison-Wesley Publishing Company, 1989.
- [117] X. Wang, X.-B. Wang, and P. R. Gascoyne, "General expressions for dielectrophoretic force and electrorotational torque derived using the Maxwell stress tensor method," *Journal of Electrostatics*, vol. 39, no. 4, pp. 277–295, 1997.
- [118] S. Zwecker, S. Klinkel, and R. Müller, "Nonlinear finite element simulation of thin dielectric elastomer structures," *Proceedings of 1st Young Researcher Symposium by Center for Mathematical and Computational Modelling*, 2011.
- [119] P. A. Martins, R. M. Jorge, and A. J. Ferreira, "A comparative study of several material models for prediction of hyperelastic properties: Application to silicone-rubber and soft tissues," *Strain*, vol. 42, no. 3, pp. 135–147, 2006.
- [120] *Application of Comsol Multiphysics 3.2 to finite strain viscoelasticity of an elastomeric solid.*, 2006.
- [121] Z. Suo, "Theory of Dielectric Elastomers," *Acta Mechanica Solida Sinica*, vol. 23, no. 6, 2010.
- [122] M. Rackl, "Material testing and hyperelastic material model curve fitting for Ogden , Polynomial and Yeoh models," in *ScilabTEC 2015, Paris*, no. May, 2015.
- [123] K. Levenberg, "A method for the solution of certain non-linear problems in least squares," *Quart. Appl. Math.* 2, 1944.

- [124] H. Sönerlind, “Singularities in Finite Element Models: Dealing with Red Spots,” April 24, 2019. [Online]. Available: <https://www.comsol.de/blogs/singularities-in-finite-element-models-dealing-with-red-spots/>
- [125] J.-M. Bueno-Barrachina, C.-S. Cañas-Peñuelas, and S. Catalan-Izquierdo, “FEM Edge Effect and Capacitance Evaluation on Cylindrical Capacitors,” *Journal of Energy and Power Engineering*, vol. 6, pp. 2063–2069, 2012.
- [126] E. Rustighi, W. Kaal, S. Herold, and A. Kubbara, “Experimental Characterisation of a Flat Dielectric Elastomer Loudspeaker,” *Actuators*, pp. 1–14, 2018.
- [127] S. Nalbach, G. Rizzello, and S. Seelecke, “Continuum Vibration Analysis of Dielectric Elastomer Membranes,” *SPIE Smart Structures and Materials + Nondestructive Evaluation and Health Monitoring*, vol. 10163, pp. 2–9, 2017.
- [128] J. Zhu, S. Cai, and Z. Suo, “Resonant behavior of a membrane of a dielectric elastomer,” *International Journal of Solids and Structures*, vol. 47, no. 24, pp. 3254–3262, 2010.
- [129] Comsol Multiphysics, “Structural Mechanics Module User’s Guide,” 2018.
- [130] J. Bonet, R. D. Wood, J. Mahaney, and P. Heywood, “Finite element analysis of air supported membrane structures,” *Comput. Methods Appl. Mech. Engrg.*, vol. 190, 2000.
- [131] M. Hodgins, A. York, and S. Seelecke, “Systematic experimental investigation of dielectric electroactive polymers using a custom-built uniaxial tensile test RIG,” *Journal of Intelligent Material Systems and Structures*, vol. 1, pp. 1–12, 2017.

## **Eidesstattliche Versicherung**

Hiermit versichere ich an Eides statt, dass ich die vorliegende Arbeit selbstständig und ohne Benutzung anderer als der angegebenen Hilfsmittel angefertigt habe. Die aus anderen Quellen oder indirekt übernommenen Daten und Konzepte sind unter Angabe der Quelle gekennzeichnet. Die Arbeit wurde bisher weder im In- noch im Ausland in gleicher oder ähnlicher Form in einem Verfahren zur Erlangung eines akademischen Grades vorgelegt.

Saarbrücken, den

Philipp Loew